

# Aquifer characterisation using nuclear magnetic resonance

vorgelegt von  
Diplom Geophysiker  
**Raphael Dlugosch**  
geb. in Rosenheim

von der Fakultät VI – Planen Bauen Umwelt  
der Technischen Universität Berlin  
zur Erlangung des akademischen Grades

Doktor der Naturwissenschaften  
- Dr. rer. nat. -

genehmigte Dissertation

Promotionsausschuss:

Vorsitzender: Prof. Dr. G. Franz  
Gutachter: Prof. Dr. U. Yaramanci  
Gutachter: Prof. Dr. E. Auken  
Gutachter: Dr. M. Müller-Petke

Tag der wissenschaftlichen Aussprache: 05. Dezember 2014

Berlin 2014  
D83



# Abstract

Not only is water the source of life, but access to clean drinking water is acknowledged to be a human right. Nuclear magnetic resonance (NMR) can help to gather detailed information about the extent and hydraulic properties of an aquifer which are essential information for a sustainable use. The main objectives of this thesis are (i) to revise the prediction of hydraulic conductivities including coarse-grained unconsolidated sediments using NMR and (ii) to develop a robust inversion approach for surface NMR to estimate the 2D distribution of water content and NMR relaxation time in the subsurface.

The Kozeny-Godefroy model is introduced which allows for an advanced prediction of hydraulic conductivity from NMR measurements. The model replaces the empirical factors in known relations with physical, structural and NMR intrinsic parameters. It additionally accounts for the relaxation of protons in the bulk water and in pores which are controlled by diffusion limited conditions.

A new sophisticated inversion approach for 2D surface NMR surveys is presented. It considers the entire recorded data set at once allowing to determine the 2D distribution of water content and NMR relaxation time in the subsurface. The outstanding features of this new inversion approach are its 2D capability, robustness in spite of noisy data and the potential to distinguish aquifers of different lithology due to their NMR relaxation times.

Finally, the results of an extensive hydrogeophysical study at the Schillerslage test site, including surface, Earth's field, borehole and laboratory NMR measurements, are presented, compared and discussed. The obtained NMR parameters are used for the prediction of 1D and 2D distributions of the hydraulic conductivity in the subsurface.

In conclusion, this thesis demonstrates that the estimation of hydraulic conductivities in aquifers using NMR can be improved using the Kozeny-Godefroy model. The presented new inversion approach increases the range of application for surface NMR to 2D targets. This allows obtaining 2D images of the hydraulic conductivity distribution in the subsurface.



# Zusammenfassung

Wasser ist nicht nur die Quelle des Lebens, der Zugang zu Trinkwasser ist auch ein anerkanntes Menschenrecht. Die Methode der Kernspinresonanz (NMR) erlaubt es detaillierte Informationen über Ausdehnung und hydraulischen Eigenschaften von Aquiferen zu sammeln. Dies stellt eine wesentliche Voraussetzung für deren nachhaltige Nutzung dar. Die wichtigsten Ziele dieser Arbeit sind (i) die verbesserte Ableitung der hydraulischen Leitfähigkeit aus NMR-Messungen, insbesondere an groben Lockermaterial, und (ii) die Entwicklung eines Inversionsansatzes für Oberflächen-NMR-Messungen zur Ableitung der 2D-Verteilung von Wassergehalt und NMR-Relaxationszeit im Untergrund.

Das Kozeny-Godefroy-Modell erlaubt eine verbesserte Ableitung der hydraulischen Leitfähigkeit aus NMR-Messungen. Es ersetzt die empirischen Faktoren in bekannten Gleichungen mit physikalischen, strukturellen und NMR-spezifischen Parametern und berücksichtigt den Relaxationsprozess von Protonen in freiem Wasser und in diffusionskontrollierten Porenräumen.

Der neue Inversionsansatz zur Auswertung von 2D Oberflächen-NMR-Messungen berücksichtigt den kompletten Datensatz in einem Arbeitsschritt und bestimmt daraus die 2D-Verteilung von Wassergehalt und NMR-Relaxationszeit im Untergrund. Herausragenden Eigenschaften des Inversionsansatzes sind dessen 2D-Fähigkeit und erhöhte Widerstandsfähigkeit gegenüber verrauschten Daten. Zudem ermöglicht die NMR-Relaxationszeit die Unterscheidung verschiedener Lithologien.

Die Ergebnisse einer umfangreichen hydrogeophysikalischen Untersuchung am Teststandort Schillerslage, bestehend aus Oberflächen-, Erdfeld-, Bohrloch- und Labor-NMR-Messungen, werden vorgestellt, verglichen und diskutiert. Aus den gewonnenen NMR-Parametern werden die 1D- und 2D-Verteilungen der hydraulischen Leitfähigkeit im Untergrund abgeleitet.

Als Fazit der Arbeit kann gesagt werden, dass das Kozeny-Godefroy-Modell die Ableitung der hydraulischen Leitfähigkeiten in Aquiferen aus NMR-Messungen verbessert und der neue Inversionsansatz den Anwendungsbereich von Oberflächen-NMR auf 2D-Ziele vergrößert. In Kombination erlauben beide Neuerungen die Abbildung der 2D-Verteilung der hydraulischen Leitfähigkeit im Untergrund.



# Contents

<b>1. Introduction</b>	<b>1</b>
<b>2. Fundamentals of nuclear magnetic resonance (NMR)</b>	<b>5</b>
2.1. Principles . . . . .	5
2.2. Applications . . . . .	7
2.3. Initial amplitude and water content ( $w$ ) . . . . .	8
2.4. NMR relaxation times ( $T$ ) . . . . .	8
<b>3. The link between NMR and hydraulic conductivity (<math>K</math>)</b>	<b>11</b>
3.1. Fluid flow in porous media . . . . .	11
3.2. NMR in porous media . . . . .	12
3.3. Predicting $K$ from NMR measurements . . . . .	14
3.4. The new Kozeny-Godefroy model (KGM) . . . . .	15
3.4.1. Derivation . . . . .	15
3.4.2. Sensitivity to model parameters . . . . .	16
3.5. Experimental validation of KGM . . . . .	19
3.5.1. Sample material and preparation . . . . .	19
3.5.2. $K$ measurements . . . . .	19
3.5.3. NMR measurements . . . . .	21
3.6. Benefits and limitations of KGM . . . . .	22
3.6.1. Evaluation of KGM . . . . .	22
3.6.2. Comparison to other models . . . . .	24
3.6.3. Limitation of the flow model . . . . .	27
3.6.4. Limitation of the NMR model . . . . .	29
3.7. Summary on KGM . . . . .	29
<b>4. Fundamentals of surface NMR</b>	<b>31</b>
4.1. Basics . . . . .	31
4.2. Sensitivity kernel . . . . .	32
4.2.1. General 3D kernel . . . . .	32
4.2.2. 2D and 1D kernel . . . . .	32

## Contents

4.2.3.	Impact of pulse moment, loop size and electrical resistivity . . . . .	32
4.3.	Forward calculation . . . . .	36
4.3.1.	General 3D formulation . . . . .	36
4.3.2.	Effective dead time . . . . .	36
4.3.3.	Complex-valued signal . . . . .	36
4.3.4.	Discrete data and model space . . . . .	37
4.4.	Inversion . . . . .	37
4.4.1.	General inversion approach . . . . .	37
4.4.2.	Initial value inversion (IVI) scheme . . . . .	38
4.4.3.	Time-step inversion (TSI) scheme . . . . .	40
4.4.4.	$qt$ inversion (QTI) scheme . . . . .	41
<b>5.</b>	<b>2D distribution of <math>w</math> and <math>T</math> from surface NMR</b>	<b>43</b>
5.1.	2D QTI approach . . . . .	43
5.1.1.	Objective . . . . .	43
5.1.2.	Optimising the size of the forward problem . . . . .	43
5.2.	Synthetic study . . . . .	45
5.2.1.	Forward calculation . . . . .	45
5.2.2.	Inversion . . . . .	47
5.3.	Field case 1: Eddelstorf . . . . .	48
5.3.1.	Site information . . . . .	48
5.3.2.	Surface NMR survey . . . . .	50
5.3.3.	Inverse modelling . . . . .	50
5.3.4.	2D QTI result . . . . .	50
5.3.5.	Results of other 2D inversion approaches . . . . .	51
5.3.6.	Impact of regularisation anisotropy . . . . .	51
5.3.7.	Impact of electrical resistivity . . . . .	53
5.4.	Field case 2: Nauen . . . . .	55
5.4.1.	Site information . . . . .	55
5.4.2.	Surface NMR survey . . . . .	57
5.4.3.	Results using different 2D inversion approaches . . . . .	58
5.4.4.	Comparison to the former 2D inversion result . . . . .	60
5.4.5.	Comparison to laboratory results . . . . .	62
5.5.	Discussion on 2D QTI . . . . .	63
5.5.1.	Benefit of the NMR relaxation time . . . . .	63
5.5.2.	Advantages of the 2D QTI . . . . .	64
5.5.3.	Monoexponential model space . . . . .	64
5.5.4.	Complex signal . . . . .	65

<b>6. The hydrogeophysical test site Schillerslage</b>	<b>67</b>
6.1. Objectives . . . . .	67
6.2. Overview . . . . .	67
6.2.1. Location . . . . .	67
6.2.2. Geology . . . . .	68
6.2.3. Drill location Eng20 . . . . .	71
6.2.4. Summary of applied NMR methods . . . . .	73
6.3. Structural investigation . . . . .	76
6.3.1. Electrical resistivity tomography . . . . .	76
6.3.2. 2D surface NMR . . . . .	77
6.4. Parameter investigation . . . . .	81
6.4.1. NMR water content . . . . .	82
6.4.2. Transverse NMR relaxation time ( $T_2$ ) . . . . .	83
6.4.3. Longitudinal NMR relaxation time ( $T_1$ ) . . . . .	87
6.4.4. Impact of method specific properties on the obtained NMR parameters . . . . .	89
6.5. Prediction of $K$ from NMR measurements . . . . .	97
6.5.1. 1D application using different NMR methods . . . . .	97
6.5.2. 2D application using surface NMR . . . . .	100
6.6. Summary of the Schillerslage study . . . . .	102
<b>7. Summary and Outlook</b>	<b>103</b>
<b>8. Acknowledgements</b>	<b>105</b>
<b>A. Appendix</b>	<b>115</b>
A.1. KGM for planar and spherical pore geometries . . . . .	115
A.2. Structure of the Jacobian matrix . . . . .	117
A.3. Transformation of the model domain . . . . .	118
A.4. Coordinates of the field examples . . . . .	119



# List of abbreviations and symbols

## Abbreviations

<b>NMR</b>	nuclear magnetic resonance
<b>SDR</b>	Schlumberger-Doll-Research equation
<b>FID</b>	free induction decay
<b>IVI</b>	initial value inversion
<b>TSI</b>	time-step inversion
<b>QTI</b>	<i>qt</i> inversion
<b>D</b>	-dimensional
<b>COI</b>	coincident
<b>tx</b>	transmitter
<b>rx</b>	receiver
<b>HOL</b>	half overlapping
<b>E2E</b>	edge-to-edge
<b>KGM</b>	Kozeny-Godefroy model
<b>ERT</b>	electrical resistivity tomography
<b>MRI</b>	magnetic resonance imaging
<b>CPMG</b>	Carr-Purcell-Meiboom-Gill pulse sequence
<b>SB</b>	Seevers model including bulk water relaxation
<b>SDR</b>	Schlumberger-Doll Research equation
<b>SPM</b>	single pore mode
<b>RMS</b>	root mean square
<b>RDP</b>	relaxation during pulse
<b>GPR</b>	ground-penetrating radar
<b>LIAG</b>	Leibniz Institute for Applied Geophysics
<b>SI</b>	International System of Units
<b>API</b>	American Petroleum Institute units

## Contents

### Symbols

$w$	$[\text{m}^3/\text{m}^3]$	water content
$\phi$	$[\text{m}^3/\text{m}^3]$	porosity
$T$	[s]	NMR relaxation time
$S$	$[\text{m}^2]$	pore surface
$V$	$[\text{m}^3]$	pore volume
$S/V$	[1/m]	surface-to-volume ratio
$k$	$[\text{m}^2]$	permeability
$K$	[m/s]	hydraulic conductivity
$T_B$	[s]	bulk water NMR relaxation time
$\mathbf{G}^{3d}$	$[\text{V}/\text{m}^3]$	3D sensitivity kernel
$\hat{\mathbf{S}}$	[Js/rad]	nuclear spin
$\hat{\boldsymbol{\mu}}$	[J/T]	nuclear magnetic moment
$\gamma$	[rad/(Ts)]	gyromagnetic ratio (proton: $267.5 \times 10^6 \text{ rad T}^{-1} \text{ s}^{-1}$ )
$\mathbf{B}_0$	[T]	static magnetic field
$\theta$	[K]	temperature ( $\text{K} = \text{°C} + 273.15$ )
$\mathbf{M}_0$	[A/m]	macroscopic net magnetisation in thermal equilibrium
$\hbar$	[Js]	Planck's constant divided by $2\pi$ ( $1.054 \times 10^{-34} \text{ Js}$ )
$k_B$	[J/K]	Boltzmann constant
$N_P$	$[\text{1}/\text{m}^3]$	number of nuclei per unit volume (protons in water: $\frac{2N_A \rho}{18 \text{ g mol}^{-1}} = 6.691 \times 10^{28} \text{ m}^{-3}$ )
$N_A$	[1/mol]	Avogadro constant ( $6.022 \times 10^{22} \text{ mol}^{-1}$ )
$\beta$	[rad]	flip angle
$\omega_0$	[rad/s]	Larmor frequency
$\mathbf{M}$	[A/m]	macroscopic net magnetisation
$t$	[s]	time
$T_1$	[s]	longitudinal NMR relaxation time
$T_2$	[s]	transverse NMR relaxation time
$T_2^*$	[s]	$T_2$ including dephasing
$\Delta \mathbf{B}_0$	[T/m]	field-strength gradient of $\mathbf{B}_0$
$t_{es}$	[s]	inter-echo spacing of the CPMG sequence
$D$	$[\text{m}^2/\text{s}]$	self-diffusion constant
$T_D$	[s]	$T$ observed by a CPMG pulse sequence due to diffusion
$T_{2o}$	[s]	$T_2$ due to all other processes
$r_{\text{tube}}$	[m]	pore radius of tube-shaped pores
$\tau$	[m/m]	tortuosity defined as arc-chord ratio
$d_{\text{grain}}$	[m]	effective grain diameter
$f$	[/]	fraction of particles

$d_l$	[m]	lower sieve size limit
$d_u$	[m]	upper sieve size limit
$\eta$	[Pas]	dynamic viscosity
$\varrho$	[kg/m <sup>3</sup> ]	density
$g$	[kg/m <sup>2</sup> ]	gravitational acceleration (9.81 kg m <sup>-2</sup> )
$V_B$	[m <sup>3</sup> ]	volume of water away from the pore surface
$V_S$	[m <sup>3</sup> ]	volume of water in a layer at the pore surface
$R_S$	[1/s]	relaxation rate in a layer at the pore surface
$\rho$	[m/s]	surface relaxivity
$SSP$	[/]	sink strength parameter
$o$	[/]	mode index
$T_{ML}$	[s]	arithmetic mean of the logarithms of the $T$ distribution
$\rho_a$	[m/s]	apparent surface relaxivity
$C$	[m/s <sup>3</sup> ]	calibration constant
$\lambda$	[/]	regularisation factor
$q$	[As]	pulse moment
$I$	[A]	current
$t_{\text{pulse}}$	[s]	excitation pulse duration
$\mathbf{r}$	[m]	position vector
$\mathbf{B}_T$	[T]	component of the secondary magnetic tx field perpendicular to $\mathbf{B}_0$
$\mathbf{B}_R$	[T]	component of the secondary magnetic rx field perpendicular to $\mathbf{B}_0$
$\mathbf{b}_T$	[/]	unity vector of $\mathbf{B}_T$
$\mathbf{b}_R$	[/]	unity vector of $\mathbf{B}_R$
$\zeta$	[rad]	phase lag relative to $I$
$\mathbf{b}_0$	[/]	unity vector of $\mathbf{B}_0$
$\mathbf{G}$	[V/m <sup>2</sup> ]	2D sensitivity kernel
$\mathbf{G}^{1d}$	[V/m]	1D sensitivity kernel
$v^{\text{obs}}$	[V]	envelope of the measured NMR signal
$v^{\text{syn}}$	[V]	envelope of the synthetic NMR signal
$w_j$	[m <sup>3</sup> /m <sup>3</sup> ]	partial $w$ per time bin
$t_{\text{dteff}}$	[s]	effective dead time
$n$	[/]	time step/gate index
$c$	[/]	cell index
$l$	[/]	FID index
$p$	[/]	loop position index
$\mathbf{d}$	[V]	data space
$\mathbf{m}$	[m <sup>3</sup> /m <sup>3</sup> ; s]	model space
$\Phi$	[/]	objective function

## Contents

$\mathbf{W}_d$	[1/V]	error matrix
$\mathbf{W}_m$	[/]	first-order flatness matrix
$\epsilon$	[V]	error estimate
$r_z$	[/]	anisotropic factor
$\lambda$	[/]	regularisation factor
$\chi^2$	[/]	chi-squared value
$\mathbf{J}$	[/]	Jacobian matrix
$\alpha$	[/]	pore shape index

# 1. Introduction

The method of nuclear magnetic resonance (NMR) has been developed in the 1940s by Felix Bloch (Bloch et al., 1946) and Edward Mills Purcell (Purcell et al., 1946) for which both shared the Nobel Prize for Physics in 1952. The method proved to be a useful tool in geosciences especially since its application moved from the laboratory to the first borehole logging in 1960s (Brown and Gamson, 1960). About 20 years later Russian scientists successfully developed the technique of surface NMR (Semenov, 1987), which allows probing the subsurface to depths of about 100 m by using large wire loops placed at the surface (Weichman et al., 1999). Since then a growing community has been applying NMR to hydrological problems. The amplitude of the NMR signal is directly proportional to water content ( $w$ ) and, in case of full saturation, porosity ( $\phi$ ) which is a unique ability among geophysical techniques. Additionally, the measured exponential relaxing signals are the result of the interaction of protons in the fluid with each other and with the matrix at the pore surface. Assuming basic pore shapes, this allows relating the NMR relaxation time ( $T$ ) to the specific inner surface of a sample, i.e. the surface-to-volume ratio ( $S/V$ ) of the pores (Brownstein and Tarr, 1979).

The permeability ( $k$ ) is a fundamental property of a porous medium and a measure of the ability to transmit fluids. The parameter is highly complex and depends, among others, on the cross-section dimensions of its flow channels and the saturation of the material. In hydrogeological applications  $k$  is often replaced by the hydraulic conductivity ( $K$ ), which integrates the fluid properties viscosity and density, and therefore describes the ease of water to move through the pore space. The prediction of  $K$  is an important task in hydrology, essential for aquifer characterisation and hydraulic modelling. For fully saturated conditions, the Kozeny-Carman equation (Kozeny, 1927; Carman, 1938) relates  $k$  to the  $S/V$  of tube-shaped flow channels. Its application is very popular and discussed in detail, e.g. by Carrier (2003). To predict  $k$ , NMR has been proven to be very effective, e.g. Kenyon (1997). Among others, popular (semi-)empiric equations to predict  $k$  are those from SeEVERS (1966) and Kenyon et al. (1988). The latter is commonly used in rock physics and known as Schlumberger-Doll Research equation (SDR). While these equations are established for sandstones, they are used to some extent in shales (Josh et al., 2012),

## 1. Introduction

limestones (Akbar et al., 1995) and poorly consolidated reservoir sands (Kleinberg et al., 2003). For many hydrological applications in the near subsurface the properties of unconsolidated sediments are of particular interest. In contrast to sandstones, unconsolidated sediments show a large porosity and pore sizes up to several millimetres both leading to high  $K$  values. Wells placed in coarse unconsolidated sediments are generally very productive but show an increased vulnerability to pollution. The commonly used equations of SeEVERS (1966) and Kenyon et al. (1988) to predict  $k$  from NMR measurements are based on the assumption of fast diffusion (Brownstein and Tarr, 1979), which states that the self diffusion of the protons is fast enough that the entire pore is sampled during the relaxation process. This assumption may not be appropriate for the large pores commonly found in unconsolidated sediments. The first part of this thesis therefore investigates the following question: Can the prediction of  $k$  or  $K$  using NMR measurements on unconsolidated sediments be improved by a more general model not limited to the fast-diffusion approximation?

Surface NMR allows for a non-invasive characterisation of an aquifer. This can be an essential feature, for example when an aquiclude protecting an aquifer from pollution must not be penetrated by a borehole. Compared to laboratory or borehole application, the volume probed by surface NMR is huge. For each NMR experiment, the free propagation of the magnetic excitation field in the subsurface leads to a sensitivity function which shows an oscillating characteristic with depth. During a surface NMR survey several NMR experiments with different strengths of the excitation field and thus different sensitivity functions are conducted. Inversion is necessary to determine the spatial distribution of  $w$  and  $T$  in the subsurface. Several schemes are available to invert the recorded data set of free induction decays (FIDs) after a single pulse experiment. The initial value inversion (IVI) after Legchenko and Shushakov (1998) reduces all FIDs to their initial amplitudes, e.g. using a monoexponential fit. This scheme can therefore only derive the spatial  $w$  distribution. To obtain information about the spatial  $T$  distribution in the subsurface, time-step inversion (TSI) was introduced by Legchenko and Valla (2002). It basically consists of several IVIs conducted on different time steps of the FIDs, followed by a fitting of the derived  $w$  with an exponential function to obtain the spatial distribution of  $T$ . The inversion of surface NMR data was significantly improved by the introduction of the  $qt$  inversion (QTI) scheme (Mueller-Petke and Yaramanci, 2010). QTI considers the full FIDs of all experiments simultaneously and thus increases both spatial resolution and stability of the inverse problem. Commonly, the application of surface

NMR is restricted to 1-dimensional (D) targets. This allows using a single coincident (COI) transmitter (tx) and receiver (rx) loop and to interpret the collected data assuming 1D subsurface conditions. 2D targets may be investigated by combining multiple COI setups at different locations. However, to rely exclusively on COI can be time-consuming because only one data set is collected during each NMR experiment. Comprising separated tx and rx loop setups into one survey, e.g. half overlapping (HOL) or edge-to-edge (E2E) setups, leads to an increase in resolution especially at shallow depth (Hertrich et al., 2005, 2009). The development of multi-channel instrumentation made the use of separated loop setups efficient because several data sets can be collected simultaneously during each NMR experiment (Dlugosch et al., 2011). Current 2D IVI, using COI loop setups (Girard et al., 2007; Hertrich et al., 2007) or incorporating separate tx and rx loop setups (Hertrich et al., 2009), only allow to estimate the spatial  $w$  distribution. Under fully saturated conditions, it is therefore difficult to distinguish between fine and coarse-grained layers which is often essential to answer hydrological questions, e.g. for finding an optimal well location. To obtain the spatial distribution of  $T$ , and thus pore-size information, a 2D TSI was first presented by Walsh (2008). The second part of this thesis deals with the following questions: Can the resolution of the vertical 2D images of  $T$  and  $w$  obtained from 2D surface NMR surveys be improved by the development of a 2D QTI approach? And does the obtained 2D information of  $T$  lead to an improved characterisation of the subsurface?

The outline of this thesis is as follows. Chapter 2 covers the basic NMR principles and equations required for this thesis. This includes the origin of NMR amplitude and the different NMR relaxation times.

A review of the theory how to predict hydraulic conductivities in porous media and how to link them to NMR measurements is given in Chapter 3. The chapter starts with an overview of the commonly used equations and their derivations. To improve the prediction of  $K$  for coarse-grained, unconsolidated material from NMR measurements the new Kozeny-Godefroy model (KGM) is presented. The impact of the different model parameters are discussed and KGM is evaluated by data measured on well-sorted glass beads and quartz sand with grain sizes ranging from fine sand to fine gravel. The achieved results are compared to the commonly used SDR and SeEVERS equations and the benefit and limitations of KGM are discussed. The content of this chapter has already been published in Dlugosch et al. (2013).

Chapter 4 extends the theory presented in Chapter 2 by surface NMR specific information. The chapter covers the calculation of 3D sensitivity

## 1. Introduction

kernel ( $\mathbf{G}^{3d}$ ) for a NMR experiment, the forward calculation of surface NMR signals and details on different inversion schemes.

In Chapter 5, the 2D QTI approach is introduced. Several optimisations applied to the data and model domain to reduce the size of the inverse problem are presented. The improved features of the 2D QTI approach are demonstrated on a synthetic study and two field cases by comparing them to IVI and TSI results. The choice of regularisation parameters and the impact of the electric subsurface resistivity are discussed. With the exception of the Nauen field case (Chap. 5.4) the results presented in Chapter 5 have already been published in Dlugosch et al. (2014).

An extensive hydrogeophysical survey of the Schillerslage test site is presented in Chapter 6. The result of a 2D surface NMR survey is evaluated with respect to the resolved 2D structures and quality of the NMR parameters. The results of geological analyses on drill cores, an electrical resistivity tomography (ERT) survey and Earth's field, borehole and laboratory NMR measurements are compared and discussed. Additionally, this shows the method specific potentials of different NMR methods to characterise shallow aquifers. The prediction of the hydraulic conductivity using KGM is transferred from the laboratory to field application. Combining KGM with the 2D surface NMR result leads to a vertical 2D section of the hydraulic conductivity distribution in the subsurface.

The results of this thesis are summarised in Chapter 7. A detailed discussion on KGM and 2D QTI can be found in the respective subsections (Chap. 3.6 and 5.5). The thesis finish with a short outlook to point out several options for further improvements and studies.

# 2. Fundamentals of NMR

## 2.1. Principles

Matter is made of atoms. The method of NMR utilises one of the three basic physical properties of an atom nucleus, the nuclear spin ( $\hat{\mathbf{S}}$ ). Compared to the two remaining properties, mass and electric charge, the spin of a nucleus has only little obvious affect on the macroscopic behaviour of a material. Nevertheless, it provides scientists with a wonderful tool for spying on the microscopic and internal structure of objects without disturbing them (Levitt, 2002). The concept of a nuclear spin is highly abstract and originates from a quantum mechanical effect. Using two macroscopic effects, magnetic moment and angular momentum, to describe the impact of the nuclear spin in a descriptive way can therefore only be an approximation.

### Magnetic moment

The nuclear spin leads to a small magnetic moment ( $\hat{\boldsymbol{\mu}}$ ) for each nucleus which can be illustrated as a small bar magnet. Both parameters are linked by the nuclide specific gyromagnetic ratio ( $\gamma$ )

$$\hat{\boldsymbol{\mu}} = \gamma \hat{\mathbf{S}}, \quad (2.1)$$

and their axes are aligned in parallel ( $\gamma > 0$ ) for most nuclide. Because of its magnetic moment, a nucleus interacts with magnetic fields which can either originate from the molecular environment of the nucleus or from outside the sample. When all nuclei in a sample are exposed to an external static magnetic field ( $\mathbf{B}_0$ ), the magnetic moments try to align with  $\mathbf{B}_0$  to achieve a low energy state, but simultaneously get disturbed by the thermal energy of the system. For a sample in a thermal equilibrium at a temperature ( $\theta$ ), these two processes, after Curie's law, lead to a macroscopic net magnetisation ( $\mathbf{M}_0$ ) of

$$\mathbf{M}_0 = \frac{N_P \gamma^2 \hbar^2 \mathbf{B}_0}{4k_B \theta}, \quad (2.2)$$

with Planck's constant divided by  $2\pi$  ( $\hbar$ ), Boltzmann constant ( $k_B$ ) and number of nuclei per unit volume ( $N_P$ ) (see Fig. 2.1). The magnitude of  $\mathbf{M}_0$

## 2. Fundamentals of NMR

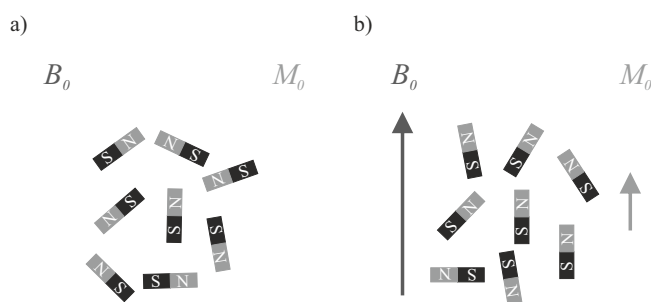


Figure 2.1.: Sketch of magnetic nuclei in thermal equilibrium.  $\mathbf{M}_0$  (a) in absence of a static magnetic field ( $\mathbf{B}_0$ ) and (b) in presence of  $\mathbf{B}_0$ .

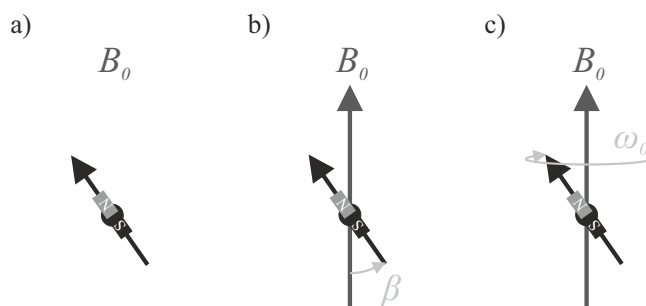


Figure 2.2.: Snapshot of a magnetic nucleus bearing a spin ( $\gamma > 0$ ) in absence of  $\mathbf{B}_0$  (a). Applying a static magnetic field ( $\mathbf{B}_0$ ) deviating by  $\beta$  from the orientation of the spin (b) results in a torque and thus in a precession of the magnetic spin axis on a cone around  $\mathbf{B}_0$  with  $\omega_0$  (c).

is commonly very small. Even for hydrogen, which has the highest  $\gamma$  of all nuclide ( $\gamma = 0.2675 \text{ rad s}^{-1} \text{ nT}^{-1}$ ),  $\mathbf{M}_0$  is about three orders of magnitude smaller than the effect due to the observed diamagnetism of water (Levitt, 2002). The amplitude of  $\mathbf{M}_0$  can be increased by strong artificial  $\mathbf{B}_0$ , but still is commonly not directly detectable as an increase in  $\mathbf{B}_0$ .

### Angular momentum

In absence of a  $\mathbf{B}_0$ , the spin axis of each nucleus in a sample may point in any possible direction. When exposed to a constant  $\mathbf{B}_0$ , spin axis deviating from  $\mathbf{B}_0$  by flip angle ( $\beta$ ) do not simply adjust in parallel to  $\mathbf{B}_0$  but precess at a constant angle  $\beta$  around  $\mathbf{B}_0$  (Fig. 2.2) This behaviour is similar to a spinning mass bearing an angular momentum, e.g. a gyroscope. Dependent on  $\mathbf{B}_0$  this precession occurs at a Larmor frequency ( $\omega_0$ ) which is characteristic

for each nuclide and is given by

$$\omega_0 = -\gamma \mathbf{B}_0 . \quad (2.3)$$

### NMR experiment

During a NMR experiment, magnetic moment and angular momentum of a nucleus are jointly addressed. Because a sample comprises a huge number of nuclei, the observable NMR effect on a sample in thermal equilibrium is commonly reduced to  $\mathbf{M}_0$ . A basic NMR experiment uses a constant  $\mathbf{B}_0$  and applies an electromagnetic pulse at the resonance frequency  $\omega_0$  to disturb the nuclei from their thermal equilibrium. This process, called excitation, is leading to a flip of the orientation of  $\mathbf{M}_0$  from  $\mathbf{B}_0$  by  $\beta$ . Due to the resulting coherent precession, the magnetic nuclei emit a small electromagnetic field at  $\omega_0$  observable after the excitation pulse.

## 2.2. Applications

The application of NMR is non-invasive, it can be conducted on samples in a solid, fluid or gas phase and is used in medicine, chemistry and physics. There are several NMR techniques which focus on different parameters of a NMR experiment.

NMR spectroscopy looks for small variations of  $\omega_0$  (Eq. 2.3). Using a very homogeneous  $\mathbf{B}_0$ , NMR can be used to identify nuclei due to their characteristic  $\omega_0$  or to obtain physical, chemical and structural information about molecules due to their shift in  $\omega_0$ .

When a NMR experiment is conducted under a well defined gradient field  $\mathbf{B}_0$ ,  $\omega_0$  can be used to image the spatial distribution of nuclei with a specific  $\gamma$ , e.g. hydrogen. This is called magnetic resonance imaging (MRI) and has a very popular application in medicine.

The NMR relaxometry focuses on the relaxation of the NMR signal after the excitation back to the thermal equilibrium which can be described by an exponential process with the NMR relaxation time ( $T$ ). This process can be monitored both in spectroscopy and MRI and is controlled by the interaction of the nuclei with their environment. In medical MRI,  $T$  allows to conclude about the pore or cell size of a tissue and thus is an important imaging parameter.

In geosciences, the application of NMR is primary limited by the difficulty to produce a well defined and strong  $\mathbf{B}_0$ . This is especially true when

## 2. Fundamentals of NMR

samples have a significant contrast in the magnetic susceptibility or for the cramped confines of a borehole. The used comparable low  $\mathbf{B}_0$  limits the application to NMR relaxometry and nuclei with high  $\gamma$ , i.e. hydrogen commonly found in water or petroleum.

### 2.3. Initial amplitude and water content ( $w$ )

The initial amplitude of the NMR signal can be recorded immediately after a short excitation of a sample and depends on  $\mathbf{M}_0$  and  $\beta$ . To achieve a maximum signal,  $\beta$  is normally controlled by the experimental setup to be  $\frac{1}{2}\pi$  or  $\frac{3}{2}\pi$  for all nuclei. Under these conditions the initial NMR amplitude is linear dependent on  $\mathbf{M}_0$ . For a NMR experiment conducted at known temperature ( $\theta$ ), static magnetic field ( $\mathbf{B}_0$ ) and nuclei with a known  $\gamma$ , this allows to conclude on the number of nuclei in the sample (Eq. 2.2).

A basic application using the initial NMR amplitude is the estimation of the number of hydrogen nuclei in a sample. If the volume of the sample is known, this allows to conclude about  $w$ , which under fully saturated conditions yields information about  $\phi$ . This can be done either by using detailed information about the experiment, i.e.  $\beta$  distribution in the sample and necessary input to calculate  $\mathbf{M}_0$  using Equation 2.2 ( $\mathbf{B}_0$ ,  $\theta$  and  $N_P$ ), or simply by relating the signal amplitude to a calibration measurement with a known amount of water.

### 2.4. NMR relaxation times ( $T$ )

After the excitation of the nuclei, the return to the thermal equilibrium is described by the Bloch equations (Bloch, 1946). Solution of the Bloch equations yields two independent relaxation processes, one perpendicular and the other aligned with  $\mathbf{B}_0$ , both of exponential character. Accordingly, they are described by respective time constants, the longitudinal NMR relaxation time ( $T_1$ ) for rebuilding the magnetisation aligned with  $\mathbf{B}_0$  and the transverse NMR relaxation time ( $T_2$ ) for the collapse of the magnetisation perpendicular to  $\mathbf{B}_0$ . For  $\mathbf{B}_0$  aligned in  $z$ -direction, the macroscopic net magnetisation ( $\mathbf{M}$ ) at a time ( $t$ ) after the excitation of the sample is given

## 2.4. NMR relaxation times ( $T$ )

by:

$$\mathbf{M}_z(t) = \mathbf{M}_0(1 - e^{-t/T_1}) , \quad (2.4)$$

$$\mathbf{M}_x(t) = -\mathbf{M}_0 \cos(\omega_0 t) e^{-t/T_2} , \quad (2.5)$$

$$\mathbf{M}_y(t) = \mathbf{M}_0 \sin(\omega_0 t) e^{-t/T_2} . \quad (2.6)$$

Both relaxation times,  $T_1$  and  $T_2$ , generally are of the same order of magnitude and follow the relation  $T_1 \geq T_2$ . They are often interpreted to yield similar information about a sample (Kleinberg et al., 1993) but the origin of both relaxation processes are different.

### Longitudinal NMR relaxation time ( $T_1$ )

The longitudinal NMR relaxation time ( $T_1$ ) describes the re-establishment of the thermal equilibrium and thus  $\mathbf{M}_0$  after a perturbation of the sample. In theory, a single nucleus with a spin axis deviating by  $\beta$  from a homogeneous  $\mathbf{B}_0$  would precess infinitely, never aligning with  $\mathbf{B}_0$ . However on a microscopic scale,  $\mathbf{B}_0$  experienced by each nucleus is neither homogeneous nor constant but affected by molecules or other magnetic particles which are all in thermal motion. Therefore, a single nucleus samples small variations in the direction of  $\mathbf{B}_0$  which is enough to bring down the theory of a precession on a constant cone around the macroscopic  $\mathbf{B}_0$ . Over time the spin of a single nucleus roams all possible  $\beta$  which, on a macroscopic scale, allows to establish a new thermal equilibrium at a rate  $T_1$ .

### Transverse NMR relaxation time ( $T_2$ )

After an excitation of a sample which leads to a macroscopic change in the orientation of  $\mathbf{M}$ , the transverse NMR relaxation time ( $T_2$ ) describes the decay of the observed macroscopic amplitude of  $\mathbf{M}$  in the plane perpendicular to  $\mathbf{B}_0$ . The thermal motion of a nucleus in an environment of molecules or other magnetic particles leads to small changes in the observed amplitude of  $\mathbf{B}_0$  experienced by each nucleus and thus  $\omega_0$  (Eq. 2.3). This loss in coherence in the precession of the spin axes around  $\mathbf{B}_0$  leads, after some time, to an extinction of parts of the NMR signal. Because the variations in  $\mathbf{B}_0$  observed by each nucleus are random, this decay is irreversible leading to a random distributed orientation of the spin axes in the plane perpendicular to  $\mathbf{B}_0$  when the sample reaches the thermal equilibrium. Therefore, the  $T_2$  including dephasing ( $T_2^*$ ) estimated by a simple FID experiment is commonly significantly shorter than  $T_2$ .

## 2. Fundamentals of NMR

If a nucleus moves in a static and defined field-strength gradient ( $\Delta\mathbf{B}_0$ ), part of the observed dephasing of the  $T_2$  signals is reversible. Its impact on  $T_2$  can be reduced using a Carr-Purcell-Meiboom-Gill (CPMG) pulse sequence (Carr and Purcell, 1954; Meiboom and Gill, 1958). The effectiveness depends on the inter-echo spacing of the CPMG sequence ( $t_{es}$ ) and the self-diffusion constant ( $D$ ) of the fluid and, as a first approximation, can be described as an additional  $T$  due to diffusion ( $T_D$ ) (Kleinberg and Horsfield, 1990):

$$\frac{1}{T_2} = \frac{1}{T_{2o}} + \frac{1}{T_D} = \frac{1}{T_{2o}} + \frac{D(\gamma\Delta\mathbf{B}_0 t_{es})^2}{12}. \quad (2.7)$$

$T_D$  acts in series with the  $T_2$  due to all other processes ( $T_{2o}$ ), which for example includes the relaxation of nuclei on surfaces, as described in Chapter 3.2.

# 3. The link between NMR and hydraulic conductivity ( $K$ )<sup>1</sup>

## 3.1. Fluid flow in porous media

The equation of Kozeny (1927) and Carman (1938) can be used to predict  $k$  of an unconsolidated sample from basic information about the sample matrix (e.g. Carrier, 2003). The equation is based on a simple model of parallel tube-shaped pores defined by a respective pore radius ( $r_{\text{tube}}$ ). Including a modification to estimate  $k$  (e.g. Pape et al., 2006) the Kozeny-Carman equation is given by:

$$k_{\text{KC}} = \frac{1}{8\tau^2} \phi r_{\text{tube}}^2, \quad (3.1)$$

with  $\phi$  and tortuosity ( $\tau$ ).

Equation 3.1 can be converted from the original description of tube-shaped pores to other (matrix) geometries using an equivalent  $S/V$ . Assuming smooth and spherical grains which can be described by an effective grain diameter ( $d_{\text{grain}}$ ), simple geometric considerations leads to

$$r_{\text{tube}} = \frac{1}{3} \frac{\phi}{1 - \phi} d_{\text{grain}}, \quad (3.2)$$

which allows for estimating  $k$  based on sieving analyses. In this work the effective grain diameter after Carrier (2003)

$$d_{\text{grain}} = 1 / \sum_i \frac{f_i}{d_{li}^{0.5} d_{ui}^{0.5}} \quad (3.3)$$

is used, with fraction of particles ( $f$ ) between the respective sieve sizes limits  $d_l$  and  $d_u$ .

In hydrological application  $k$  is often replaced by  $K$ , which integrates the fluid properties dynamic viscosity ( $\eta$ ) and density ( $\rho$ ) under gravitational acceleration ( $g$ ). Under fully saturated conditions,  $K$  can be written as

$$K = \frac{\rho g}{\eta} k. \quad (3.4)$$

---

<sup>1</sup>The content of this chapter has been published in R. Dlugosch et al. (2013). Improved prediction of hydraulic conductivity for coarse-grained, unconsolidated material from nuclear magnetic resonance. *Geophysics* 78(4), EN55–EN64. DOI: 10.1190/geo2012-0187.1

### 3. The link between NMR and hydraulic conductivity ( $K$ )

Because of the primary hydrological application in unconsolidated material this work focusses on the determination of  $K$  and adapts the following equations appropriately. Combining Equation 3.1 to 3.4, the Kozeny-Carman equation for predicting  $K$  from sieving analyses reads:

$$K_{\text{KC}} = \frac{\varrho g}{72\eta\tau^2} \frac{\phi^3}{(1-\phi)^2} \left( \sum_i \frac{f_i}{d_{li}^{0.5} d_{ui}^{0.5}} \right)^{-2}. \quad (3.5)$$

Beside the temperature dependency of  $K$  due to  $\eta$  and  $\varrho$  (see Tab. 3.1), most results presented in this paper are equally true for  $k$  and can be transferred using Equation 3.4.

## 3.2. NMR in porous media

One of the first models which describes  $T_1$  observed on water in the pores of a solid was presented by Seevers (1966). It consists of two processes: the bulk water relaxation ( $T_B$ ) in the main volume of water ( $V_B$ ) and a fast relaxation in a thin layer with a volume  $V_S$  that is in contact with the grain surface and characterised by relaxation rate ( $R_S$ )

$$\frac{1}{T_1} = \frac{1}{T_B} + R_S \frac{V_S}{V_B}. \quad (3.6)$$

This relation links the NMR signal to the  $S/V$  of the pore and therefore allows to derive hydraulic properties.

Brownstein and Tarr (1979) introduced a simple diffusion model, valid for  $T_1$  and  $T_2$ , which links the measured  $T$  to pores with basic shapes including tubes. The model accounts for the  $D$  of water and the average sink strength density of the pore surface or surface relaxivity ( $\rho$ ) but neglects the impact of  $T_B$ . The material-specific  $\rho$  describes the interaction of the protons with the pore surface. The authors distinguish two limiting cases (fast diffusion and slow diffusion) depending on the sink strength parameter ( $SSP$ ), given by

$$SSP = \rho r_{\text{tube}}/D. \quad (3.7)$$

For each case, a separate equation is presented linking  $T$  and pore size.

Solving the governing differential equations for fast-diffusion conditions ( $SSP \ll 1$ ), also called  $\rho$  controlled, results in one dominant NMR signal which is the first-order solution, i.e. the main mode ( $o = 0$ ). The solution basically matches the formulation of Seevers (1966) (Eq. 3.6) without  $T_B$  and reads

$$\frac{1}{T} = \rho \frac{S}{V}, \quad (3.8)$$

with pore surface ( $S$ ) and pore volume ( $V$ ). For a single water filled pore this results in a primarily monoexponential signal. If a certain pore size corresponds to a monoexponential signal, then a distribution of pore sizes within one sample will lead to a measured multiexponential signal, i.e. a distribution of partial  $w$  ( $w_j$ ) with respective relaxation times. Assuming a constant  $\rho$  this leads to a linear relationship between pore size and relaxation time distribution. Commonly, the weighted geometric mean, also called arithmetic mean of the logarithms ( $T_{ML}$ ) of a distribution of  $T_j$

$$\ln(T_{ML}) = \frac{\sum_j w_j \ln(T_j)}{\sum_j w_j}, \quad (3.9)$$

with respective weighting factor  $w_j$  (Brown and Fantazzini, 1993; LaTorraca et al., 1993; Dunn et al., 2002) is used to represent a sample, i.e. to represent a sample by a mean pore size

For the slow-diffusion case ( $SSP \gg 10$ ), also called  $D$  controlled, the relation between  $T$  and the pore size changes. The observed NMR signal from a single pore becomes multiexponential due to the higher order solutions of the differential equations. The relaxation times of these higher modes ( $o > 0$ ) are significantly faster than the main mode and their amplitudes sum up to a significant amount of the total signal for increasing values of  $SSP$ . Consequently, a  $T$  distribution may not purely originate from a pore radius distribution and  $T_{ML}$  no longer represent a mean pore size of a sample. The region of intermediate-diffusion ( $1 \leq SSP \leq 10$ ) is not explicitly described by Brownstein and Tarr (1979).

While Brownstein and Tarr (1979) gave separate equations for the slow- and fast-diffusion case, Godefroy et al. (2001b) found a solution that describes the main mode ( $o = 0$ ) for the complete range of  $SSP$ , by excluding very early times in the NMR relaxation, i.e. neglecting higher modes ( $o > 0$ )

$$\frac{1}{T} = \frac{1}{T_B} + \frac{1}{\frac{r_{\text{tube}}}{2\rho} + \frac{r_{\text{tube}}^2}{4D}}. \quad (3.10)$$

Obviously, using the relaxation time of the zeroth mode to estimate a pore radius is correct only if a single radius is present, i.e. a relaxation-time distribution is due to higher modes and not due to a distribution of pore sizes.

In addition to the described processes,  $T_2$  can be influenced by the movement of the protons in a magnetic gradient field due to diffusion (Kleinberg and Horsfield, 1990). However, this effect (Equation 2.7) is

### 3. The link between NMR and hydraulic conductivity ( $K$ )

usually neglected when using a CPMG pulse sequence conducted at a low NMR frequency and with a short pulse spacing. Under these conditions  $T_2$  and  $T_1$  yield identical pore-size information (Kleinberg et al., 1993). The subsequent equations are therefore referred to  $T$ , which is valid for  $T_2$  only under the described limitations, i.e. negligible magnetic field gradients. Because generally  $T_1 \geq T_2$ , this leads to relaxation time specific  $\rho$ .

Usually fast-diffusion conditions are assumed (e.g. Kenyon, 1997) to estimate  $\rho$  of a sample which consequently allows to use Equation 3.8. Therefore,  $T$  and  $V$  are estimated by a NMR experiment and  $S$  is measured independently using a different method, for example section images (e.g. Straley et al., 1987), hydraulic conductivity (e.g. Kenyon et al., 1989), nitrogen adsorption or NMR-diffusion measurements (e.g. Hürlimann et al., 1994). Because all of these methods have an individual sensitivity to the roughness of the pore surface, this leads to a wide variation of  $S$  and  $\rho$  of up to a factor of 10 and more. Therefore, Kenyon (1997) introduced an effective or apparent surface relaxivity ( $\rho_a$ ) when relating NMR to hydraulic measurements. Consequently,  $\rho_a$  is used for the samples presented in this study.

### 3.3. Predicting $K$ from NMR measurements

To predict  $k$  from NMR measurements, an analytic solution can be achieved by combining the Kozeny-Carman (Eq. 3.1) with Equation 3.6 as presented by Seevers (1966). Including the fluid properties to predict  $K$  using Equation 3.4 leads to the Seevers model including bulk water relaxation (SB)

$$K_{SB} = C_{SB}\phi \left( \frac{T_B T}{T_B - T} \right)^2 . \quad (3.11)$$

The same result can be achieved using Kozeny-Carman (Eq. 3.1) and the fast-diffusion approximation after Brownstein and Tarr (1979) (Eq. 3.8) and additionally include the effect of  $T_B$ . Therefore, the calibration constant ( $C$ ) can be expressed by  $C_{SB} = (\rho g \rho^2) / (2\eta \tau^2)$ , comprising the matrix properties ( $\rho$  and  $\tau$ ) and fluid properties ( $\rho$ ,  $\eta$  and  $g$ ).

In analogy to the Kozeny-Carman equation but derived empirically, Kenyon et al. (1988) presented an equation to predict  $k$  from NMR measurements. It is based on several data sets measured on sandstones and is commonly known as SDR

$$K_{SDR} = C_{SDR}\phi^4 T^2 . \quad (3.12)$$

### 3.4. The new Kozeny-Godefroy model (KGM)

SDR and SB comprise several parameters, like pore geometry and surface relaxivity, as well as temperature-dependent fluid parameters into the empiric factors  $C_{SB}$  and  $C_{SDR}$ . These factors are obtained from calibration measurements for each sandstone formation or material. Ranges for  $C_{SB}$  and  $C_{SDR}$  can be found in literature, e.g. for sandy material summarised by Mohnke and Yaramanci (2008) to predict  $K$  for a temperature of 10 °C. Due to the limitations or data sets used to estimate Equation 3.11 and 3.12 they are summarised as fast-diffusion approximations.

Other semi-empirical approaches were published by Timur (1968) and Coates and Dumanoir (1973) which can also be traced back to the Kozeny-Carman equation. Due to the lack of bound water for the coarse and clay-free material of the presented samples, Timur-Coates like equations cannot be applied successfully and are therefore not further discussed in this work.

The presented SDR and SB differ (i) in the porosity exponent (4 and 1) and (ii) by neglecting and accounting for bulk water relaxation, respectively. Note that the porosity exponent is subject to discussion (Kenyon et al., 1988; Mavko and Nur, 1997). Because the presented samples in this work show only minor variations of  $\phi$ , this work cannot contribute any information to this discussion. For a constant  $\phi$ , the different porosity exponents in SDR and SB only lead to a constant factor which can be simply included into the empiric calibration constants of both equations. Therefore in this work, SDR and SB differ primarily due to the influence of  $T_B$  for long relaxation times.

## 3.4. The new Kozeny-Godefroy model (KGM)

### 3.4.1. Derivation

In order to obtain a model to estimate  $K$  from NMR measurements on unconsolidated material, Kozeny-Carman (Eq. 3.1) is combined with Godefroy (Eq. 3.10) and converted to  $K$  using Equation 3.4. Note that the main requirements of Kozeny-Carman and Godefroy persist. The model is referred to as Kozeny-Godefroy model (KGM)

$$K_{\text{KGM}} = \frac{\rho g}{8\tau^2\eta} \phi \left( \frac{-D}{\rho} + \sqrt{\left(\frac{D}{\rho}\right)^2 + \frac{4DT_B T}{T_B - T}} \right)^2. \quad (3.13)$$

This allows to estimate  $K$  by (i) measuring  $\phi$  and  $T$  using NMR, (ii) obtaining  $T_B$ ,  $\eta$ ,  $D$  and  $\rho$  from literature or separate measurements and

### 3. The link between NMR and hydraulic conductivity ( $K$ )

adapting them to the sample temperature and (iii) calibrating  $\rho$  and  $\tau$  or assuming values from literature. In cases where the impact of  $T_D$  on the NMR measurement is known, e.g. when using a NMR borehole tool with a limited echo spacing, the effect of  $T_D$  can be summarised into the resulting  $T_B$  value. The sensitivity of KGM to its model parameters is discussed in the following.

#### 3.4.2. Sensitivity to model parameters

The KGM (Eq. 3.13) depends on several model parameters. Some of them cannot be estimated by a simple NMR experiment but need to be chosen using additional information. Apart from  $g$ , they can be subdivided into sample or matrix specific parameters ( $\rho$ ,  $\phi$  and  $\tau$ ) and fluid parameters ( $T_B$ ,  $\eta$ ,  $D$  and  $\varrho$ ). Their impact on KGM is discussed individually, with exception of the fluid parameters which are summarised as the effect on KGM due to temperature variations of water. The parameters  $\rho = 50 \mu\text{m s}^{-1}$ ,  $\phi = 0.35$ ,  $\tau = 1.5$  and a temperature of  $20^\circ\text{C}$ , i.e.  $\theta = 293.15 \text{ K}$ , were chosen as the default model. These values are based on observations and expectations for clay free unconsolidated material and are referenced and discussed in more detail in the respective paragraph. The successive variation of one specific model parameter from the default model is presented in Figure 3.1.

The impact of the surface relaxivity on KGM is discussed focusing on the left part of Figure 3.1a. For a given pore size, e.g. resulting in  $K = 10^{-3} \text{ m s}^{-1}$ , an increase in  $\rho$  has two effects. (i) The measured  $T$  of the main mode is reduced and (ii) the diffusion condition gradually changes from fast to slow diffusion. Neglecting the impact of  $T_B$ , the dependency of  $K$  from  $T$  changes from  $K \propto T^2$  for the fast-diffusion case gradually to  $K \propto T$  for the slow-diffusion case, where  $T$  is finally no longer a function of  $\rho$ . This leads to a physical upper limit of  $K$  for a measured  $T$  and  $\phi$ . For long  $T$  (right side of Figure 3.1a)  $T_B$  starts dominating  $T$  and therefore the estimation of  $K$ . Assuming a constant fluid chemistry,  $T_B$  of water is mainly controlled by the temperature.

The impact of temperature ( $\theta$ ) on KGM is evaluated focusing on the temperature range between  $10$  and  $30^\circ\text{C}$ , typical for the laboratory and shallow field applications. Figure 3.1b shows the dominant impact of  $T_B$  for long  $T$ , commonly observed in coarse material. Consequently,  $K$  on coarse material can only be estimated reliably if  $T_B$  is well determined. However, the effect of temperature on KGM is not limited to  $T_B$ . More fundamentally, a variation in  $\theta$  changes the fluid viscosity  $\eta$  which affects samples of all grain sizes. On the NMR part of KGM, a change in  $\eta$

### 3.4. The new Kozeny-Godefroy model (KGM)

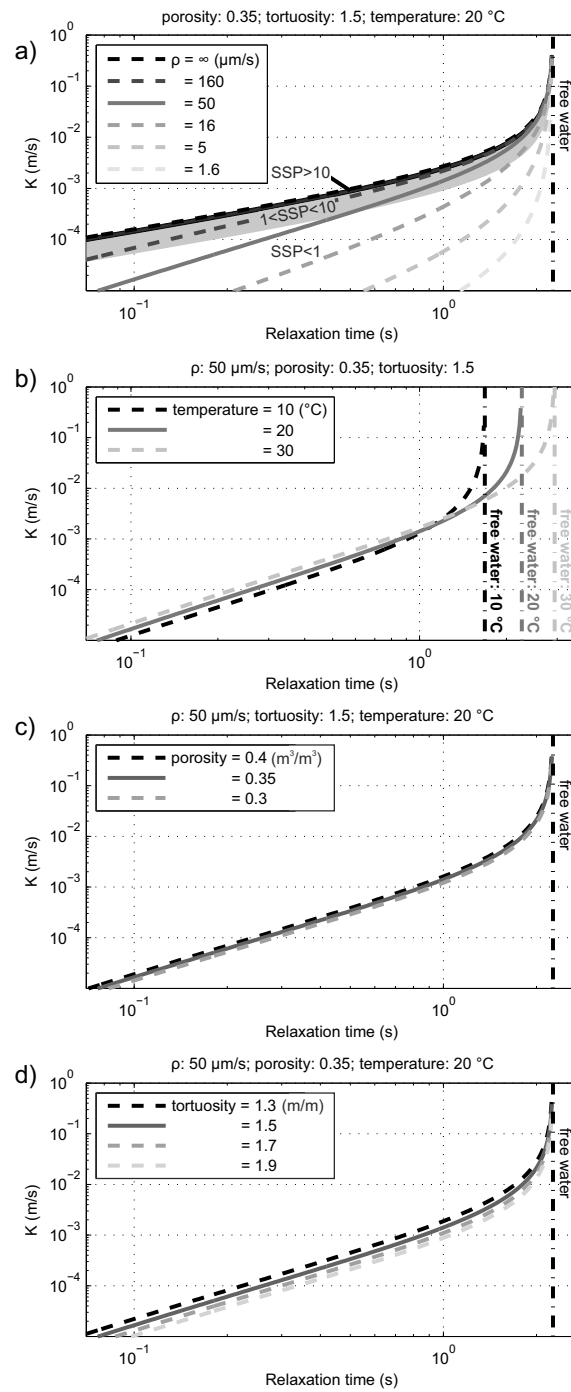


Figure 3.1.: Sensitivity of KGM to variation of the model parameters surface relaxivity, temperature, porosity and tortuosity (from a to d). The default model is marked by continuous lines. Regions of intermediate ( $1 \leq SSP \leq 10$ ) and slow diffusion ( $SSP \leq 10$ ) are shaded (a).

### 3. The link between NMR and hydraulic conductivity ( $K$ )

	Equation	Reference
$T_B$	$3.3 + 0.044(\theta - 308.15)$	own $T_2$ measurements
$\eta$	$(1002, 797 \text{ and } 653) \times 10^{-6}$ for (20, 30 and 40) °C	tabular (Kestin et al., 1978)
$D$	$20.24 - 0.180\theta + 0.0004031\theta^2$	Dunn et al. (2002)
$\rho$	$1000 - \frac{\theta + 15.83}{508.92(\theta - 277.13)}(\theta - 3.98)^2$	McCutcheon et al. (1993)

Table 3.1.: Physical properties of water and their dependency from the temperature ( $\theta$ ) in Kelvin. The equation for  $T_B$  was approximated by an empirical fit on continuous  $T_2$  measurements during the warm up of tap water from 5 to 35 °C.

affects  $D$  and  $T_B$  and in consequence the NMR relaxation. For example, a lower fluid temperature leads not only to a shift of  $T_B$  to shorter  $T$  but additionally to a reduction in  $D$ . Therefore, the sample might leave the fast-diffusion condition if  $SSP \ll 1$  is violated (Eq. 3.7) and higher modes, i.e. multiexponential NMR signals, might be observed. On the flow part of KGM, a change in  $\eta$  affects the macroscopic flow and therefore  $K$ . Despite its complex impact on KGM, the fluid temperature can be easily measured in the laboratory and borehole or approximated for field applications. The temperature dependency of  $\eta$ ,  $D$  and  $T_B$  of the fluid can either be gained from the literature or from separate measurements (e.g. see Tab. 3.1).

The expected range of porosity for unconsolidated, well-sorted and clay-free material is rather small. Because KGM uses a tube-shaped pore model, porosity contributes linearly to  $K$ , thus leading to relatively small changes (Fig. 3.1c). Under fully saturated conditions,  $\phi$  can be easily estimated from the amplitude of the NMR signal.

Similar to  $\phi$ , the expected range of tortuosity for clay-free and well-sorted unconsolidated material is small and leads to a small shift in  $K$  (Fig. 3.1d). However, for higher values of  $\tau$ , e.g. as found on sandstones, its effect can become significant due to its quadratic term. For this study a mean value of 1.5 was chosen that lies between  $\pi/2$  after Bartell and Osterhof (1928) and  $\sqrt{2}$  after Carman (1956). It is also in good agreement with Pape et al. (2006), who estimated  $\tau = 1.5$  from NMR diffusion measurement on glass beads.

## 3.5. Experimental validation of KGM

### 3.5.1. Sample material and preparation

To be able to provide samples of homogeneous material and grain shape over a wide range of grain sizes ( $d_{\text{grain}}$  between 90  $\mu\text{m}$  and 4.4 mm) glass beads were chosen for evaluating the Kozeny-Godefroy model. The beads (Sigmund Lindner GmbH, Warmensteinach, Germany) consist of soda lime glass with a chemical composition of mainly  $\text{SiO}_2$ : 54.7 %,  $\text{Al}_2\text{O}_3$ : 14.5 %,  $\text{CaO}$ : 22.5 % and  $\text{B}_2\text{O}_3$ : 5.5 %. The particles are spherically shaped and split into samples with narrow grain size ranges as shown in Table 3.2. Additionally, a set of sand samples with high quartz content (Euroquarz GmbH, Dorsten, Germany) but natural grain shapes is used to show the applicability of KGM to predict  $K$  on natural material.

To be able to visually check the correct installation of the material a lucent polycarbonate sample holder was used with a length of 110 mm and an inner diameter of 40 mm. The dimension was chosen to be large enough to hold a representative volume of the material but still fit in the coil of the used laboratory-NMR.

The samples were saturated with degassed and deionised water, doped with sodium chloride to reach an electrical conductivity of 400  $\mu\text{S cm}^{-1}$ . The sample holder was first filled with fluid to which the grains were slowly added to prevent air pockets. The material was gradually filled and compacted with a pestle to achieve a homogeneous porosity.

### 3.5.2. $K$ measurements

The hydraulic conductivity ( $K_{\text{meas}}$ ) of the samples were estimated using the constant-head setup. A fundamental assumption for this experiment is to maintain laminar flow conditions which is challenging for coarse material. Therefore, the Reynolds numbers for flow in a tube and packed bed were estimated for each measurement. Additionally, the experiments were conducted with different flow rates and checked for consistence. The temperature of the fluid was measured and  $K_{\text{meas}}$  was corrected to a common temperature of 22 °C using Equation 3.4 to make  $K$  consistent with the thermal equilibrium reached during the NMR measurements. To estimate the error of  $K_{\text{meas}}$ , a quadratic propagation of uncertainty from all input parameters was assumed. The results were compared to  $K_{\text{KC}}$  (Fig. 3.2) obtained from sieving analyses using the Kozeny-Carman equation to predict  $K$  (Eq. 3.5) assuming  $\tau = 1.5 \pm 0.1$ . The range of geometric parameters

### 3. The link between NMR and hydraulic conductivity ( $K$ )

Material	$d_{\text{grain}}/\mu\text{m}$ (sieving)		$\phi$ (NMR)	$\rho_a/\mu\text{m s}^{-1}$ ( $T_2$ )		$SSP$ ( $T_2$ )		$\rho_a/\mu\text{m s}^{-1}$ ( $T_1$ )		$SSP$ ( $T_1$ )	
	Upper	Lower		Upper	Lower	Upper	Lower	Upper	Lower	Upper	Lower
Glass beads	4400	3600	0.39	$\infty$	0	$\infty$	0.6	$\infty$	0	$\infty$	0.2
	1650	1250	0.35	160	0	$\infty$	1.5	160	0	11	0.7
	500	250	0.38	54	38	2.8	0.8	43	30	2.0	0.6
	150	90	0.37	66	55	0.9	0.4	42	35	0.6	0.2
Quartz sand	2000	630	0.41	297	0	13	0.9	232	0	13	0.2
	1000	500	0.38	73	20	11	1.1	74	18	13	1.0
	500	125	0.34	44	34	1.5	0.5	22	14	0.6	0.3
	250	63	0.40	41	31	0.6	0.2	37	30	0.6	0.2

Table 3.2.: List of the sample parameters: material, effective grain diameter ( $d_{\text{grain}}$ ) and porosity ( $\phi$ ). The apparent surface relaxivity ( $\rho_a$ ) and sink strength parameter ( $SSP$ ) of the samples derived from KGM using the individual measured porosity ( $\phi$ ),  $K_{\text{meas}}$  and respective  $T_1$  or  $T_2$  values of each sample. The range of  $\rho_a$  and  $SSP$  is derived from the error range of the input parameters.

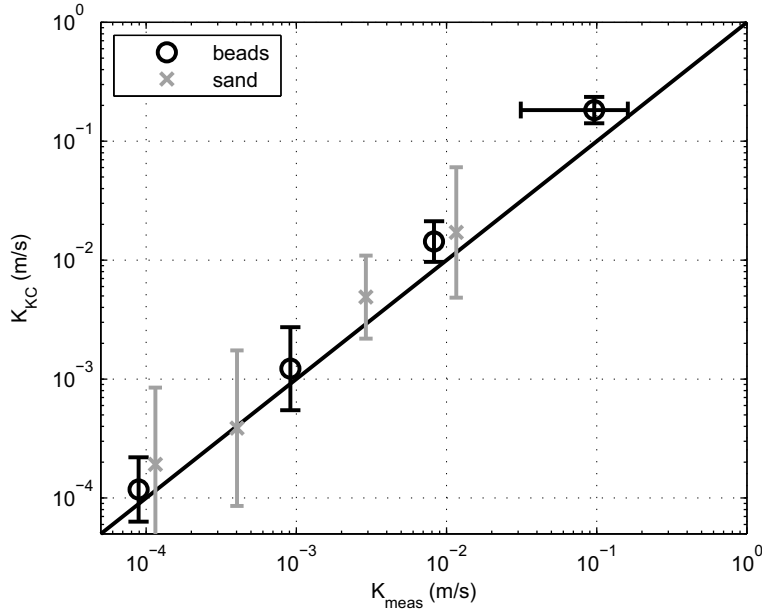


Figure 3.2.: Comparison of  $K$  measured by flow experiment and predicted using sieving analyses and the Kozeny-Carman equation on glass beads and quartz sand samples. The black line marks the identity. Error bars smaller than marker size are not shown.

$d_{\text{grain}}$  and  $\phi$  measured on each sample were used to estimate an error for  $K_{KC}$ . A good agreement can be observed between  $K_{KC}$  and  $K_{meas}$  within their error levels which supports the use of the tube-shaped pore model for well-sorted, clay-free material. The small trend to overestimate  $K_{KC}$  might be explained by an underestimation of  $S/V$  assuming spherical and smooth grains. This could have been accounted for by an increase of  $\tau$  to 1.7, which is still within the expected range of the shape factor for non-spherical grains as, e.g. reported by Carrier (2003).

### 3.5.3. NMR measurements

The NMR measurements were carried out using the Rock Core Analyzer (Magritek, Wellington, New Zealand) which operates at 2 MHz. The built-in cooling system was used to ensure a constant sample temperature between 21 and 22 °C during the measurements.

The  $T_1$ -relaxation was measured by an inversion recovery experiment using 50 logarithmically spaced delays ranging from 0.01 to 15 s. To determine  $T_2$ , a CPMG pulse sequence with an echo spacing of 200  $\mu\text{s}$  was applied

### 3. The link between NMR and hydraulic conductivity ( $K$ )

and logarithmically resampled to 500 data points. To obtain a  $T_1(T_2)$  distribution from the data, an inversion was conducted to estimate the  $w_j$  for 150 (300) logarithmically spaced time bins between 0.01 to 10 s.

Because  $T_B$  is not only a function of temperature but can be altered by dissolved ions,  $T_B$  was estimated separately for every sample. Therefore, the pore fluid was extracted and  $T_2$  of the liquid was measured after the NMR experiments on the sample.

Estimating a representative  $T$  value or  $T$  distribution of a sample is essential to conclude on hydraulic properties using NMR. Figure 3.3 exemplary shows a  $T_2$  distribution derived by a smooth multiexponential fitting (see, e.g. Whittall et al., 1991). To weight between minimum structure in the  $T$  distribution and minimum residual between measured data and model response a regularisation factor ( $\lambda$ ) is used. Additionally, a single pore mode (SPM) fit after Ronczka et al. (2012) is presented for comparison. The SPM approach calculates the first 10 modes of a single pore after Brownstein and Tarr (1979) and adapts  $r_{\text{tube}}$  and  $\rho$  accordingly. Both, smooth and SPM fit, explain the data comparably well, and therefore show that modes may not be ignored for coarse material. Additionally,  $T$  of the main mode agrees well with the maximum of the smooth distribution. This supports the assumption that the presented sample can be described by a single pore radius whose information is comprised in the maximum of the smooth distribution. Therefore, this maximum was used in this work in analogy to Godefroy et al. (2001a).

To estimate the error of the calculated  $T$ ,  $\lambda$  of the smooth inversion was varied to estimate the range of  $T$  which sufficiently explains the measured data without leaving structure in the residual and without increasing the misfit significantly above the noise level. For the samples presented in this work the relative error of  $T$  is in the range of 0.05.

## 3.6. Benefits and limitations of KGM

### 3.6.1. Evaluation of KGM

The results for the measured  $T_2$  and  $K_{\text{meas}}$  on glass beads and sand are presented in Figure 3.4. Contour lines of KGM for a range of  $\rho$  from  $5 \mu\text{m s}^{-1}$  to  $\infty$ , a fixed mean sample porosity of 0.38 and a fluid temperature of  $22^\circ\text{C}$  are plotted for comparison. The value of  $T_B = 2.39 \text{ s}$  has been estimated by separate NMR measurements on all sample fluids. The two different sample types (sand and glass beads) line up on respective contour lines of constant

### 3.6. Benefits and limitations of KGM

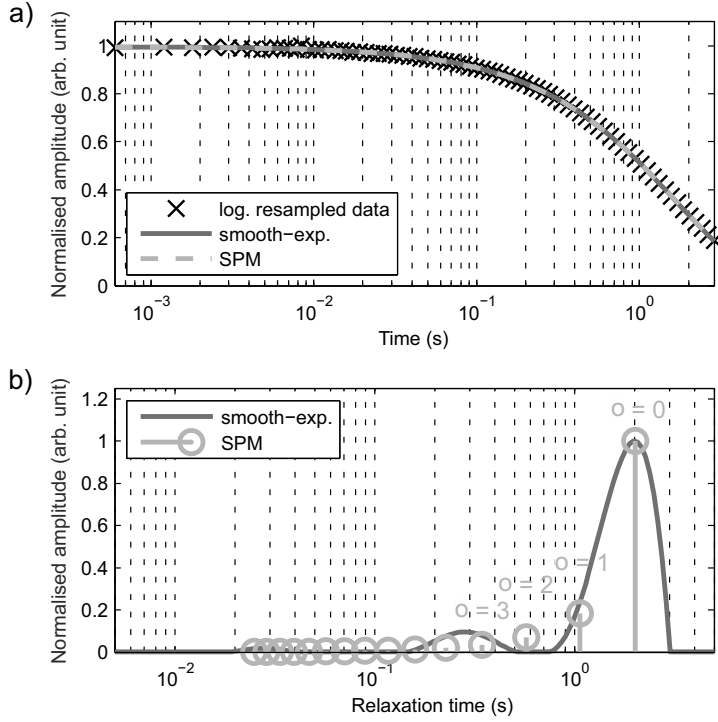


Figure 3.3.: Logarithmically equidistant resampled  $T_2$  relaxation curve of water-saturated glass beads with a grain size of 1250 to 1650  $\mu\text{m}$  and fitted  $T$ -models with a smooth distribution and using single pore mode (SPM) model (a). Distribution of the fitted modes including the mode number  $o$  (b).  $\text{RMS}(\text{smooth}) = 2.29 \times 10^{-4}$  and  $\text{RMS}(\text{SPM}) = 2.35 \times 10^{-4}$ .

$\rho$ . However, this visual comparison is somehow limited because, apart from a variation of  $\rho$ , Figure 3.4 only shows a mean KGM with otherwise fixed model parameters. Therefore, this mean KGM does not account for variations of the sample porosity, which deviates up to 0.03 from the mean KGM, nor does it reflect the uncertainty of the mean KGM due to the used input parameters. The main impacts on KGM are expected from  $T_B$ , with an error of  $\pm 0.07$  s estimated from extracted sample fluids, or  $\tau$ , with  $\pm 0.01$  approximated from  $\phi$  variation after Lanfrey et al. (2010).

To overcome these limitations the surface relaxivity has been calculated for every sample, by rearranging Equation 3.13 to solve  $\rho$  and using the sample specific values of  $\phi$ . Because the samples in this work have an unknown pore roughness, these values are referred to as apparent surface relaxivity ( $\rho_a$ ). The ranges of  $\rho_a$ , obtained by a quadratic propagation of uncertainty for all input parameters, are listed in Table 3.2. Examination

### 3. The link between NMR and hydraulic conductivity ( $K$ )

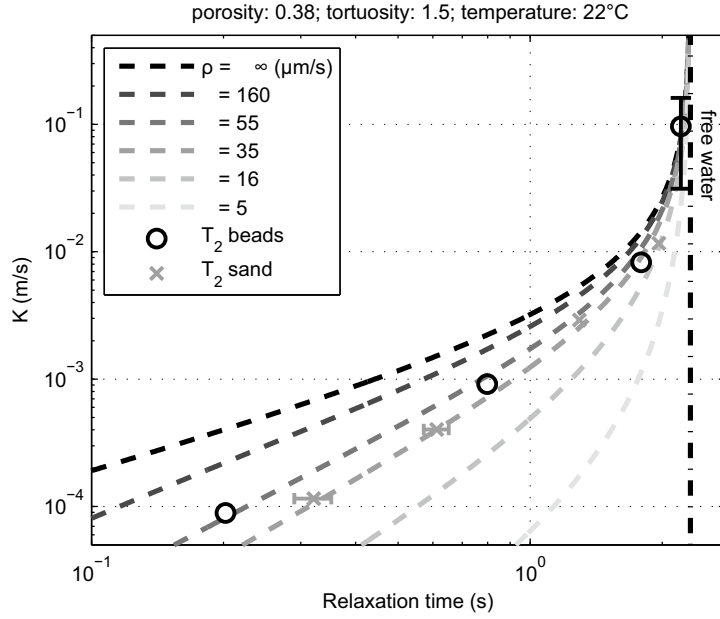


Figure 3.4.: Kozeny-Godefroy model for a constant porosity of 0.38,  $T_B$  of 2.39 s, a temperature of 22 °C and varying surface relaxivity ( $\rho$ ). Measured  $T_2$  relaxation times and  $K_{\text{meas}}$  on glass beads and quartz sand samples with different grain sizes. Error bars smaller marker sizes are not shown.

of the  $\rho_a$  ranges suggest that  $55 \mu\text{m s}^{-1}$  might be a reasonable value when applying  $T_2$  measurements on glass beads. For sand the respective  $\rho_a$  seems to be slightly lower ( $35 \mu\text{m s}^{-1}$ ). For  $T_1$ , the respective  $\rho_a$  are  $\approx 37 \mu\text{m s}^{-1}$  for glass beads and  $\approx 30 \mu\text{m s}^{-1}$  for sand. These values are in the range of surface relaxivities found in the literature (see Tab. 3.3) if the inner surface of a sample ( $S$ ) is estimated by NMR diffusion measurements or section images. The fact that  $\rho$  estimated by Godefroy et al. (2001b) on glass beads are significantly lower might be due to the intense washing of the samples with hydrogen chloride which was not conducted in this work.

#### 3.6.2. Comparison to other models

To evaluate if other models might also explain the measurements, results obtained using KGM (Eq. 3.13) are compared with results from SB (Eq. 3.11) and SDR (Eq. 3.12). The results are displayed in Figure 3.5. All equations assume a fixed  $T_B$  of 2.39 s and are calibrated using a respective material specific  $\rho$ ,  $C_{SB}$  and  $C_{SDR}$  from measurements of  $K_{\text{meas}}$ ,  $\phi$  and  $T_2$  estimated on the samples with the smallest grain sizes. The finest sample was cho-

### 3.6. Benefits and limitations of KGM

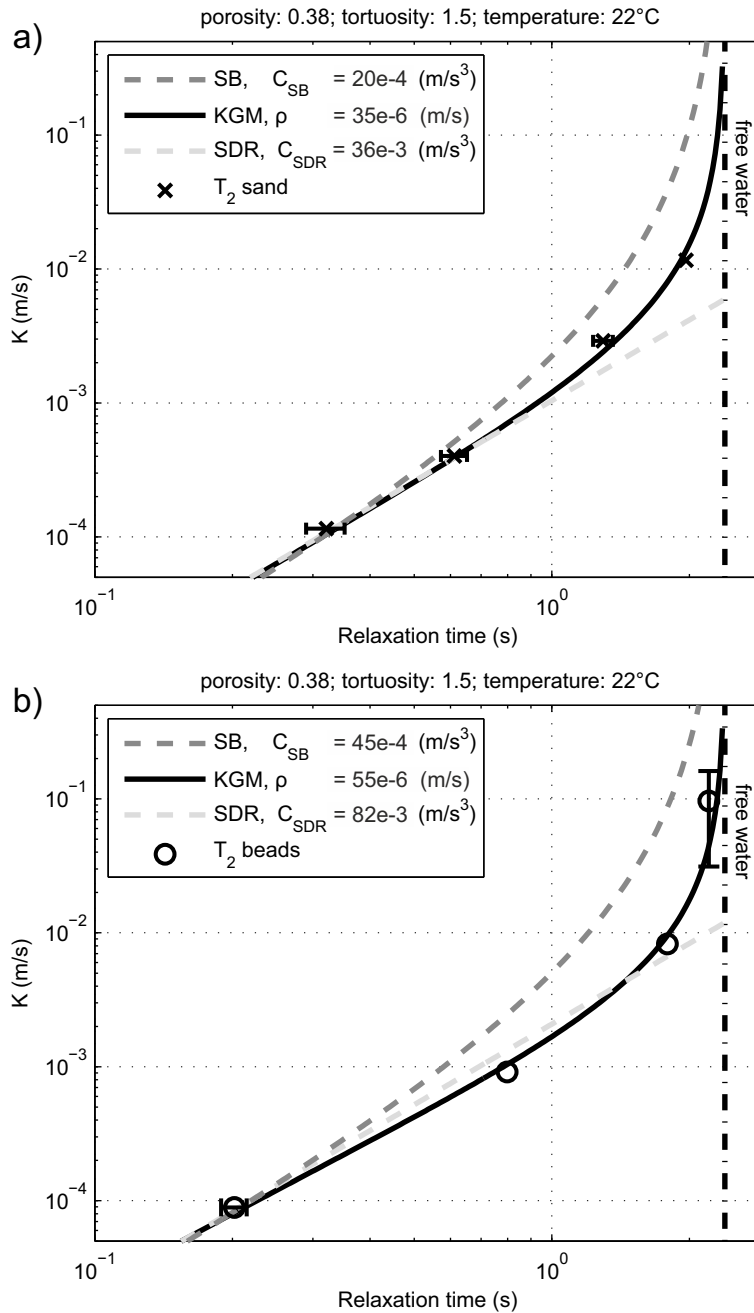


Figure 3.5.: The difference between Kozeny-Godefroy model (KGM), Seever's model including bulk water relaxation (SB) and Schlumberger-Doll Research equation (SDR) neglecting  $T_B$  when calibrated in the sand (a) or bead (b) sample with the smallest grain size. The respective estimated  $K_{meas}$  and  $T_2$  measured on samples with increasing grain sizes for comparison. Error bars smaller marker sizes are not shown.

### 3. The link between NMR and hydraulic conductivity ( $K$ )

Samples	Method to estimate $S$	$\rho/\mu\text{m s}^{-1}$		Reference
		Low.	Upp.	
Sandstones	NMR diffusion	2.6	40	Hürlimann et al. (1994)
Sandstones	section images	10	60	Kenyon et al. (1989)
Sandstones	section images	30	300	Howard et al. (1993)
Glass beads	section images	11.5		Straley et al. (1987)

Table 3.3.: References for  $\rho$  estimated from  $T_1$  and  $S$  measurements assuming fast-diffusion conditions. The method used to estimate  $S$  as well as different sample materials are listed.

sen for the calibration of the equations because it most likely fulfils the requirements where all equations are valid, i.e. negligible impact of  $T_B$  and fast-diffusion conditions. For small values of  $K$  and  $T$  the contour lines of all equations are in good agreement in shape ( $K \propto T^2$ ) and value. However, using the calibrated equations to predict  $K$  of more coarse but similar material, both SB and SDR are unable to explain the measured data. Under these conditions, two effects with opposed signs determine the relation between  $T$  and  $K$ .

One effect is due to  $T_B$ . Because  $\phi$  is fixed for this comparison,  $T_B$  is the only difference between SB and SDR. The bulk water relaxation limits the measured  $T$  and leads to an underestimation of  $K$  if ignored. The amplitude of the underestimation of  $K$  is a function of  $T$  and becomes increasingly important for high  $T$  values. Thus, a good knowledge of  $T_B$  is essential for NMR measurements on coarse material.

The second effect on the  $T$  and  $K$  relation is due to the limiting factor of  $D$  and thus the violation of the fast-diffusion approximation. It can be observed by the two facts, that (i) the measurements on the samples do not line up with SB and that they (ii) show a material specific deviation from SB and SDR. For larger pores i.e. higher  $K$ ,  $D$  limits the ability of the protons to reach the pore surface and thus to experience  $\rho$ . This leads to higher  $T$  values than expected when assuming fast-diffusion conditions. Because KGM accounts for this limiting effect of  $D$ , the measurements on samples with different grain sizes still line up on a single contour line of  $\rho$ . To quantify the grain size where the fast-diffusion approximation is no longer appropriate  $SSP$  was calculated for each presented sample using Equation 3.7. Ranges of  $\rho_a$  are obtained from KGM (see Tab. 3.2) and  $r_{\text{tube}}$  are estimated from  $K_{\text{meas}}$  using Equation 3.1 and 3.4. These values indicate that for grains sizes larger than approximately  $d_{\text{grain}} > 250 \mu\text{m}$ ,  $SSP \ll 1$

and thus the fast-diffusion approximation is violated. In consequence the application of SB and SDR is no longer valid.

Finally, the capabilities of KGM, SB and SDR to predict  $K$  using the sample specific  $\phi$  are shown in Figure 3.6. The model parameters and error ranges were estimated as described in Chapter 3.5. All equations are calibrated on the sample with the smallest grain size of each data set respectively and are used to predict  $K$  for more coarse material. Apart from the violation of the requirement for SB and SDR, using coarse material for calibration is also not recommended for KGM because of the reduced resolution of  $\rho_a$  due to  $T_B$  (see Tab. 3.2). After calibration, KGM is able to predict  $K$  from  $\phi$  and using both relaxation times,  $T_2$  and  $T_1$ , over the entire range of presented grain sizes from fine sand up to fine gravel. For the presented samples, both, SB and SDR, show systematic deviations from the hydraulic measurements for coarse material of up to one magnitude which leads to an overestimation of  $K$  using SB and an underestimation using SDR.

### 3.6.3. Limitation of the flow model

The presented KGM is developed and validated assuming fully water-saturated unconsolidated material and homogeneity at every scale. As summarised by Carrier (2003), the application of Kozeny-Carman type equations is limited to laminar flow, not too wide grain-size distribution, non-compact particle shapes and no electrochemical reactions. The latter is why clayey material is not covered.

A tube-shaped pore model sufficiently explains the presented data set of  $K$  measured on sand and glass beads using a theoretically derived  $\tau$  of 1.5 (see Fig. 3.2). However, real pores do generally not fit the assumptions of simplified pore geometries and smooth surfaces. To account for the impact of the deviation on  $K$ ,  $\tau$  can be adjusted accordingly. A change of  $\tau$  to 1.7 slightly improves the prediction of  $K$  for the presented samples from the Kozeny-Carman equation by reducing  $K_{KC}$ . This change in  $\tau$  leads to an increase of  $\rho_a$  obtained from KGM by a factor of approximately 1.3. More complex pore models may also explain the measured data. However, no analytic solutions of the governing equations are given for more complex geometries. Other analytic solutions for planar and spherical pore geometries are given in Appendix A.1.

### 3. The link between NMR and hydraulic conductivity ( $K$ )

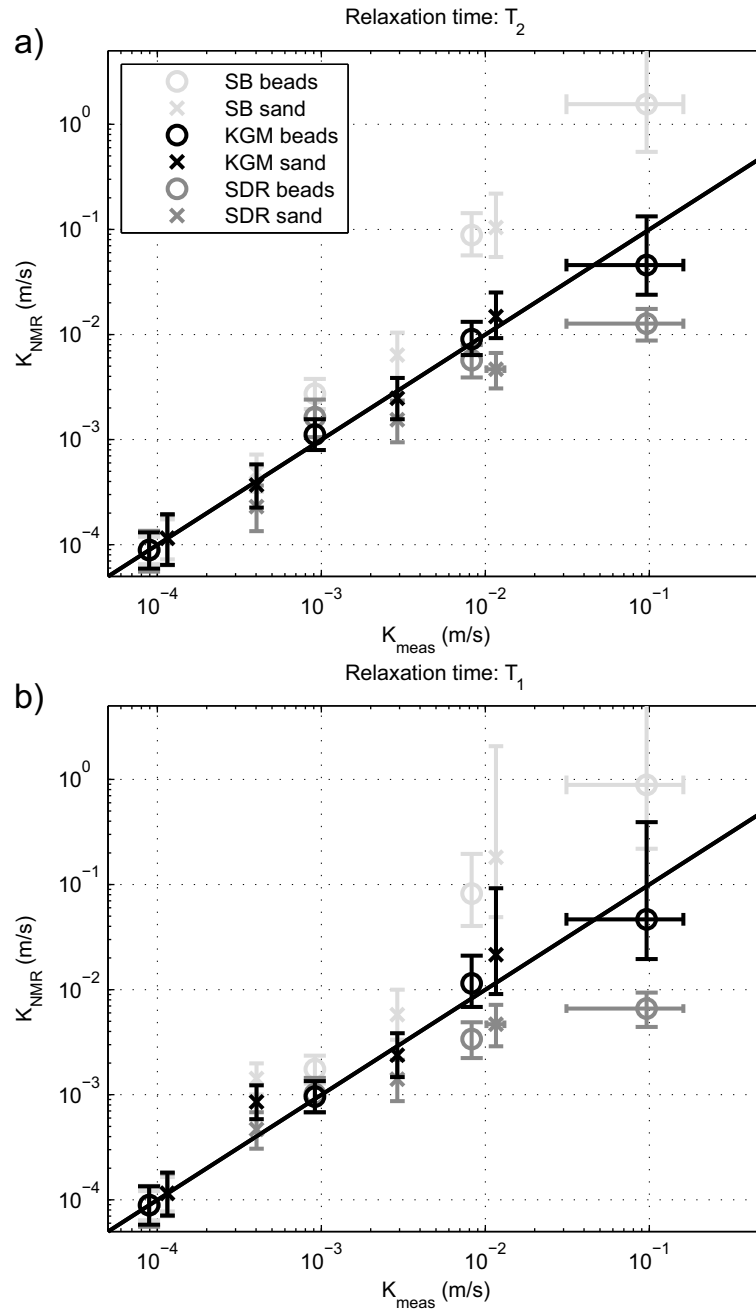


Figure 3.6.: Comparison of  $K_{\text{meas}}$  measured on quartz sand and glass bead and  $K_{\text{NMR}}$  estimated using SB, KGM and SDR for  $T_2$  (a) and  $T_1$  (b). The sample with the shortest  $T$  of each material was used for calibration. Error bars smaller marker sizes are not shown.

### 3.6.4. Limitation of the NMR model

The samples presented in this work were chosen to show a small grain-size distribution to avoid the ambiguity that multiexponential signals can either arise from different pore sizes or higher modes. Using the maximum of the  $T$  distribution allows finding an adequate measure for a sample with a single pore radius, both in the slow- and fast-diffusion case. If a material with a wide distribution of pore radii is present, using only the maximum of the  $T$  distribution will result in ignoring the effect of pores which are not represented by this maximum. Ignoring small/large pores will result in an over-/underestimation of  $T$  and thus  $K$ . A common approach in SDR handling wide distributions uses the arithmetic mean of logarithms (see Eq. 3.9) for  $T$ . Note that this is only appropriate under fast-diffusion conditions.

Additionally, one cannot exclude that multiexponential signals may also be due to other effects like inhomogeneous distribution of surface relaxivities. An assumption for the governing NMR models (Seevers, 1966; Brownstein and Tarr, 1979; Godefroy et al., 2001b) is that the relaxation of the protons at the pore surface is homogeneous for the entire sample, i.e. it can be described by a constant  $\rho_a$ . Small-scale variation of  $\rho$  within the diffusion length of a water molecule, which is  $\approx \sqrt{4DT}$  (Woessner, 1963), are averaged and the relaxation process is effectively dominated by a mean surface relaxivity (Foley et al., 1996). For the effect of a spatial distribution of  $\rho$  on NMR measurements see Grunewald and Knight (2011b). In this work,  $\rho$  is considered to be independent on  $\omega_0$  and temperature which might be an issue if measurements conducted under diverging conditions are compared. Note that the coupling of pores, i.e. the diffusion of a proton from one pore to another during the relaxation (Ramakrishnan et al., 1999), become important for material with a distribution of pore radii. Because pore coupling is not considered, this is another reason why samples with a distribution of pore radii are not covered by KGM.

## 3.7. Summary on KGM

A new model, called KGM, has been presented and evaluated for predicting  $K$  from NMR of unconsolidated material including coarse grains, but limited to a narrow pore-size distribution. KGM is in good agreement with the commonly used fast-diffusion approximations, e.g. Seevers (1966) or SDR (Kenyon et al., 1988) for fine-grained material. KGM allows for improved

### 3. The link between NMR and hydraulic conductivity ( $K$ )

prediction of  $K$  compared to SDR and SeEVERS for coarse-grained material by including slow-diffusion case and bulk water relaxation. At least for the presented samples, SDR and SeEVERS fail to predict  $K$  for grain sizes larger than medium sand and show systematic deviations of up to one magnitude.

The model replaces the empiric calibration factors by intrinsic NMR parameters (surface relaxivity, bulk water relaxation time), structural parameter (tortuosity) and physical parameters (self-diffusion constant, dynamic viscosity, density, gravitational acceleration). This improves the quality of  $K$  predicted from NMR measurements, because the calibration with flow measurements focuses on the matrix-specific parameters and therefore increases the range of validity of the calibration. The presented measurements of  $K$  and  $T$  on glass beads and quartz sands confirm KGM. Because the estimation of surface relaxivity ( $\rho$ ) from  $K$  and  $T$  using KGM does not account for surface roughness, this work refers to apparent surface relaxivity ( $\rho_a$ ) as intrinsic NMR parameter combining  $\rho$  and surface roughness. For the samples presented in this work, this leads to values of  $\approx 55(37) \mu\text{m s}^{-1}$  for glass beads and  $\approx 35(30) \mu\text{m s}^{-1}$  for sand  $T_2(T_1)$ . Extensive laboratory measurements on different geological materials may narrow the range of  $\rho_a$  and thus the range for predicted  $K$  using KGM without calibration.

The prediction of  $K$  using KGM is right now limited to (i) materials with a small range of pore sizes due to the limitation on estimating a single representative  $T$ , (ii) simple pore geometries like tube-shaped, planar or spherical pores.

# 4. Fundamentals of surface NMR

## 4.1. Basics

Surface NMR exploits the intrinsic magnetic moment (spin) of hydrogen nuclei, i.e. protons, present in the groundwater. In contrast to laboratory or borehole applications which use strong artificial magnetic background fields, surface NMR utilises the relatively low but homogeneous Earth's magnetic field. This leads to a low Larmor frequency ( $\omega_0$ ) in the range of 1 to 3 kHz, a low macroscopic net magnetisation ( $\mathbf{M}$ ) and therefore low signal strength. To increase the signal above the noise level large volumes of water need to be excited in the subsurface.

A secondary magnetic field is used to tilt the spin axis of the protons from the thermal equilibrium. For surface NMR, this secondary magnetic field is generated by an alternating current passing through a large loop laid out on the Earth's surface. The strength of the excitation is given by the pulse moment ( $q$ )

$$q = It_{\text{pulse}}, \quad (4.1)$$

defined as the product of current ( $I$ ) and excitation pulse duration ( $t_{\text{pulse}}$ ). Increasing  $q$  leads to an increasing flip angle ( $\beta$ ) for a proton at a given position ( $\mathbf{r}$ ) in the subsurface and allows the excitation of protons at greater depths.

For a given location in the subsurface, only the components of the magnetic fields perpendicular to  $\mathbf{B}_0$  interact with the spin system. They are named  $\mathbf{B}_T$  (for tx) and  $\mathbf{B}_R$  (for rx) with their respective unity vectors  $\mathbf{b}_T$  and  $\mathbf{b}_R$ . Because alternating magnetic fields in conductive media are generally elliptically polarised, the fields are decomposed into two circular rotating parts which spin clockwise  $B_{T,R}^+$  and anticlockwise  $B_{T,R}^-$  respectively relative to the spin precession. For more details see Hertrich (2008).

## 4.2. Sensitivity kernel

### 4.2.1. General 3D kernel

The characteristic of a surface NMR experiment to transmit and record NMR signals is summarised by the  $\mathbf{G}^{3d}$

$$\begin{aligned} \mathbf{G}^{3d}(q, \mathbf{r}) = & 2\omega_0 \mathbf{M}_0 \sin(-\gamma q |\mathbf{B}_T^+(\mathbf{r})|) \\ & \times |\mathbf{B}_R^-(\mathbf{r})| e^{i[\zeta_T(\mathbf{r}) + \zeta_R(\mathbf{r})]} \\ & \times [\mathbf{b}_R(\mathbf{r})\mathbf{b}_T(\mathbf{r}) + i\mathbf{b}_0\mathbf{b}_R(\mathbf{r}) \times \mathbf{b}_T(\mathbf{r})] , \end{aligned} \quad (4.2)$$

with respective phase lag relative to  $I$  ( $\zeta$ ) and unity vector of  $\mathbf{B}_0$  ( $\mathbf{b}_0$ ). If not stated otherwise, a subsurface temperature of 8°C is assumed to calculate  $\mathbf{M}_0$  for the surface NMR experiment presented in this work.  $\mathbf{G}^{3d}$  depends on direction and strength of the Earth's magnetic field, sizes, geometries and positions of the used loops, strength of the applied excitation pulse and is affected by a conductive subsurface (Weichman et al., 2000).

In this work, the propagation of the tx and the respective rx fields in the subsurface are modelled based on an analytic solution for a circular loop over a layered conductive half-space after Ward and Hohmann (1988). For details on calculating  $\mathbf{G}^{3d}$  of arbitrary loop geometries, 3D subsurface conductivity models or topography see Lehmann-Horn et al. (2011).

### 4.2.2. 2D and 1D kernel

For 2D and 1D conditions  $\mathbf{G}^{3d}$  can be integrated over the horizontal dimensions ( $x, y$ ) to the 2D sensitivity kernel ( $\mathbf{G}$ ) and the 1D sensitivity kernel ( $\mathbf{G}^{1d}$ ) respectively. Examples of  $\mathbf{G}$  for COI and HOL loop setups are presented for selected pulse moments in Figure 4.1. Because the size of  $\mathbf{G}^{1d}$  is reduced to a vector,  $\mathbf{G}^{1d}$  of several pulse moments are generally summarised in one plot as presented in Figure 4.2.

### 4.2.3. Impact of pulse moment, loop size and electrical resistivity

The penetration depth of  $\mathbf{G}^{3d}$ , and thus a surface NMR survey at a location with a given  $\mathbf{B}_0$ , depends on  $q$ , loop geometry and the electrical resistivity of the subsurface. The impact of the different parameters on  $\mathbf{G}^{3d}$  is presented for  $\mathbf{G}^{1d}$  to simplify the presentation. Generally, higher  $q$  values lead to a higher penetration depth (Fig. 4.2). The benefit of increasing  $q$  is not

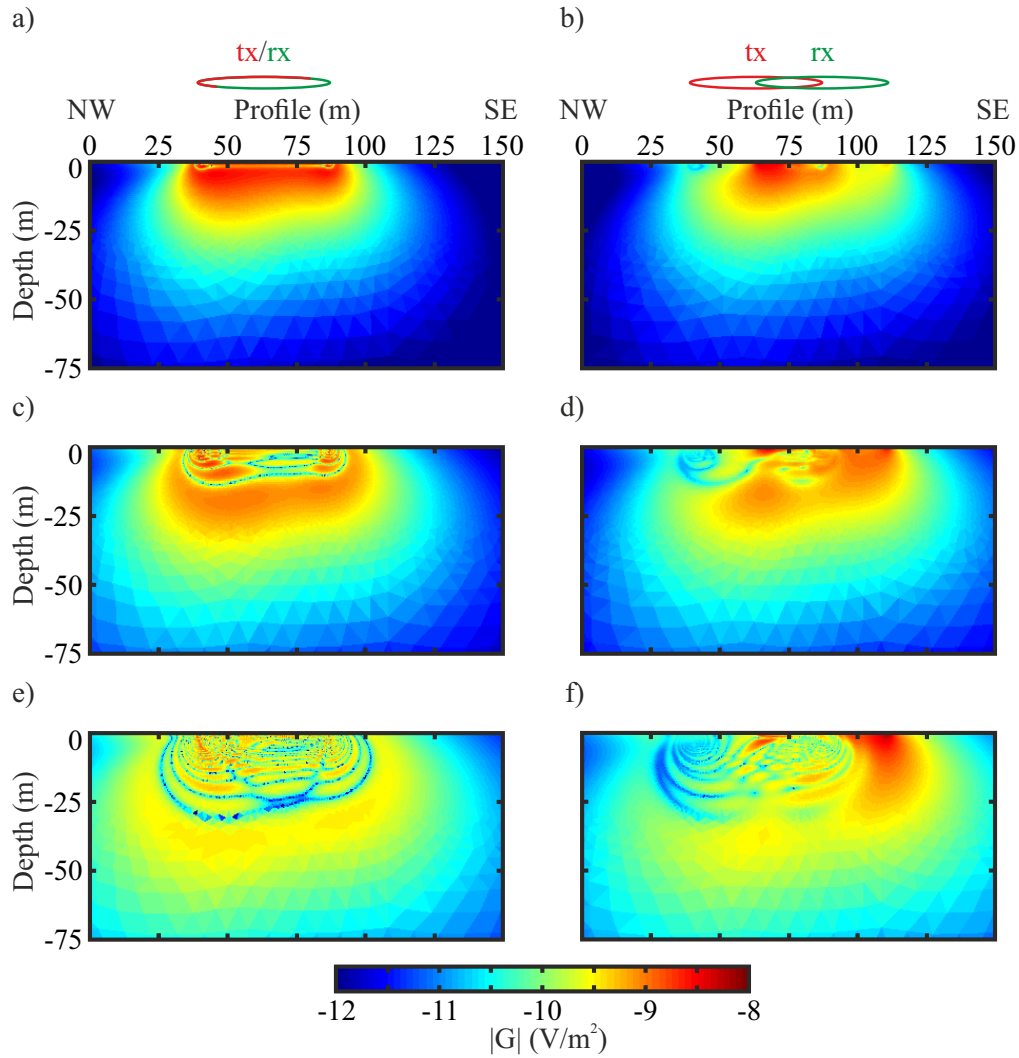


Figure 4.1.: Examples of 2D sensitivity kernel ( $\mathbf{G}$ ) for COI (a, c and e) and HOL (b, d and f) loop setups with increasing  $q$  from top to bottom [0.2, 1, 3.6] A s. Other parameters are: resistive subsurface, circular loops, 1 turn, diameter 48 m, profile direction:  $51^\circ\text{W}$ ,  $\mathbf{B}_0$  inclination:  $61^\circ$ ,  $\omega_0 = 2044$  Hz and  $\theta = 281$  K.

#### 4. Fundamentals of surface NMR

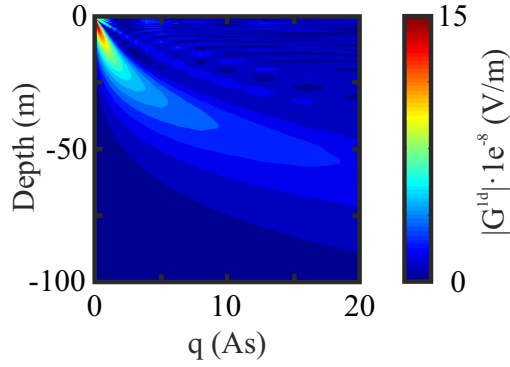


Figure 4.2.: Examples of 1D sensitivity kernel ( $\mathbf{G}^{1d}$ ) for a COI loop setup and a variation of  $q$ . Other parameters are: resistive subsurface, circular loop, 1 turn, diameter 50 m, inclination  $61^\circ$ ,  $\omega_0 = 2044$  Hz and  $\theta = 281$  K.

linear but is significantly reduced for higher  $q$  values. Recent state of the art instrumentation is limited to an  $I$  of around 600 A. Using a 40 ms pulse, this leads to a maximum  $q$  of 24 A s.

The impact of loop size and electrical resistivity on  $\mathbf{G}^{1d}$  was exemplary analysed for 1D conditions by Braun and Yaramanci (2008). Therefore, the maximum penetration depth of a surface NMR survey is additionally limited by two effects, geometrical and electromagnetic attenuation.

For an electrical resistive subsurface, the geometrical attenuation is the dominant factor. It states that at low frequencies the penetration depth of an electromagnetic field depends on its vertical homogeneity and thus the size of the tx loop (Weidelt, 2005). Therefore, an electromagnetic field emitted from a small loop has less penetration depth than a field emitted from a larger loop (Fig. 4.3 a, e, i).

For an electrical conductive subsurface, the electromagnetic attenuation increasingly affects  $\mathbf{G}^{1d}$  and reduces the penetration depth of a surface NMR layout (e.g. Fig. 4.3 i, j, l). Because  $\mathbf{G}^{1d}$  is affected by both, geometrical and electromagnetic attenuation, the depth of penetration is limited by the strongest effect. Above a certain level of electrical resistivity, the geometrical attenuation is stronger and its impact on  $\mathbf{G}^{1d}$  can be ignored. Dependent on the loop size, this level is approximately  $10 \Omega \text{ m}$  for a 10 m loop,  $100 \Omega \text{ m}$  for a 50 m loop and  $200 \Omega \text{ m}$  for a 100 m loop. For most water saturated geological materials, this limits the benefit of very large loops due to the increased impact of the electromagnetic attenuation.

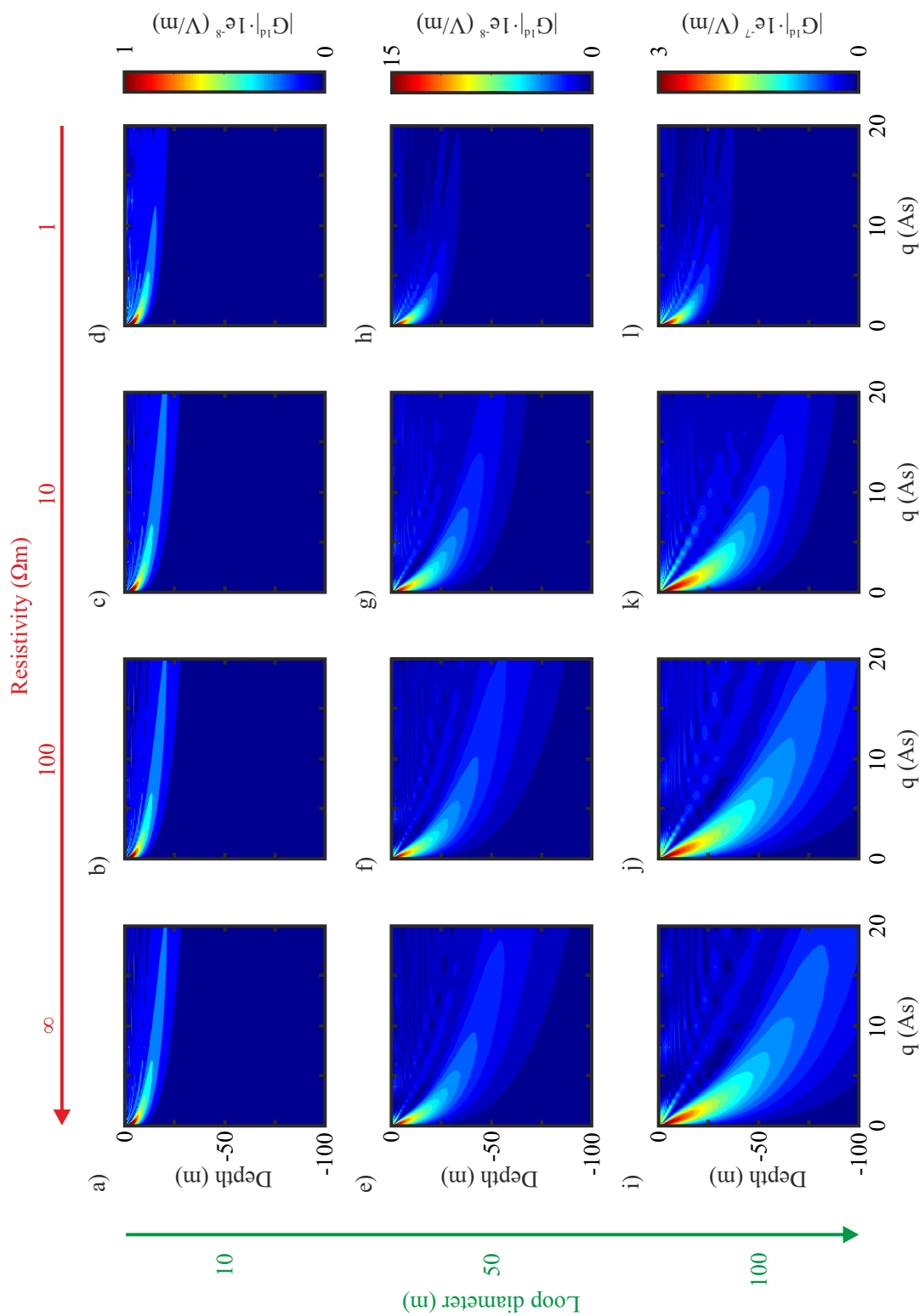


Figure 4.3.: Impact of loop size and electrical resistivity of the subsurface on the 1D sensitivity kernel ( $G^{1d}$ ). Other parameters are circular COI loop, 1 turn, inclination  $61^\circ$ ,  $\omega_0 = 2044$  Hz and  $\theta = 281$  K.

## 4.3. Forward calculation

### 4.3.1. General 3D formulation

After the excitation pulse, the protons relax back to their thermal equilibrium. Due to the precession during their relaxation they emit small magnetic fields which induce an alternating voltage in a surface loop. Quadrature detection at  $\omega_0$  is commonly used to estimate the envelope of the measured NMR signal ( $v^{\text{obs}}$ ). To simplify the notation,  $T$  is used instead of  $T_2^*$  in the following equations. Ignoring the impact of electromagnetic noise, the envelope of the synthetic NMR signal ( $v^{\text{syn}}$ ) at a time ( $t$ ) after the start of the relaxation can be described by (Mohnke and Yaramanci, 2008)

$$v^{\text{syn}}(q, t) = \int \mathbf{G}^{\text{3d}}(\mathbf{r}, q) \int w_j(\mathbf{r}, T_j) e^{-t/T_j} dT_j d\mathbf{r} . \quad (4.3)$$

The partial  $w$  ( $w_j$ ) comprises the spatial distribution of water  $\mathbf{r}(x, y, z)$  in the subsurface and for a range of specific  $T_{2j}^*$  as described by Mueller-Petke and Yaramanci (2010).

### 4.3.2. Effective dead time

Despite recent instrumental improvements, the data sets collected by surface NMR typically show a large delay between the start of the NMR relaxation and the first recorded signal. This delay is called effective dead time ( $t_{\text{deff}}$ ) (Dlugosch et al., 2011) and includes half the pulse length to account for relaxation during pulse (RDP) (Walbrecker et al., 2009), instrumental dead time and clipping of the data to avoid filter artifacts. Because of the long  $t_{\text{deff}}$ , surface NMR struggles to detect NMR signals with very short relaxation times, often associated with bound water or water in very small pores. Therefore,  $w$  detected by surface NMR is often referred to as NMR visible water or mobile water content which can lead to a significant underestimation of  $w$  in fine material.

### 4.3.3. Complex-valued signal

The signals  $v^{\text{obs}}$  and  $v^{\text{syn}}$  have generally complex values showing a phase shift  $\zeta$  between transmitted and received signal. This can be due to (i) low electrical resistivity in the subsurface (Braun et al., 2005), (ii) the use of separated tx and rx loops (Weichman et al., 2000), (iii) off-resonant excitation (Walbrecker et al., 2011) and (vi) instrumental effects. For the

inversion, the complex  $v^{\text{obs}}$  and  $v^{\text{syn}}$  are reduced to real-valued amplitudes for reasons discussed in Chapter 5.5.4.

### 4.3.4. Discrete data and model space

Generally, neither the data space nor the model space chosen for the forward calculation is continuous. The NMR signal  $v^{\text{obs}}$  is recorded at a given sampling rate which can be reduced due to the quadrature detection or filtering. This leads to a discrete  $t_n$  with  $n$  running from  $1 \dots N$ .

The model space used for the inversion is generally subdivided into layers (1D) or cells (2D) with constant  $w$  and  $T_2^*$ . In this work they are identified by a cell index ( $c$ ) running from  $1 \dots C$ . When results obtained from different inversions are compared in this work, they were generally acquired using the same mesh.

To simplify the handling of the forward problem with a computer, Equation 4.3 can be transferred into a sum notation. For 2D conditions this leads to

$$v_{t_n}^{\text{syn}} = \sum_{c_j} \mathbf{G}_{cl} w_{c_j} e^{-t_n/T_{c_j}} , \quad (4.4)$$

where the FID index ( $l$ ), running from  $1 \dots L$ , merges the spatial impact due to different  $q$  and loop positions ( $p$ ).

## 4.4. Inversion

### 4.4.1. General inversion approach

Because of the complex character of the sensitivity kernel an inversion is necessary to conclude from  $v^{\text{obs}}$  to the spatial distribution of the NMR parameters in the subsurface. This work uses the general inversion approach, i.e. objective function and solver for the normal equation, as described in detail by Hertrich et al. (2007). The to be minimised dimensionless objective function ( $\Phi$ ) consists of terms for data misfit ( $\Phi_d$ ) and model roughness ( $\Phi_m$ )

$$\Phi = \Phi_d + \lambda \Phi_m = \|\mathbf{W}_d \Delta \mathbf{d}\|_2^2 + \lambda \|\mathbf{W}_m \mathbf{m}\|_2^2 \rightarrow \min . \quad (4.5)$$

The matrix  $\mathbf{W}_d = \text{diag}(1/\epsilon)$  holds the error estimate ( $\epsilon$ ) for each data point. The vector  $\Delta \mathbf{d} = \mathbf{d}^{\text{obs}} - \mathbf{d}^{\text{syn}}$  contains the misfit between observed and forward calculated data. The first-order flatness matrix ( $\mathbf{W}_m$ ) ensures a smoothness-constrained solution (Günther et al., 2006; Hertrich et al., 2007).

#### 4. Fundamentals of surface NMR

To account for an anisotropic regularisation on 2D meshes, a weighting factor  $r_b$  for each cell boundary  $b$  is defined according to Coscia et al. (2011)

$$r_b = 1 + (r_z - 1)\mathbf{n}_b \cdot \mathbf{e}_z, \quad (4.6)$$

where  $\mathbf{n}_b$  is the normal vector on the cell boundary and  $\mathbf{e}_z$  is the unit vector in  $z$ -direction. Small values of the anisotropic factor ( $r_z$ ) lead to a decreased penalty for gradients in a vertical direction and thus predominantly layered models. The dimensionless  $\lambda$  weights between minimal data misfit and model roughness term. During an inversion, the highest  $\lambda$ , i.e. least structured model, is selected which fully explains the data. This is generally indicated by leaving no structures in the misfit and a chi-squared value ( $\chi^2 = \Phi_d/(LN)$ ) close to 1.

Applying Gauss-Newton minimisation, a model update  $\Delta \mathbf{m}^k$  is derived in each iteration  $k$  from solving the regularised normal equation

$$(\mathbf{J}^\top \mathbf{W}_d^\top \mathbf{W}_d \mathbf{J} + \lambda \mathbf{W}_m^\top \mathbf{W}_m) \Delta \mathbf{m}^k = \mathbf{J}^\top \mathbf{W}_d^\top \mathbf{W}_d \Delta \mathbf{d}^k - \lambda \mathbf{W}_m^\top \mathbf{W}_m \mathbf{m}^k, \quad (4.7)$$

using a dedicated conjugate gradient solver (Günther et al., 2006). An explicit line search procedure (Nocedal and Wright, 2006) is applied to optimise step length and thus convergence. The Jacobian matrix ( $\mathbf{J}$ ) is a function of the model parameters and needs to be recalculated for each iteration. Its derivation is described exemplarily in the Appendix A.2.

#### 4.4.2. Initial value inversion (IVI) scheme

There are several schemes available to invert surface NMR data. The initial value inversion (IVI) (Fig. 4.4 a to c) is the oldest scheme and was first presented for 1D conditions by Legchenko and Shushakov (1998). The first 2D IVI was presented by Girard et al. (2007) and Hertrich et al. (2007) using COI loop setups. By incorporating separate tx and rx loop setups Hertrich et al. (2009) increased the spatial resolution of the obtained result. A sketch of a 2D IVI incorporating COI and HOL loop setups is presented in Figure 4.5.

The initial values  $v_l^{obs}(t=0)$  necessary for IVI were estimated by fitting a complex monoexponential function to the recorded FIDs and rotating the phase shift (Fukushima and Roeder, 1981) to obtain corrected and real-valued amplitudes (Mueller-Petke and Yaramanci, 2010). The covariance for  $v_l^{obs}(t=0)$  obtained from this fit are used as an error estimate  $\epsilon_l$ . Because of the loss of information during this data reduction, IVI can only derive the

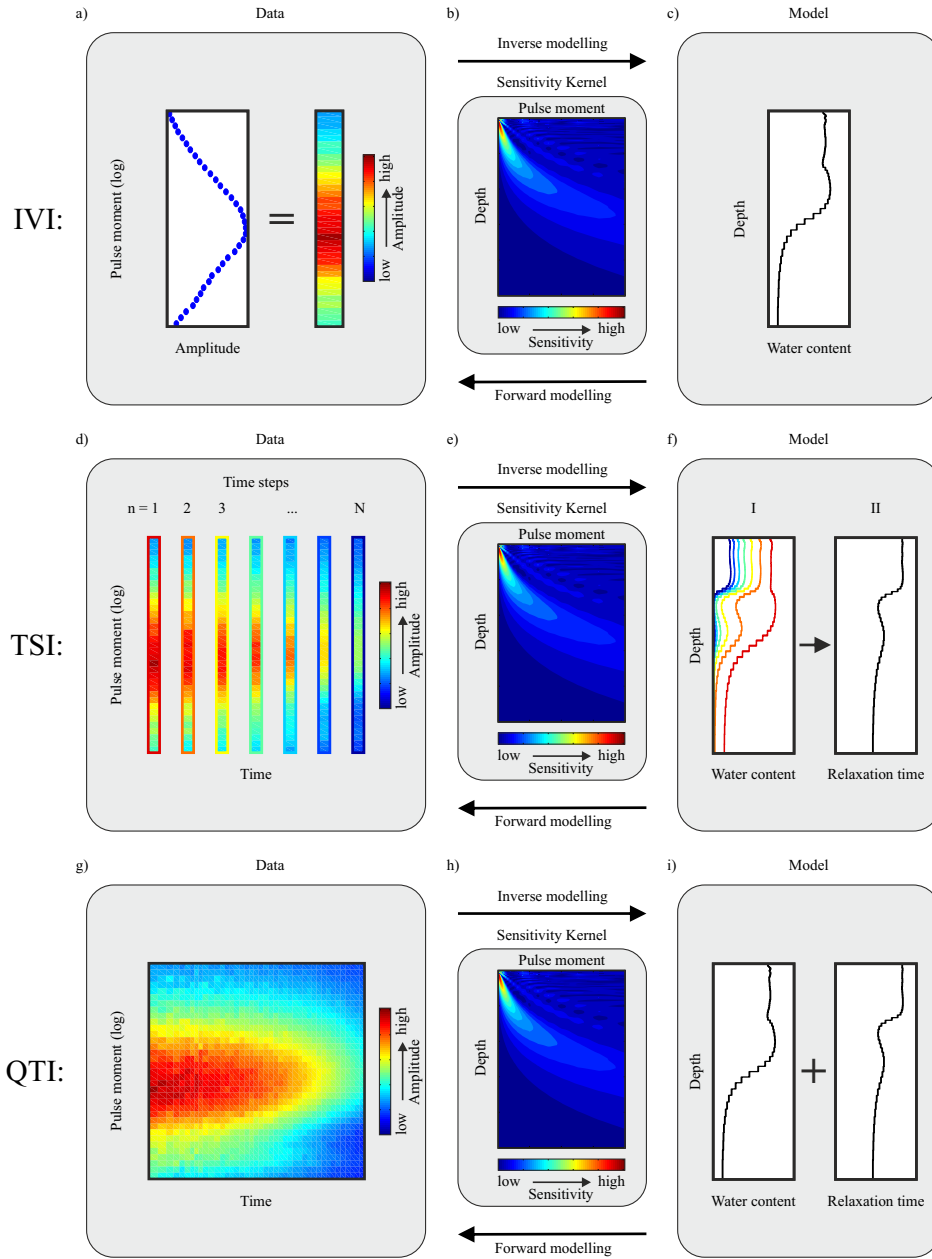


Figure 4.4.: Sketch of the 1D inversion approaches IVI (a to c), TSI (d to f) and QTI (g to i). Data domain consisting of sounding curve  $v^{\text{obs}}(q, t = 0)$  (a), sounding curves  $v^{\text{obs}}(q, t_n)$  for different time steps ( $n$ ) (d) and the entire recorded data cube  $v^{\text{obs}}(q, t)$  (g). 1D kernel function linking data and model domain for forward calculation and inversion (b, e, h). Model domain consisting of 1D distribution of  $w$  (c),  $w$  for different time steps followed by a  $T_2^*$  estimation (f), and jointly estimated  $w$  and  $T_2^*$  distribution (i).

#### 4. Fundamentals of surface NMR

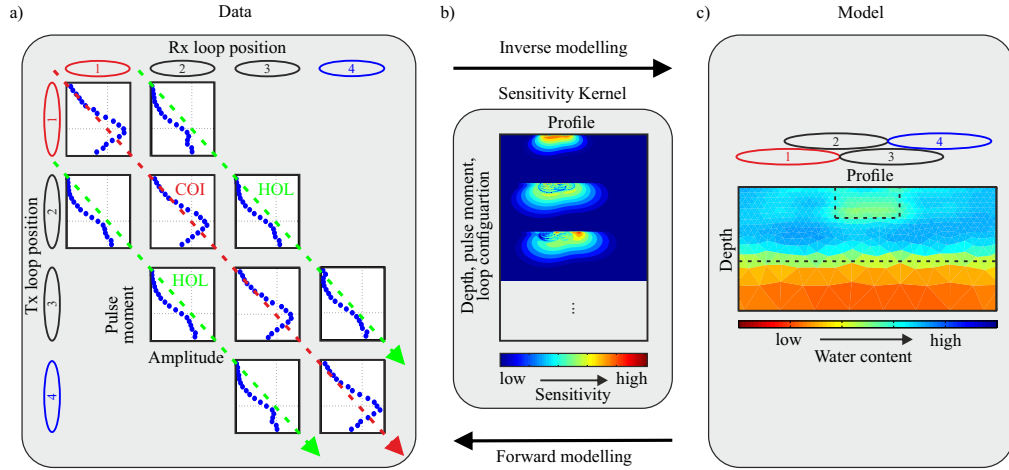


Figure 4.5.: Sketch of the 2D IVI approach. Data domain consisting of subsets of COI and HOL data sets, presented as a matrix with tx over rx loop position (a). 2D kernel function linking data and model domain for forward calculation and inversion (b). Loop positions and model domain consisting of spatial distribution of water content (c).

spatial  $w$  distribution. The respective data space ( $\mathbf{d}$ ) and model space ( $\mathbf{m}$ ) for the inversion reads

$$\mathbf{d} = [ |v_1|, |v_2|, \dots, |v_L| ]^T, \quad (4.8)$$

$$\mathbf{m} = [ w_1, w_2, \dots, w_C ]^T. \quad (4.9)$$

Under full saturated conditions, it is hardly possible to identify most unconsolidated sediments based on  $w$ . It is therefore difficult to distinguish fine from coarse-grained layers which is often essential to answer hydrological questions, e.g. for finding an optimal well location.

#### 4.4.3. Time-step inversion (TSI) scheme

The time-step inversion (TSI) approach was introduced by Legchenko and Valla (2002) to obtain information about the 1D  $T_2^*$  distribution and thus pore-size information in the subsurface (Fig. 4.4 d to f). The first 2D TSI was introduced by Walsh (2008).

TSI consists of two independent processes which are executed in series. First, several IVIs are conducted on different time steps ( $n$ ) of the FIDs to

obtain  $w$  for each cell ( $c$ ). Therefore,  $\mathbf{d}$  and  $\mathbf{m}$  for each time step read

$$\mathbf{d}_n = [|v_{1n}|, |v_{2n}|, \dots, |v_{Ln}|]^\top, \quad (4.10)$$

$$\mathbf{m}_n = [w_{1n}, w_{2n}, \dots, w_{Cn}]^\top. \quad (4.11)$$

In analogy to Günther and Müller-Petke (2012) TSI uses the standard deviation of the measured voltage  $v_{nl}^{obs}$  at each  $t_n$  for  $\epsilon_{ln}$ . In a second step, a  $T_{2c}^*$  value is estimated for each cell. Therefore, the obtained  $w_n$  values are plotted versus time step and are fitted with an monoexponential function to obtain a respective  $T_{2c}^*$  value for this cell.

Because of the two independent steps to derive the final  $T_2^*$  distribution, the obtained result lacks spatial resolution and stability (Mueller-Petke and Yaramanci, 2010).

#### 4.4.4. *qt* inversion (QTI) scheme

The inversion of 1D surface NMR data was significantly improved by the introduction of the QTI approach (Mueller-Petke and Yaramanci, 2010) (Fig. 4.4 g to i). The data space ( $\mathbf{d}$ ) of QTI consists of the full FIDs of all NMR experiments

$$\mathbf{d} = [|v_{11}|, |v_{12}|, \dots, |v_{1L}|, |v_{21}|, \dots, |v_{NL}|]^\top. \quad (4.12)$$

In analogy to TSI, QTI uses the standard deviation of the measured voltage  $v_{nl}^{obs}$  at each  $t_n$  for  $\epsilon_{ln}$  after Günther and Müller-Petke (2012).

Because QTI simultaneously obtains the spatial distribution of  $w$  and  $T_2^*$ , this increases both spatial resolution and stability of the inverse problem. The actual model space ( $\mathbf{m}$ ) used for QTI can vary. Mueller-Petke and Yaramanci (2010) presented a very general model domain using a smooth depth discretisation and allowing for a smooth multiexponential distribution of  $T_2^*$ . This leads to  $\mathbf{m}$  consisting of  $w_j$  per cell and  $T_2^*$  time window

$$\mathbf{m} = [w_{11}, w_{12}, \dots, w_{1J}, w_{21}, \dots, w_{CJ}]^\top. \quad (4.13)$$

Constraints to  $\mathbf{m}$  can help to reduce the size of the inverse problem, thus speeding up the performance, or improve the result by including additional information, e.g. a distinctive layering instead of smooth transitions. Examples are the stretched-exponential  $T_2^*$  distribution used by Behroozmand et al. (2012) or a block model with a monoexponential  $T_2^*$  distribution presented by Günther and Müller-Petke (2012). All model domains may be appropriate and may lead to improved results depending on the target and the quality of the data.



# 5. 2D distribution of $w$ and $T$ from surface NMR<sup>2</sup>

## 5.1. 2D QTI approach

### 5.1.1. Objective

The development of a 2D QTI approach is one of the main objectives of this work. A sketch of this approach is presented in Figure 5.1. The goal is to obtain 2D images of  $w$  and  $T_2^*$  of the subsurface from a surface NMR survey with increased spatial resolution and stability. The advantages of QTI, proved for 1D conditions by Mueller-Petke and Yaramanci, 2010, is expected to be transferable to 2D applications.

### 5.1.2. Optimising the size of the forward problem

According to the QTI scheme to handle the entire data set at once, the dimension of matrix  $\mathbf{G}$  is data domain size  $\times$  model domain size and can easily reach  $10^4 \times 10^5$  entries for 2D applications. This is due to the multitude of loop configurations and positions in the data domain and the added  $x$ -dimension in the model domain. As a consequence, handling  $\mathbf{G}$  with the memory of a personal computer is difficult and even the forward calculation is very slow. To reduce the size of  $\mathbf{G}$  the following steps were applied:

1. To minimise the size of the model domain it is reduced to monoexponential relaxation for each discrete location in the subsurface, as already done for 1D cases by e.g. Günther and Müller-Petke, 2012. Therefore,  $\mathbf{m}$  consists of the  $w$  and  $T_2^*$  values of all cells lined up in a single column vector

$$\mathbf{m} = [w_1, \dots, w_C, T_1, \dots, T_C]^\top . \quad (5.1)$$

---

<sup>2</sup>The main part of the content of this chapter (with the exception of Chap. 5.4) has been published in R. Dlugosch et al. (2014). Two-dimensional distribution of relaxation time and water content from surface nuclear magnetic resonance. *Near Surface Geophysics* 12 pp. 231–241. DOI: 10.3997/1873-0604.2013062

## 5. 2D distribution of $w$ and $T$ from surface NMR

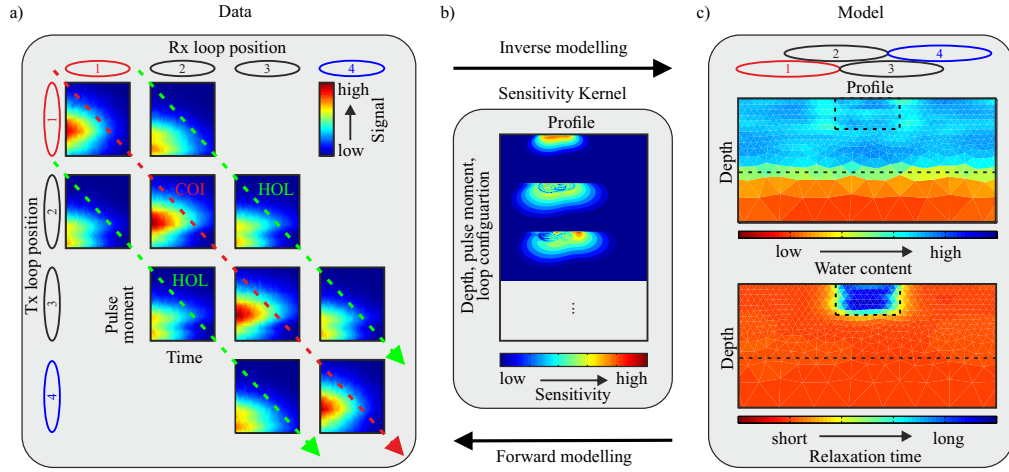


Figure 5.1.: Sketch of the 2D QTI approach. Data domain consisting of subsets of COI and HOL data sets, presented as a matrix with tx over rx loop position (a). 2D kernel function linking data and model domain for forward calculation and inversion (b). Loop positions and model domain consisting of spatial distribution of water content and relaxation time (c).

A cotangent transformation is used (see Appendix A.3) to restrict  $w$  (i.e. 0 to 0.5) and  $T_2^*$  (i.e. 0.01 to 0.8s) to reasonable values. Thus, the forward problem (Eq. 4.4) for a single FID ( $l$ ) is simplified to:

$$v_{ln}^{syn} = \sum_c \mathbf{G}_{cl} w_c e^{-t_n/T_c}, \quad (5.2)$$

The equation is now an explicit formulation of total water content  $w$  per cell and a single  $T_2^*$  instead of  $w_j$  distributed over a fixed range of  $T_2^*$  bins. The signal  $v_l^{syn}$  can still be multiexponential because it integrates over the entire subsurface.

2. An irregular triangle mesh with cell sizes growing with depth (Hertrich et al., 2007) is used during the inversion. Because of its highly oscillating characteristic close to the surface,  $\mathbf{G}$  is calculated on a finer mesh and integrated over the cells of the coarser inversion mesh.
3. The collected complex FID voltages are gate-integrated (Behroozmand et al., 2012) and reduced to a number of about  $N = 40$  time bins with associated mean times  $t_n$ . The gate and data point specific error  $\epsilon_{ln}$  is calculated according to Günther and Müller-Petke (2012) by dividing the voltage error obtained from stacking by the square root

of the number of readings within the respective gate. This leads to the gate and data point specific error  $\epsilon_{ln}$ .

Applying the described approach reduces the size of  $\mathbf{G}$  significantly. The factor is specific for each application but is in the range of 10 for both model and data domain which leads to a size of  $\mathbf{G}$  of approximately  $10^3 \times 10^4$ .

## 5.2. Synthetic study

A synthetic study is used to show the successful application of the presented 2D QTI approach and its capability to resolve structures that show only a contrast in one subsurface parameter,  $T_2^*$  or  $w$ . The setup consists of four HOL loops with a diameter of 80 m placed on a profile orientated magnetic W-E (Fig. 5.2a). The combination of HOL and COI loops was chosen to complement a high lateral resolution close to the surface with a large maximum penetration depth. The subsurface model (Fig. 5.2a and b) consists of two horizontal layers. Both have a  $T_2^*$  of 0.1 s but a changing  $w$  from 0.35 at the top to 0.1 below 60 m. A shallow structure, striking perpendicular to the profile, is 50 m wide and 25 m deep and thus significantly smaller than the loop size. This structure exhibits no contrast in  $w$  but a significantly longer  $T_2^*$  of 0.4 s.

### 5.2.1. Forward calculation

For the kernel calculation, the propagation of the magnetic field is calculated to a distance of more than four times the loop radius and scaled to 20 pulse moments spaced logarithmically between 0.01 and 15 A s. An electrical resistive Earth with a magnetic field strength of 49 300 nT and an inclination of  $68^\circ$  was assumed and  $\mathbf{G}$  was calculated on a fine mesh. For the forward calculation of the NMR signals, a coarse irregular mesh was created using `distmesh` (Persson and Strang, 2004) and  $\mathbf{G}$  was integrated over each cell. This mesh ranges two loop radii beyond the presented profile and has cell sizes of about 5 m with cell boundaries adapted to the outlines of the anomalies. The complex synthetic signal was reduced to real-valued amplitudes and Gaussian noise with a standard deviation of 35 nV was added. The obtained time series was clipped to an effective dead time of 30 ms and a maximum of 0.5 s and finally gate-integrated to  $N=39$  bins. Figure 5.2c shows the resulting  $\mathbf{d}_{syn}$  consisting of four COI soundings and six HOL setups. It also illustrates that signals from HOL loops can

## 5. 2D distribution of $w$ and $T$ from surface NMR

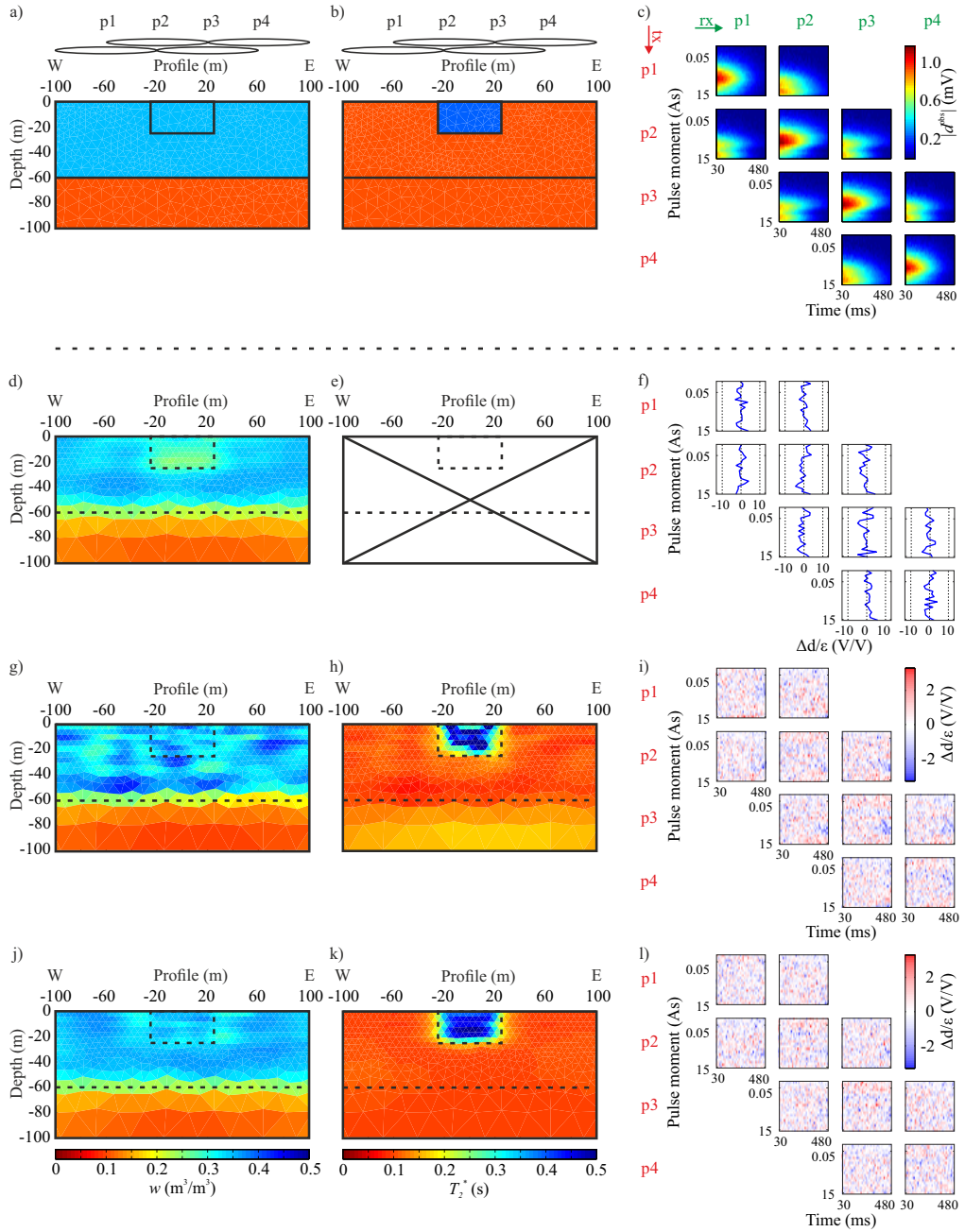


Figure 5.2.: Comparison of different 2D inversion approaches using a synthetic study. Synthetic model of  $w$  (a) and  $T_2^*$  (b) consisting of a layered subsurface and a shallow structure surveyed by four loops. (c) Synthetic data set of COI and HOL as a function of loop positions (tx over rx). 2D inversion results using the IVI (d, e), TSI (g, h) and QTI (j, k) approach. Respective error-weighted data misfit as line or image plots with  $\chi^2$  values of [4.4, 1.1, 1.0] for [f, i, l].

exhibit amplitudes comparable to COI setups, particularly for higher pulse moments.

### 5.2.2. Inversion

For the inversion, a new irregular mesh was created with cell boundaries not adapted to the outlines of the anomaly and  $\mathbf{G}$  was calculated accordingly. The cell sizes are about 5 m at the surface and coarser towards depth. This ensures a reasonable inversion speed and capability to image the demanded coarse structures. A homogeneous subsurface with  $w = 0.1$  and  $T_2^* = 0.1$  s was chosen as a starting model. The smoothness anisotropy ( $r_z = 0.2$ ) was chosen to prefer horizontal layers. The value is in the range used in ERT for sedimentary aquifer characterisation by Coscia et al. (2011). The resulting spatial distributions of  $w$  and  $T_2^*$  using the different inversion approaches are presented in Figure 5.2.

It shows that IVI can well resolve the  $w$  contrast (Fig. 5.2d) at the layer boundary at 60 m. The shallow structure, which only shows a contrast in  $T_2^*$  but not  $w$ , is traced by an area of artificially low  $w$  values. This is the result of the monoexponential fitting of multiexponential signals in the data space, which leads to an underestimation of the initial amplitudes as described by Mueller-Petke and Yaramanci (2010). The achieved  $\chi^2$  values of IVI are  $> 1$  for all  $\lambda$ . This indicates that the covariances from the FID fits are underestimating the real data error. Therefore, the  $\chi^2 \approx 1$  criterion was ignored and  $\lambda$  was chosen to achieve the smoothest model which leaves no unexplained structures in the data misfit (Fig. 5.2f).

The TSI resolves the contrast in both model parameters  $w$  (Fig. 5.2g) and  $T_2^*$  (Fig. 5.2h). However, to achieve a result which explains the data within the noise level (Fig. 5.2i), TSI tends to under-regularise the result leading to a blurry pattern. Additionally, the layer below 60 m with low  $w$  values is imaged with artificially long  $T_2^*$  times. The latter is the result of the lower boundary of the tangent transformation of the model space forcing positive  $w$  values and penalises the approximation of  $w$  to zero for all time gates. This leads to increased  $w(t)$  values for late gates which overestimates  $T_2^*$  when fitted monoexponentially.

Similar to TSI, QTI can resolve the contrast in  $w$  (Fig. 5.2j) and  $T_2^*$  (Fig. 5.2k). However, because of the native implementation of model smoothness constraining  $w$  and  $T_2^*$  simultaneously QTI avoids the erratic patterns in  $w$  and  $T_2^*$ . For both TSI and QTI,  $\lambda$  can be chosen using the  $\chi^2 \approx 1$  criterion which leaves no structure in the data misfit (Fig. 5.2l).

## 5.3. Field case 1: Eddelstorf

### 5.3.1. Site information

The presented data were acquired in 2009 at the Eddelstorf site located close to Lüneburg in Northern Germany (Figure 5.3). For coordinates of



Figure 5.3.: Location of the Eddelstorf site.

important locations see Appendix A.4. The survey is part of a data set which has already been presented in Dlugosch et al. (2011), but inverted for water content only using IVI. This work focuses on the eastern part of the profile that ranges over the buried valley. Pleistocene glacial sediments of sand and loam layers characterise the geology of the site. The result of a coinciding ERT profile is presented in Figure 5.4a including a simplified interpretation comprising information from a borehole located 200 m south of the profile. A gravel layer, tracked by a comparably resistive region ( $300 \Omega \text{ m}$ ), is present below 65 m. It is covered by a 25 m thick loam layer which shows a high electrical conductivity ( $25 \Omega \text{ m}$ ). The sand layer above ( $500 \Omega \text{ m}$ ) is approximately 30 m thick. A groundwater table is reported from a close by borehole at a seasonally changing depth within this layer but cannot be resolved by the ERT profile. The sand layer is interrupted by a 120 m wide buried glacial valley which is orientated perpendicular to the profile. The ERT profile separates the valley into a lower ( $100 \Omega \text{ m}$ ) and an upper ( $25 \Omega \text{ m}$ ) part. As reported from other glacial valleys commonly found in this area, the filling most likely consists of sand and silt interbeddings. Finally, the subsurface is covered by a 10 m thick loam layer ( $25 \Omega \text{ m}$ ).

### 5.3. Field case 1: EddeIstorf

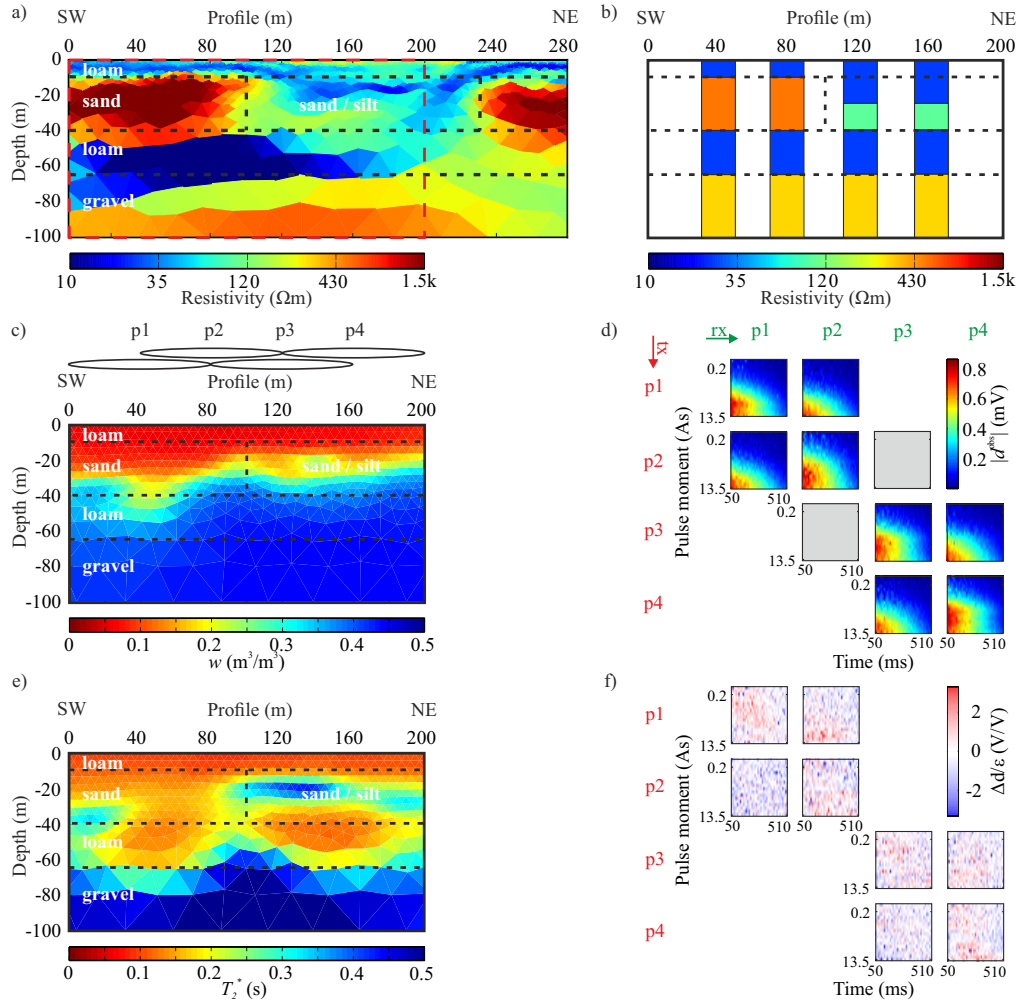


Figure 5.4.: Results of the EddeIstorf field data set. ERT profile (a), pseudo-2D model of the electrical resistivity distribution used for kernel calculation (b), loop layout and 2D QTI result for  $w$  (c) and  $T_2^*$  (e), measured data set (d) and error-weighted data misfit (f) with a  $\chi^2$  value of 1.1. Interpretation of the ERT profile including borehole information (dashed black lines) and section covered by the 2D QTI result (dashed red lines).

### 5.3.2. Surface NMR survey

On a part of the ERT profile a surface NMR survey was conducted consisting of four circular loops extending over the SW edge of the buried glacial valley. The loops have a diameter of 80 m and overlap each other by 40 m (Fig. 5.4c). The data set was collected using the GMR device from Vista Clara Inc. with pulse moments ranging from 0.1 to 13.5 A s (Fig. 5.4d). Additionally to the instrumental dead time of 10 ms and half the pulse length of  $t_{\text{pulse}}/2 = 20$  ms the first 20 ms of the low-pass filtered (500 Hz) data were removed because of artifacts. These artifacts are probably the result of instrumental effects occurring in the early version of the GMR which were reduced later by cycling the phases of the transmitter pulses allowing for a significantly shorter effective dead time of the stacked signal (Walsh et al., 2011). All delays sum up to a  $t_{\text{dteff}} = 50$  ms for the data after processing.

### 5.3.3. Inverse modelling

The ERT profile from the Eddelstorf site (Fig. 5.4a) shows large regions of high electrical conductivities which have a significant impact on the electromagnetic field propagation. Because the approach after Ward and Hohmann (1988) used in this work to calculate magnetic fields can only handle 1D conditions for the electrical resistivity distribution, a pseudo-2D scheme has to be applied as an approximation. Therefore, the kernel calculation was split into loop setups lying mainly inside and outside of the buried valley and use respective 1D electrical resistivity models as approximations (Fig. 5.4b). Two HOL configurations with one loop on either side of the edge of the buried valley were therefore excluded from the data set (Fig. 5.4d). If not otherwise stated,  $r_z$  was set to 0.2 during the inversion. As a starting model a homogeneous subsurface with  $w = 0.1$  and  $T_2^* = 0.1$  s was chosen.

### 5.3.4. 2D QTI result

The spatial distribution of  $w$  and  $T_2^*$  obtained by 2D QTI is presented in Figure 5.4c and e, respectively. The error-weighted data misfit (Fig. 5.4f) shows that the inversion result explains the data within the noise level. The buried valley, located NE of profile metre 90, is traced by a rise in the NMR-visible water table from about 30 to 18 m. The top loam and the upper part of the sand layer exhibit only little detectable water with

$T_2^* < 0.2$  s. This is likely due to partial saturation but can also be the result of the long effective dead time of the NMR data set preventing the detection of fast relaxing signals from water in small pores. The part of the expected buried valley shows a pattern of low  $w$  values but still long  $T_2^*$  up to 0.4 s. Below 30 m,  $w$  rises to 0.4 and does not trace any layering. In contrast, the  $T_2^*$  distribution enables to distinguish the loam layer with  $T_2^* \approx 0.15$  s from the underlying gravel layer with  $T_2^* > 0.4$  s. The depth of this transition is in good agreement to borehole information and is supported by the ERT survey.

### 5.3.5. Results of other 2D inversion approaches

The impact of different inversion approaches on the obtained spatial distribution of  $w$  and  $T_2^*$  is presented in Figure 5.5. The result of QTI, already presented in Figure 5.4c and e, is plotted for comparison (Fig. 5.5g and h).

The  $w$  distribution obtained from IVI (Fig. 5.5a) agrees well with the QTI result. It traces the buried valley by a rise in the NMR-visible water table but cannot distinguish the loam from the gravel layer below 40 m. In analogy to the synthetic study, the  $\chi^2$  value is significantly higher than 1 indicating that the used  $\epsilon_l$  underestimates the real data error.

The spatial distribution of  $w$  obtained from TSI (Fig. 5.5d) agrees well with the IVI and QTI results. The  $T_2^*$  image (Fig. 5.5e) can, to some degree, resolve the boundary between the gravel and the loam layer at 65 m. However, due to the lack of spatial regularisation the  $T_2^*$  image appears blurry. In contrast to QTI, TSI cannot resolve the buried valley by a specific  $T_2^*$ . Additionally, the top loam and the upper part of the sand layer with very low  $w$  values show very long  $T_2^*$  times. This is in analogy to the synthetic study and can be the result of the lower boundary of the cotangent transformation of  $w$  during the inversion. The remaining structures in the data misfit (Fig. 5.5f) show that the presented TSI result cannot fully explain the measured data. Reducing  $\lambda$  improves the data misfit only slightly but leads to very erratic images of  $w$  and  $T_2^*$ .

### 5.3.6. Impact of regularisation anisotropy

The impact of changes in the anisotropic factor ( $r_z$ ) on the QTI result is shown in Figure 5.6. The parameter  $\lambda$  was adopted respectively to reach  $\chi^2 \approx 1$ , i.e. all presented results equivalently explain the measured data within the error level. Therefore, a  $r_z$  value of 1 leads to round anomalies in the model while smaller values prefer a horizontal layering.

## 5. 2D distribution of $w$ and $T$ from surface NMR

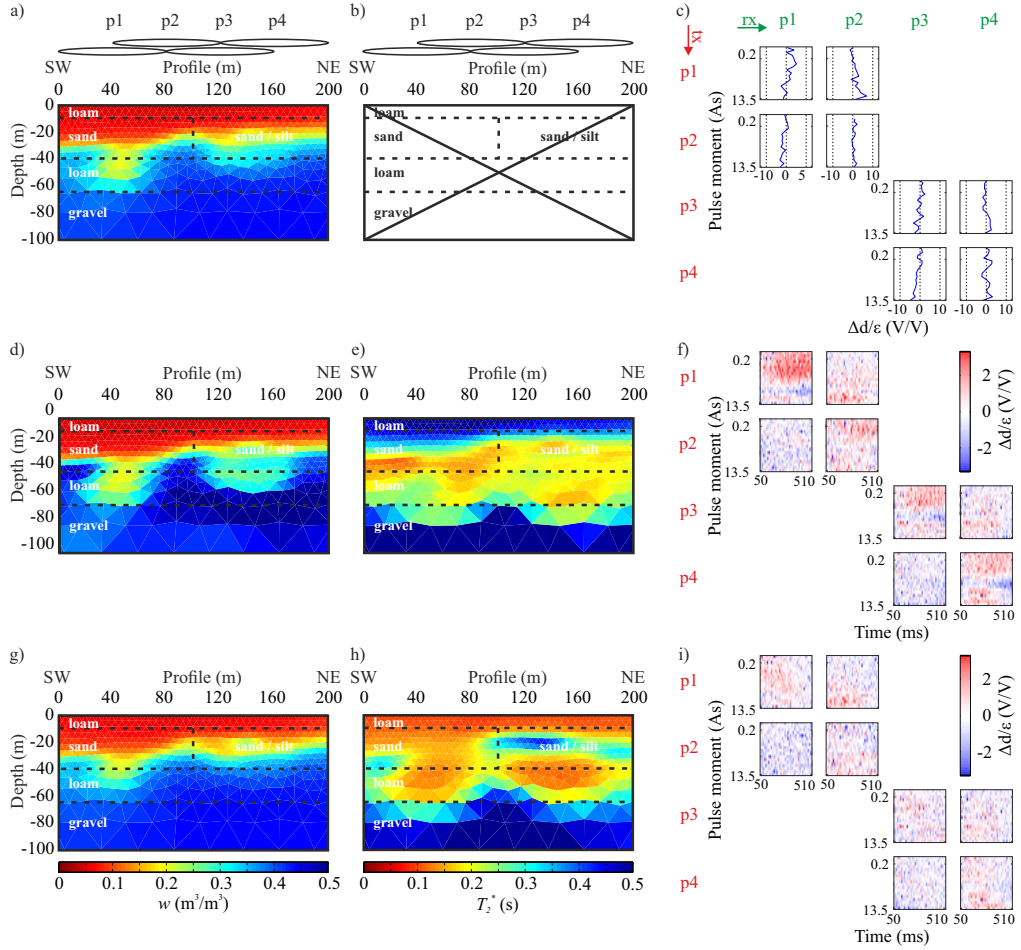


Figure 5.5.: Comparison of different 2D inversion approaches on the Eddelstorf site. Results of  $w$  (a, d, g) and  $T_2^*$  (e, h) using IVI (a, c), TSI (d, e, f) and QTI (g, h, i). All inversions use a pseudo-2D model for the electrical resistivity distribution and  $r_z = 0.2$ . Respective error-weighted data misfit as line or image plots with  $\chi^2$  values of [3.5, 1.6, 1.1] for [c, f, i].

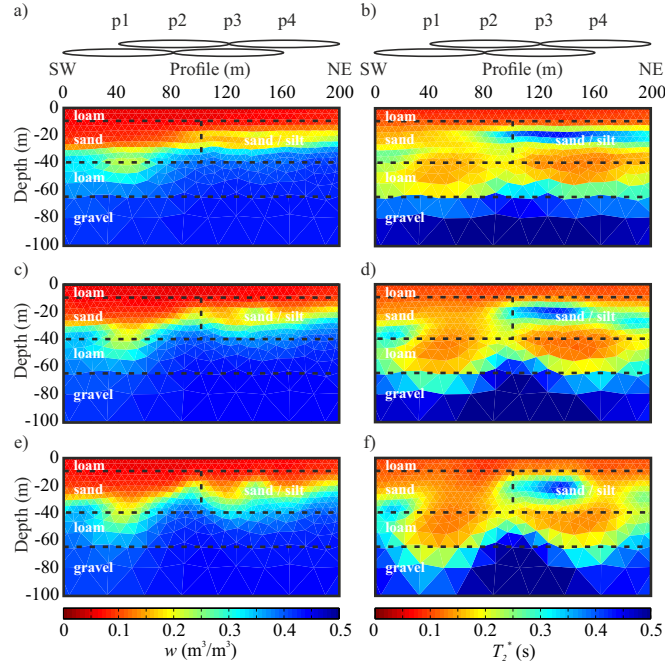


Figure 5.6.: Impact of regularisation anisotropy on the QTI. Images of  $w$  (a, c, e) and  $T_2^*$  (b, d, f) for different values of  $r_z$  [0.03, 0.2, 1] for [(a, b), (c, d), (e, f)]. All inversions use a pseudo-2D model for the electrical resistivity distribution and achieve  $\chi^2$  values of [1.17, 1.14, 1.16].

Because all results explain the data equally well, an assumption or additional information, e.g. from a borehole or other geophysical data, are required to decide which  $r_z$  to chose. A  $r_z$  of 0.2, which is in the range chosen by Coscia et al. (2011), seems to be a reasonable balance to trace the structures present at the profile, especially for  $T_2^*$ .

### 5.3.7. Impact of electrical resistivity

The impact of the electrical subsurface resistivity on surface NMR is comprised in the magnetic field calculation and thus the kernel  $\mathbf{G}$ . This impact is independent of the inversion approach, but essential for a successful application of surface NMR (Braun and Yaramanci, 2008). Figure 5.7 shows how three simple 1D electrical resistivity models affect the 2D QTI result. The electrical resistivity models were chosen to approximate the real distribution of subsurface resistivities in three steps.

## 5. 2D distribution of $w$ and $T$ from surface NMR

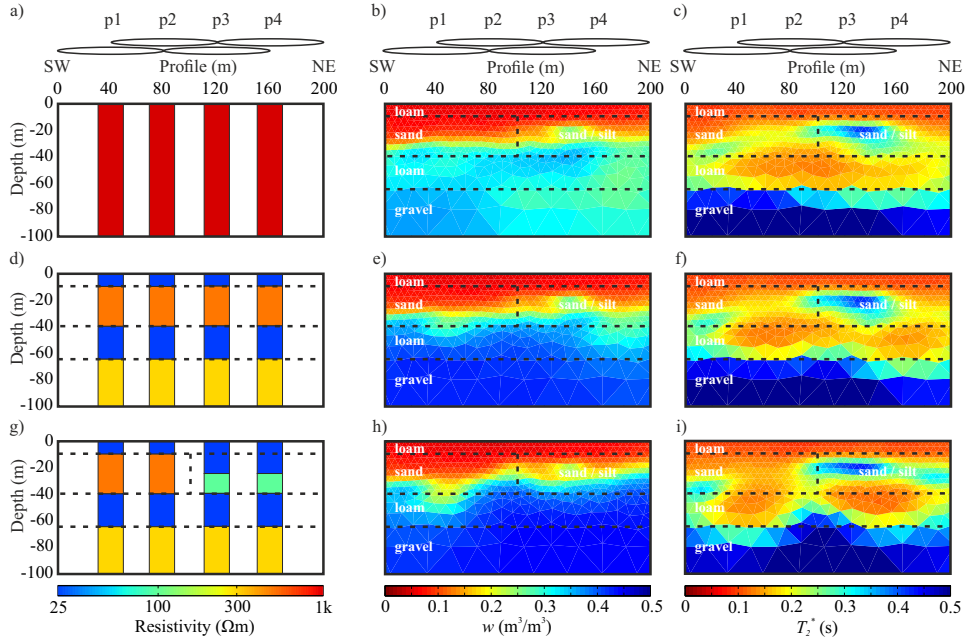


Figure 5.7.: Impact of different electrical resistivity models used for the kernel calculation on the 2D QTI result of  $w$  (b, e and h) and  $T_2^*$  (c, f and i) for the EddeIstorf site. Selected electrical resistivity models consisting of resistive half-space (a), 1D background resistivity (d) and pseudo-2D model (g). All inversions use  $r_z = 0.2$  and achieve a  $\chi^2$  value of 1.1.

As already shown for 1D by Braun and Yaramanci (2008), ignoring that the true electrical subsurface resistivities are low (Fig. 5.4a) and assuming a electrical resistive half-space (Fig. 5.7a) leads to (i) a correlation of low  $w$  values with regions of low electrical resistivity and (ii) a shift of subsurface structures to greater depth. Both effects are visible in  $w$  (Fig. 5.7b) and  $T_2^*$  (Fig. 5.7c), e.g. at the loam layer between 40 and 60 m.

Using a 1D model according to the electrical resistivity distribution outside of the buried valley (Fig. 5.7d) (i) increases the overall  $w$  values and (ii) removes the correlations of  $w$  with regions of low electrical resistivity outside the buried valley (Fig. 5.7e). Inside the buried valley, a small area with lower  $w$  values persists. The boundary between the loam and gravel, still clearly visible in the  $T_2^*$  image (Fig. 5.7f), is slightly raised.

Finally the electrical resistivity model has been adapted to the pseudo-2D scheme (Fig. 5.7g) additionally accounting for the lower electrical resistivities inside the buried valley. This (i) removes the area of lower  $w$  values (Fig. 5.7h), (ii) further rises the loam-gravel interface below the buried

valley (Fig. 5.7i) and (iii) enhances imaging the sand/silt layer at the NE end of the valley due to  $T_2^*$ . Because of the imperfect implementation of the electrical subsurface resistivity using a pseudo-2D scheme, the raise of the loam-gravel boundary below the buried valley seems to be slightly higher than expected and the lower loam layer appears interrupted at the edge of the valley. A structural joint inversion of electrical resistivity and surface NMR data can help to reduce the ambiguities of both methods (Günther and Müller-Petke, 2012). While different electrical resistivity models lead to a relocation of  $w$  and  $w$  anomalies, the  $T_2^*$  values seem to be more robust than the  $w$  values.

## 5.4. Field case 2: Nauen

### 5.4.1. Site information

The Nauen site is located west of Berlin, Germany (Fig. 5.8). For coordinates of important locations see Appendix A.4. The subsurface is



Figure 5.8.: Location of the Nauen site.

characterised by glacial sediments with a lateral change in the shallow lithology. Several geophysical methods were used to survey this site including laboratory measurements on samples from a close-by borehole, ERT, ground-penetrating radar (GPR), 1D surface NMR (Yaramanci et al., 2002) and a 2D surface NMR with separated loops (Hertrich et al., 2009). Selected results and a conceptual 2D model of the subsurface are presented in Figure 5.9.

5. 2D distribution of  $w$  and  $T$  from surface NMR

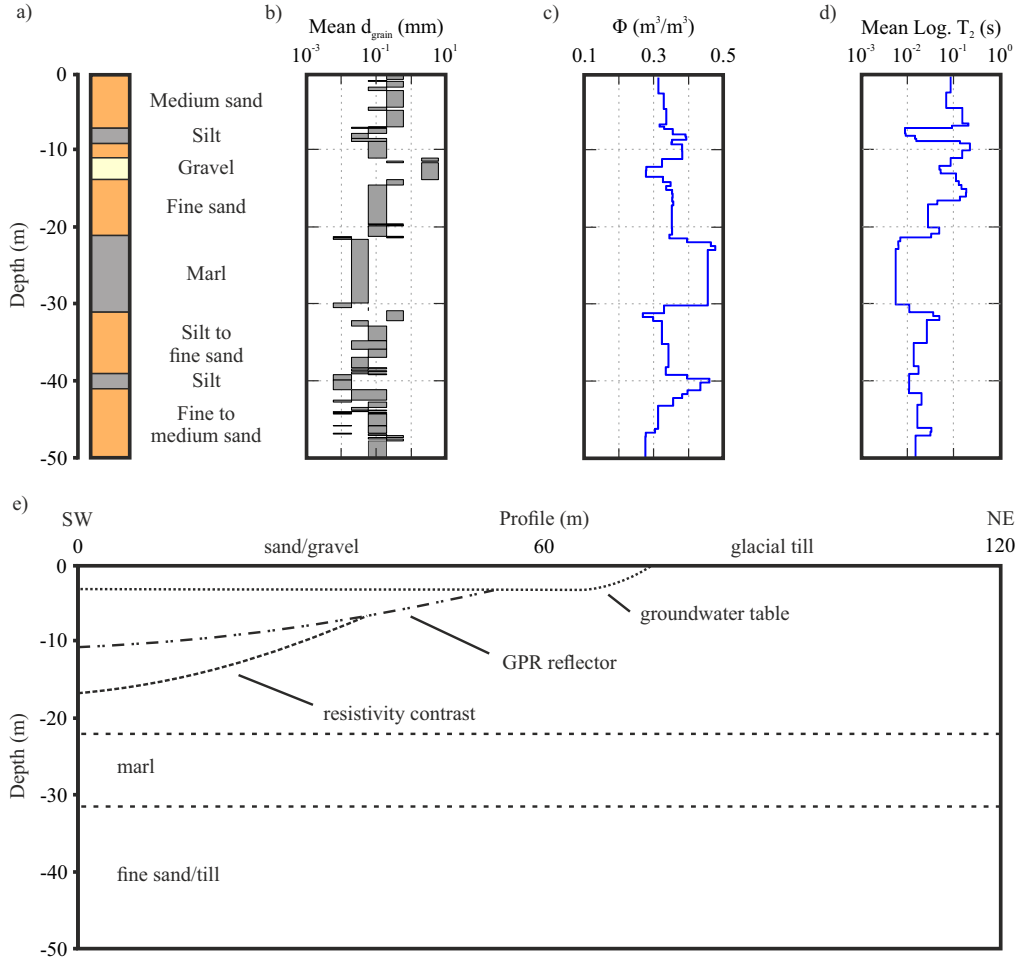


Figure 5.9.: Summary of subsurface parameters on the Nauen site. 1D lithology model (a) based on  $d_{\text{grain}}$  from sieving (b), and  $\phi$  (c) and mean of logarithms of  $T_2$  (d) (Eq. 3.9) from laboratory NMR estimated on samples from a borehole 150 m SW of the profile after Müller-Petke (2009). Conceptual 2D model (e) of the subsurface based on borehole, ERT and GPR measurements modified after Hertrich et al. (2009).

Below 30 m, the subsurface is characterised by a highly structured aquifer partly with thicker layers of fine sand or till material. Measurements on samples from a close by borehole show  $\phi \approx 0.35$  and  $T_2$  of some tens of millisecond. These  $T_2$  values are noticeable shorter than  $T_2$  measured on samples with similar grain sizes from the more shallow part ( $< 22$  m) of this site. Müller-Petke (2009) interpreted this as the result of the long storage of the drill cores leading to dry samples which were re-saturated for the NMR measurements. Minerals dissolved in the pore fluid and generally present in a higher concentration at greater depth precipitate and accumulate at the pore surface. This can lead to an increase in  $\rho$ , e.g. for iron (Keating and Knight, 2007), or to an increase in the apparent surface relaxivity ( $\rho_a > \rho$ ) due to an increased roughness of the pore surface (Kenyon, 1997).

On top of the lower aquifer and ranging from 22 to 30 m lies a marl aquiclude. Laboratory measurements show  $T_2 < 10$  ms and high  $w$  of  $\approx 0.45$ . The geology on top of the aquiclude changes laterally from the SW to the NE part of the profile. This lithological change is visible in the ERT section as a change in electrical resistivity from  $300 \Omega \text{ m}$  (SW) to  $100 \Omega \text{ m}$  (NE) and as a rise of a GPR reflector (Fig. 5.9e). The NE of the profile is not covered by borehole information but samples taken from the surface indicate that this part consists of glacial till. In the SW of the profile a geological structure cuts into the till layer. A borehole 150 m SW of the profile and penetrating this lithology exhibits fine to medium sand and gravel. NMR measurements characterise this lithology with a mean  $T_2$  of 80 to 100 ms and a  $\phi$  of 0.35. The unsaturated zone above 2 m correlates well with a highly electrical resistive layer ( $> 1000 \Omega \text{ m}$ ) in the ERT section and the groundwater table at the site is clearly visible as a GPR reflector. Both methods are not able to detect the groundwater table NE of profile metre 75 where the finer material of the glacial till leads to a larger capillary fringe instead of a sharp discontinuity in  $w$  necessary for GPR to map a reflector and the high clay content diminishes the impact of  $w$  on the electrical resistivity.

#### 5.4.2. Surface NMR survey

To show the benefit of separated tx and rx loops for surface NMR, a survey consisting of four circular loops extending over a change in the shallow lithology was carried out in 2004 and published by Hertrich et al. (2009). The loops have an diameter of 48 m and overlap each other by 24 m (Fig. 5.5b). A data set consisting of COI, HOL and E2E loop setups with tx (2 turns) and rx (1 turn) and pulse moments ranging from 0.1

## 5. 2D distribution of $w$ and $T$ from surface NMR

to 9.1 A s with  $t_{\text{pulse}} = 40$  ms was collected using the NUMIS device from Iris Instruments. Because of the instrumental dead time of 40 ms for the already internally estimated envelope of the NMR signal, this leads to an effective dead time (Dlugosch et al., 2011) of the processed data set of 60 ms including RDP. Further survey parameters are  $\mathbf{B}_0 = 49\,068$  nT, a  $\mathbf{B}_0$  inclination of  $68^\circ$  and a profile azimuth of  $51^\circ\text{E}$ . In analogy to Hertrich et al. (2009), a mean electrical subsurface resistivity of  $100\ \Omega\text{m}$  was assumed for all inversions presented for this site. Parts of the subsurface deviate from this mean value to higher resistivities, e.g. in the vadose zone or the coarse aquifer in the SW. However, because Braun (2007) showed that for the used loop size a electrical subsurface resistivity  $> 100\ \Omega\text{m}$  does not have a significant impact on the propagation of the magnetic excitation fields and thus the inversion result, these parts were ignored when calculating  $\mathbf{G}$ .

### 5.4.3. Results using different 2D inversion approaches

First, the data misfit of the different inversion approaches are compared which indicate the quality of the achieved results. As presented in Figure 5.10 (c, f, i), all inversion approaches can explain the measure data without leaving major features in the data misfit. The achieved  $\chi^2$  value of IVI is close to 1 and therefore significantly lower than  $\chi^2$  achieved for the Eddelstorf data set. This indicates that the covariance obtained from the monoexponential FID fit can lead to an appropriate error estimate when the recorded FIDs are adequately monoexponential, e.g. the  $T_2^*$  range in the subsurface is small. In contrast to the Eddelstorf data set, the  $\chi^2$  values obtained by TSI and QTI are significantly larger 1. This indicates that the used stacking error of the FIDs underestimates the real data error for the presented data set. Further studies need to evaluate if this is specific for the already internally processed FIDs of the NUMIS equipment. Thus for TSI and QTI,  $\lambda$  was chosen to achieve the smoothest model which leaves no unexplained structures in the data misfit (Fig. 5.10 f and i).

The impact of different inversion approaches on the obtained spatial distribution of  $w$  is presented in Figure 5.10 (a, d, g). Generally, the results of all inversion approaches agree well. They all trace the groundwater table at 2 m as observed in the SW part of the profile by ERT and GPR measurements. However, in contrast to ERT and GPR, surface NMR can detect the groundwater table beyond the change in lithology NE of profile metre 75. The change in lithology in the top 22 m from SW to NE is not traced by the  $w$  distribution. All inversion approaches can identify the marl aquiclude between 22 to 30 m depth. The layer is characterised by surface

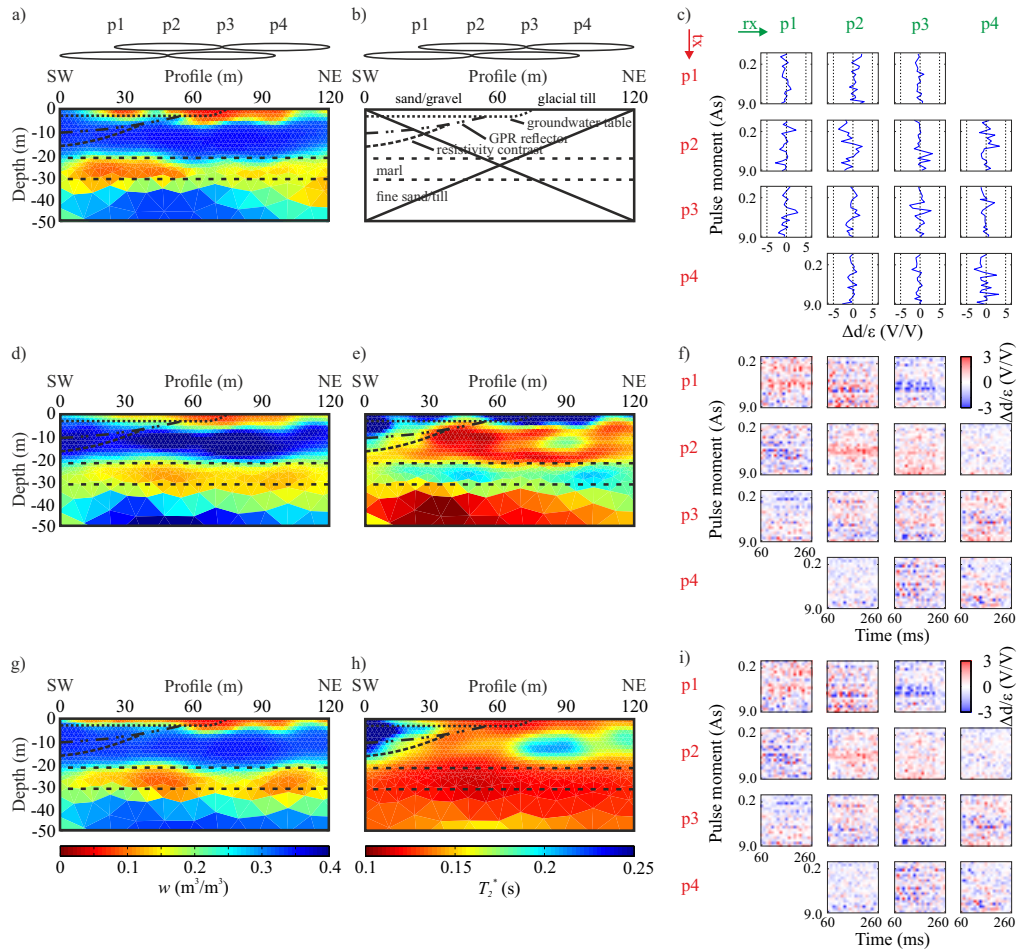


Figure 5.10.: Comparison of different 2D inversion approaches on the Nauen site. Results of  $w$  (a, d, g) and  $T_2^*$  (e, h) using IVI (a, c), TSI (d, e, f) and QTI (g, h, i). (b) Conceptual model of the subsurface based on borehole, ERT and GPR measurements modified after Hertrich et al. (2009). All inversions assume  $r_z = 0.2$ . Respective error-weighted data misfit as line or image plots with  $\chi^2$  values of [1.3, 1.6, 1.6] for [c, f, i].

## 5. 2D distribution of $w$ and $T$ from surface NMR

NMR with low  $w$  of  $\approx 0.15$  in contrast to the surrounding aquifers with  $w > 0.3$ . Compared to TSI and QTI, IVI struggles to resolve the lower boundary of the aquiclude in the NE part of the profile.

In contrast to  $w$ , the lateral change in lithology is clearly visible in the spatial  $T_2^*$  distribution with consistent long  $T_2^* > 0.25$  s in the SW and a pattern of  $T_2^*$  between 0.1 and 0.2 s in the NE. The location of the transition is in good agreement to the ERT and GPR results. The deeper aquifer below 30 m depth shows  $T_2^*$  between 0.1 and 0.15 s. The major differences between the results obtained using TSI and QTI are located in low  $w$  layers, i.e. unsaturated zone  $< 2$  m and marl aquiclude between 22 to 30 m. In these layer,  $T_2^*$  obtained from TSI is shifted to longer  $T_2^*$  than expected from laboratory NMR (Fig. 5.9) or typical for the lithology. These artifacts were also observed in the TSI results obtained from the synthetic study (Chap. 5.2.2) and the Eddelstorf field case (Chap. 5.3.5). They are the result of the lower boundary of the tangent transformation of  $w$  used for the TSI which leads to too high  $w$  for late time gates and, as a consequence, affect the fitted  $T_2^*$  times.

### 5.4.4. Comparison to the former 2D inversion result

The presented Nauen data set has already been published by Hertrich et al. (2009) using an IVI to obtain the spatial distribution of  $w$  (Fig. 5.11a). In analogy to Hertrich et al. (2009), the impact of RDP is ignored for the QTI result presented in Figures 5.11c and d. While the  $w$  values obtained using QTI are slightly higher than the IVI result by Hertrich et al. (2009), the spatial distribution of  $w$  is similar. The increased spatial resolution of QTI allows to resolve the boundary between the aquiclude and the underlying aquifer at 30 m in the NE part of the profile in the obtained  $w$  values indicating a horizontal layering below 22 m at the site. Additionally, the spatial distribution of  $T_2^*$  obtained by QTI enables to clearly identify the change in shallow lithology from coarse to fine material.

Figures 5.11e and f show the QTI result including RDP, as already presented in Figure 5.10. As expected, accounting for RDP leads to higher  $w$  values dependent on the respective  $T_2^*$  of the cell. For the presented example, this (i) removes the pattern of low  $w$  values at regions with short  $T_2^*$  times, which for example trace the change in the shallow lithology between profile metre 30 to 40 and (ii) slightly increase the contrast in the estimated  $T_2^*$  times.

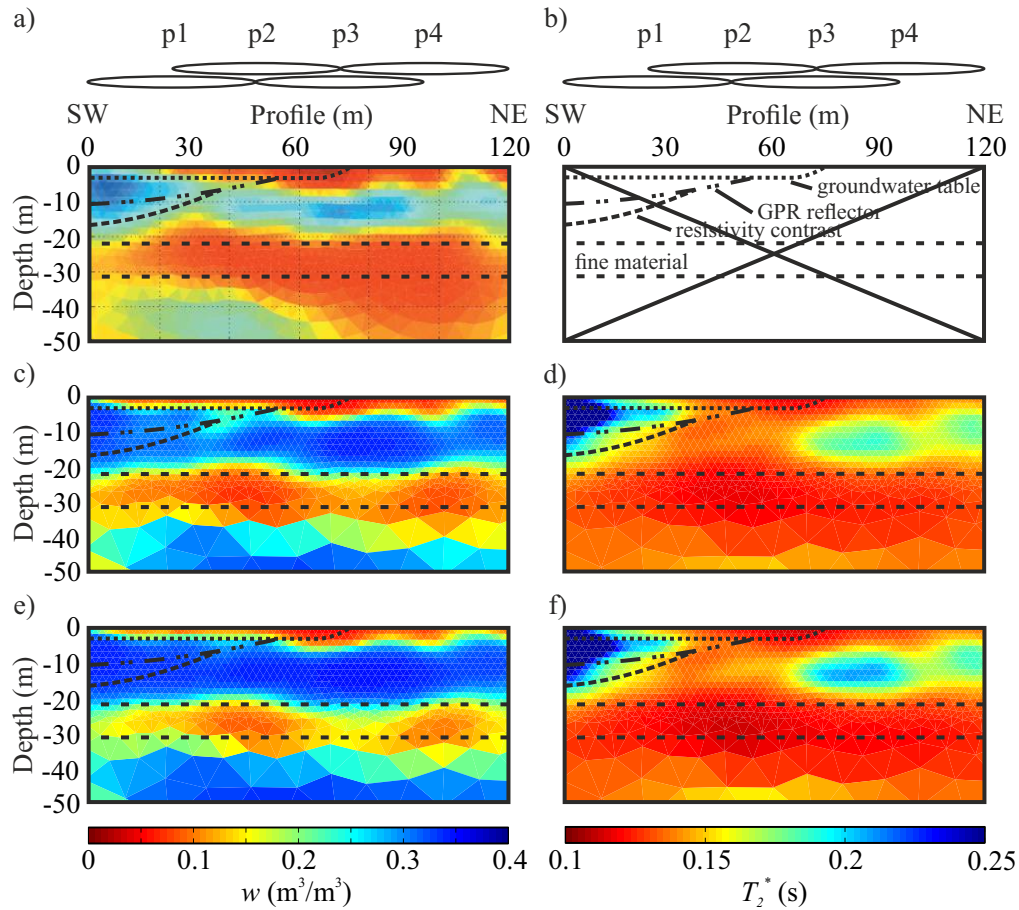


Figure 5.11.: Comparison of results for  $w$  (a, c, e) and  $T_2^*$  (d, f) using IVI from Hertrich et al. (2009) (a) and QTI (c to f) on the Nauen site. The results (a) to (d) do not account for RDP. The result accounting for RDP (e) to (f) in analogy to Figure 5.10 for comparison. (b) Conceptual model of the subsurface based on borehole, ERT and GPR measurements modified after Hertrich et al. (2009).

## 5. 2D distribution of $w$ and $T$ from surface NMR

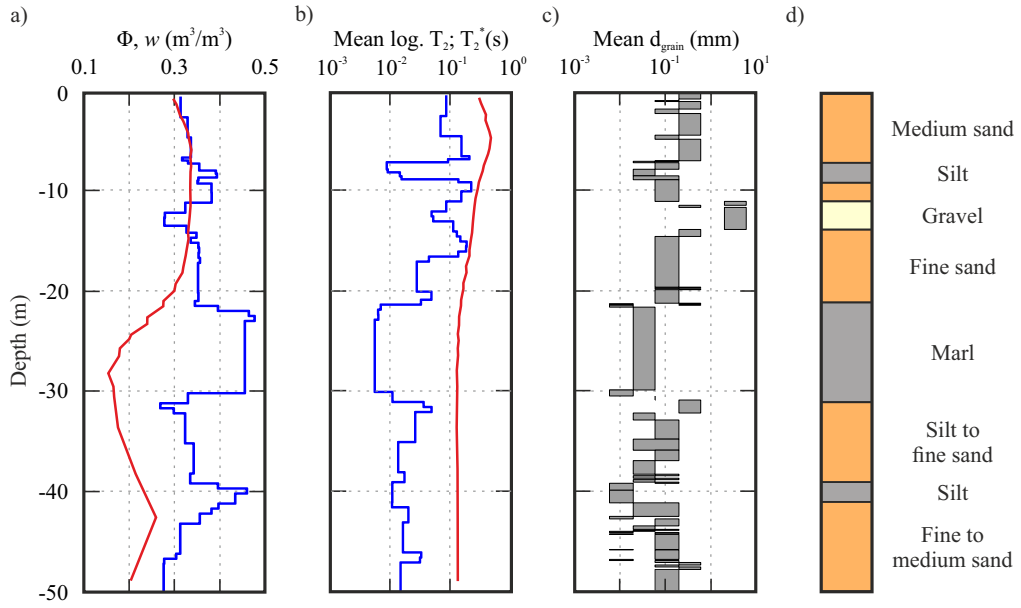


Figure 5.12.: Results of  $\phi$  (a) and mean of the logarithms of the  $T_2$  distribution (b) obtained using laboratory NMR measurements (blue) on samples from a borehole located close to the Nauen site (after Müller-Petke (2009) and presented in Fig. 5.9). The results for  $w$  (a) and  $T_2^*$  (b) extracted from the 2D QTI result (Fig. 5.10) at profile metre zero obtained from surface NMR (red). Mean grain size (c) estimated on the same borehole samples and conceptual 1D lithology model (d) of the borehole for comparison.

### 5.4.5. Comparison to laboratory results

A comparison of the laboratory results on samples from the close-by borehole (Müller-Petke, 2009) and a vertical section through the 2D QTI result at profile metre zero is presented in Figure 5.12. Because the laboratory samples had to be re-saturated from dried up conditions, the NMR amplitude is given as porosity ( $\phi$ ) instead of water content ( $w$ ). Both parameter should yield identical information below the groundwater table located at about 2 m depth. The upper aquifer above 22 m shows consistent results of  $\approx 0.35$  for  $\phi$  and  $w$  (see also Fig. 5.10). In the aquifer below 30 m,  $w$  estimated by surface NMR is only about 0.2 to 0.25 and thus significant lower than  $\phi$  obtained from laboratory NMR. The largest deviation can be observed in the marl aquiclude between 22 to 30 m depth, which is traced with high  $\phi$  values up to 0.45 by laboratory NMR but very low  $w$  values  $< 0.2$  by surface NMR. The deviations in  $w$  and  $\phi$  observed by both

methods are most likely the result of the long effective dead time (60 ms) of the surface NMR data set which yields no information about water with fast relaxation times.

A comparison of the estimated relaxation times, the monoexponential  $T_2^*$  from surface NMR and the  $T_{ML}$  (Eq. 3.9) of the  $T_2$  distributions obtained by laboratory NMR, is more complex. Both measures are affected by the different (i)  $t_{\text{dteff}}$  of both data sets, (ii) behaviour to multiexponential signals and (iii) dephasing of the NMR signal and thus difference between  $T_2$  and  $T_2^*$ . Therefore, it is expected that both measures quantitatively differ but agree qualitatively. A more detailed discussion on this topic can be found in Chapter 6.4.4. The shallow aquifer is characterised by the longest relaxation times observed by both NMR methods on the depth profile. The values are  $T_2^* > 0.25$  s and  $T_2$  between 0.08 to 0.2 s both with a slight trend to lower relaxation times with depth. The second aquifer below 30 m is hardly resolved by surface NMR as indicated by the low  $w$  values. The achieved  $T_2^*$  of around 0.1 s is close to the expected lowest resolvable limit of  $T$  for the given  $t_{\text{dteff}}$  of 60 ms. Because of the short  $T_2$  times estimated by laboratory NMR it is quite surprising that surface NMR can detect any amount of water in this layer. Together with the grain-size information, this supports the assumption of Müller-Petke (2009) that the  $T_2$  times estimated on the re-saturated laboratory samples might be shifted to shorter  $T_2$  times than representative for in-situ conditions. In the fine aquiclude between 22 to 30 m,  $T_2$  drops below 0.01 s which can no longer be resolved by surface NMR as indicated by the very low  $w$  values. The  $T_2^*$  times estimated by the QTI from the surface NMR measurements seem to persist at the  $T_2^*$  values of the adjacent layers which is likely due to the smoothness constraints in the model domain.

## 5.5. Discussion on 2D QTI

### 5.5.1. Benefit of the NMR relaxation time

Both, TSI and QTI allow to obtain a spatial information about the  $T_2^*$  distribution in the subsurface.  $T_2^*$  can yield valuable information about lithology, pore size and  $K$  if not dominated by additional relaxation processes, e.g. dephasing in high susceptibility material or a short  $T_B$  of the pore fluid.

Limitations and flaws in the conduction and interpretation of NMR measurements, like (i) using a monoexponential data fit on multiexponential

## 5. 2D distribution of $w$ and $T$ from surface NMR

signals during IVI (Chap. 5.2), (ii) ignoring RDP (Chap. 5.4.4), (iii) a long  $t_{\text{deff}}$  (Chap. 5.4.5 or more detailed Chap. 6.4.4) and (iv) using an incorrect electrical resistivity model for the kernel calculation (Chap. 5.3.7), lead to artifacts in the estimated  $w$  distribution which are often dependent on  $T$ . Because  $w$  is expected to vary only slightly for most geological material under saturated conditions, efforts to overcome these limitations can reduce the structural information visible in  $w$ . This increases the value of  $T$  to obtain spatial and lithological information of the subsurface.

### 5.5.2. Advantages of the 2D QTI

A comparison between IVI, TSI and QTI has been treated in detail by Mueller-Petke and Yaramanci (2010) for 1D conditions. They concluded that the available information content of surface NMR measurements is extracted with increased spatial resolution and stability because the complete data set is taken into account jointly. For the 2D application the used concepts do not change and the presented synthetic (Chap. 5.2) and field examples (Chap. 5.3.5 and 5.4.3) support this conclusion. Although further adaptations to the presented IVI and TSI approaches might improve the inversion results, e.g. to avoid the artificial long  $T$  in low  $w$  regions of the TSI approach, the presented QTI solves these problems naturally. The approach jointly inverts for  $w$  and  $T_2^*$  and allows to implement the data error, both enabling an appropriate model regularisation and the use of the  $\chi^2 = 1$  criterion. An adequate data error can be estimated from the stacking error of the FIDs obtained from high frequency sampled and conservatively filtered NMR records. Only in the case of an almost monoexponential  $T$  distribution in the subsurface the misfit of a monoexponential data fit seems to be a viable alternative. The described features of QTI lead to a simplified inversion and improved results compared to TSI.

### 5.5.3. Monoexponential model space

For the presented examples, the model space was decreased to a monoexponential relaxation for each model cell to minimise the size of the inverse problem for QTI. There are three arguments that support this simplification. (i) Surface NMR data sets commonly have a long effective dead time and low signal-to-noise ratio. Both makes the detection of very fast relaxing signals difficult (Dlugosch et al., 2011). This can remove the necessity to account for clay-bound water in the model which is a major source for clearly multiexponential NMR signals in unconsolidated material, e.g. when

using laboratory NMR. (ii) Pores in unconsolidated material are likely not isolated (James and Ehrlich, 1999). If a sample consists of connected pores with different diameters within the diffusion length of a proton during its relaxation,  $\approx \sqrt{4DT}$  (Woessner, 1963), NMR only identifies a mean  $S/V$  of the pores (Ramakrishnan et al., 1999) and therefore a narrow distribution of relaxation times. Finally, (iii) the monoexponential assumption is the simplest model which sufficiently explains the presented data.

#### 5.5.4. Complex signal

After quadrature detection, the envelope  $v^{\text{obs}}$  of the recorded NMR signal is complex. Mueller-Petke and Yaramanci (2010) discussed the use of real-valued amplitudes ( $|v^{\text{obs}}|$ ) or corrected amplitudes obtained by rotating  $v^{\text{obs}}$  for the inversion. However, following their conclusion of rotating  $v^{\text{obs}}$  leads to artifacts when rotating clearly multiexponential surface NMR signals. Because some of the recorded NMR signals presented in this work are clearly multiexponential the use of amplitudes was preferred during the inversion to avoid these artifacts. The main drawback of using amplitudes is the increased noise level at late record times leading to artificially long  $T_2^*$ . By gate-integrating and clipping  $v^{\text{obs}}$  to  $t < 0.5$  s these artifacts are reduced. However, the full exploitation of the complex  $v^{\text{obs}}$  during the inversion is highly recommended when instrumental phases are sufficiently studied in the future. This potentially reduces model ambiguities and improves depth resolution (Weichman et al., 2002; Braun et al., 2005).



# 6. The hydrogeophysical test site Schillerslage

## 6.1. Objectives

The main objective of this chapter is to apply the 2D QTI approach and KGM to a well known hydrogeophysical test site to evaluate their results. The structural information obtained from the 2D QTI result is compared to borehole information and an ERT result. Surveys of several other NMR methods were conducted to evaluate the  $w$  and  $T_2^*$  values obtained from surface NMR. This comparison additionally provides a unique insight into the specific potentials of different NMR methods to characterise shallow aquifers. Subsequently, the application of KGM is transferred from the laboratory to the field scale. Finally, combining the 2D QTI result and KGM allows to obtain a 2D image of the  $K$  distribution in the subsurface.

## 6.2. Overview

### 6.2.1. Location

The Schillerslage site is located northeast of Hannover, Germany (Fig. 6.1). The area has been used to test geophysical equipment since decades. The site was selected because of the geological conditions typical for northern Germany, its good accessibility and the low electromagnetic noise-level.

In 2009, the Leibniz Institute for Applied Geophysics (LIAG) developed the location to a hydrogeophysical test site with observation wells and several drillings down to the bedrock. The boreholes were drilled using a hollow drill auger provided by the State Authority for Mining, Energy and Geology. The equipment allows to gain drill cores and to install plastic casings for subsequent borehole measurements.

The area is covered by a wide range of geophysical surveys including transient electromagnetics, spectral induced polarisation, GPR, seismoelectrics and seismics as described in Holland et al., 2011. This work is focused on a W-E profile where three drillings (Eng03, Eng08 and Eng20), one ERT profile, a 2D NMR survey from location p1 to p7 and a 1D NMR

## 6. The hydrogeophysical test site Schillerslage



Figure 6.1.: Location of the Schillerslage site.

sounding at p1 were conducted (Fig. 6.2). For coordinates of the locations see Appendix A.4.

### 6.2.2. Geology

The geology is characterised by sediments of the glacial periods Elsterian, Saalian and Weichselian lying on top of a marl bedrock from the Late Cretaceous (Binot, 2008). The sediments primarily consist of medium sand with layers of fine sand, gravel and boulder clay and were dated considering the regional context (Fig. 6.3a). Because the observed stratification is almost horizontal, the results of the three lithological profiles obtained at Eng20, Eng08 and Eng03 are summarised in a conceptual 1D model of the subsurface (Fig. 6.3b and c). For the studied W-E profile, the deviation of this 1D model from most geological interfaces observed in the boreholes is less than 1 m. Only the interfaces which delimit the Elsterian sediments show deviations up to 2 m as indicated in Figure 6.3a. Because of the good depth information obtained from borehole logs, the 1D model favours the information obtained at Eng20 which locate the upper limit of the Elsterian sediments at around 10 to 11 m.

The top 5 m of the subsurface consist of medium sand from the Weichselian glacial with an interbedded 0.15 m thick peat layer at a depth of about 1.5 m. Although not present in the lithology profile, a separate drilling at Eng20 using a soil sampler confirms the presence of this peat layer at about 1.8 m. The mean water table at the Schillerslage site is

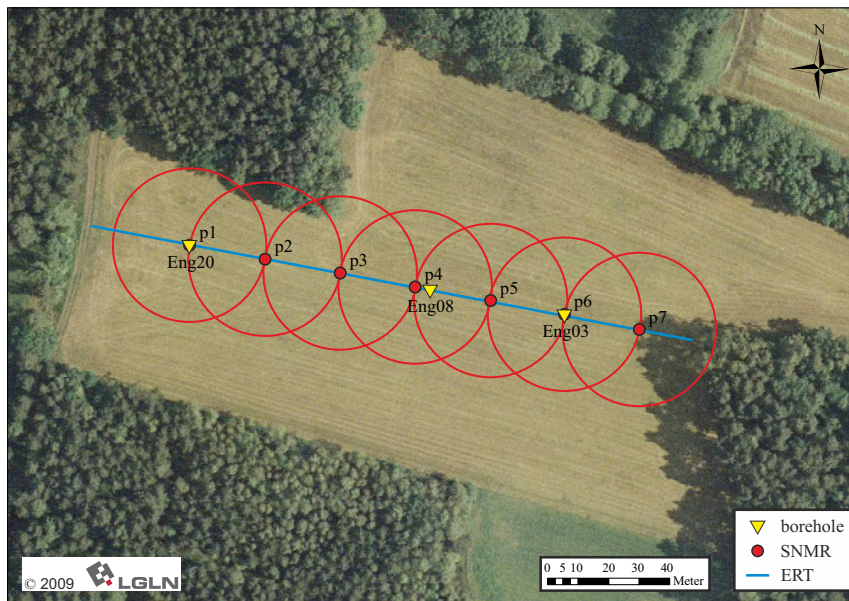
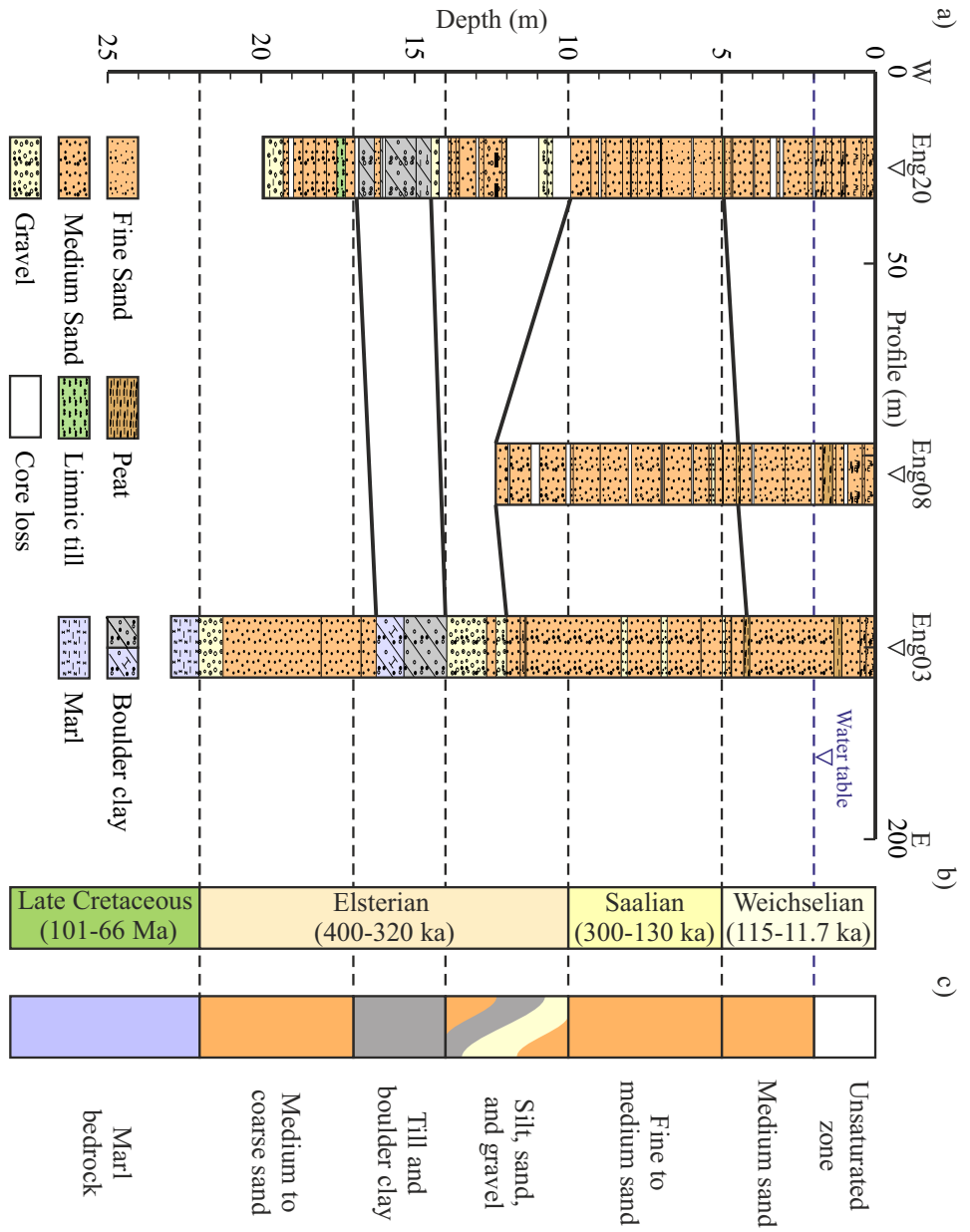


Figure 6.2.: Overview of the drill locations (Eng03, Eng08 and Eng20), loop positions of surface NMR survey (p1 to p7) and ERT profile conducted at the Schillerslage site.

located at about 2 m depth with annual variations of approximately  $\pm 0.5$  m. A thin peat layer from the Eemian interglacial separates the sediments of the Weichselian glacial from an about 5 to 7 m thick layer of well sorted fine to medium sand from the Drenthe stadium of the Saalian complex. Below about 10 m, the sediments of the Elsterian glacial form three layers. These sediments are generally not well sorted, contain a significant amount of silt and show high lateral variations in lithology and thickness. On the observed profile, the top of this layer down to 14 m is characterised by medium sand with layers of silt and gravel. Below, an approximately 3 m thick and solid boulder clay layer separates the water saturated sediments of the area into two aquifers. Further drillings in the surrounding of the main W-E profile show that the thickness of the boulder clay varies widely on a regional scale (Binot, 2008). It can reach up to 7 m, thereby replacing the sand and gravel layer of the Elsterian glacial on top, but can also disappear and therefore is not consistently separating the two aquifers. Below the boulder clay, a layer of medium to coarse sand reaches down to the marl bedrock at about 22 m.

6. The hydrogeophysical test site Schillerslage

Figure 6.3.: (a) Lithology profiles of the Schillerslage site from geological analyses of the drill cores Eng03 (Binot, 2008), Eng08 and Eng20 (Binot, pers. comm.). Derived conceptual 1D model of the site consisting of age (b) and lithology (c).



### 6.2.3. Drill location Eng20

The drilling location Eng20 was chosen for a detailed and comprehensive survey of the two shallow aquifers at the Schillerslage site using NMR. To be able to evaluate and interpret the results, several other geoscientific methods were conducted to gather a more complementary image of the location (Fig. 6.4). The information consists of a lithology profile obtained from drill cores (Fig. 6.4a) and grain-size analyses performed on sub-samples of the cores (Fig. 6.4b). Additionally,  $K_{KC}$  was calculated from the grain-size information using Equation 3.5, assuming  $\tau = 1.5$  and a mean subsurface temperature of  $10^\circ\text{C}$  (Fig. 6.4c). To demonstrate that  $K_{KC}$  yields representative results,  $K$  obtained by flow measurements are plotted for comparison. These measurements (Sass, 2010) were conducted on drill cores obtained at Eng08 and are corrected to  $10^\circ\text{C}$  using Equation 3.4. The volume susceptibility was measured on core samples (Rolf, pers. comm.) to evaluate the strength of the internal magnetic gradients and thus the expected impact on  $T_2^*$  due to dephasing (Fig. 6.4d). A gamma ray log (Grelle, pers. comm.), measuring the natural radioactivity in API, was conducted in the plastic-cased borehole to identify clay rich layers and layer boundaries with a high vertical resolution (Fig. 6.4e).

The medium sands of the Weichselian glacial reach down to 5 m with an average  $K$  of  $2.5 \times 10^{-4} \text{ m s}^{-1}$ . Flow measurements, done on samples from Eng08 with a higher vertical resolution, indicate that fine layers of low  $K$  values might be embedded in the medium sand. The sediments of the Saalian complex extend from 5 m to a depth of 10 m. The top 2 m layer consists of fine sand with slightly lower  $K$  of  $1.5 \times 10^{-4} \text{ m s}^{-1}$  and medium sand below with  $K$  of about  $6 \times 10^{-4} \text{ m s}^{-1}$ . The upper sediments of the Elsterian glacial between 10 and 14 m are not completely resolved by drill cores. The recovered material consists of medium sand and gravel with a significant amount of organic material. The increased amplitude of the natural gamma log helps to define the boundary of this layer and indicates an increased clay content, especially at the depth with core loss. The  $K$  values obtained from sieving analyses on the recovered material range from  $2$  to  $6 \times 10^{-4} \text{ m s}^{-1}$ . These values do not represent the parts of the layer that are not resolved by drilling. Because of the high clay content these parts are expected to show significantly lower  $K$  values. The till and boulder clay between 14 and 17 m mainly consists of silt and contains a significant amount of organic material. The layer shows low  $K$  values of about  $4 \times 10^{-5} \text{ m s}^{-1}$  which characterise this layer as an aquiclude. However, due to the limitations of the Kozeny-Carman like equation to predict  $K$  from

## 6. The hydrogeophysical test site Schillerslage

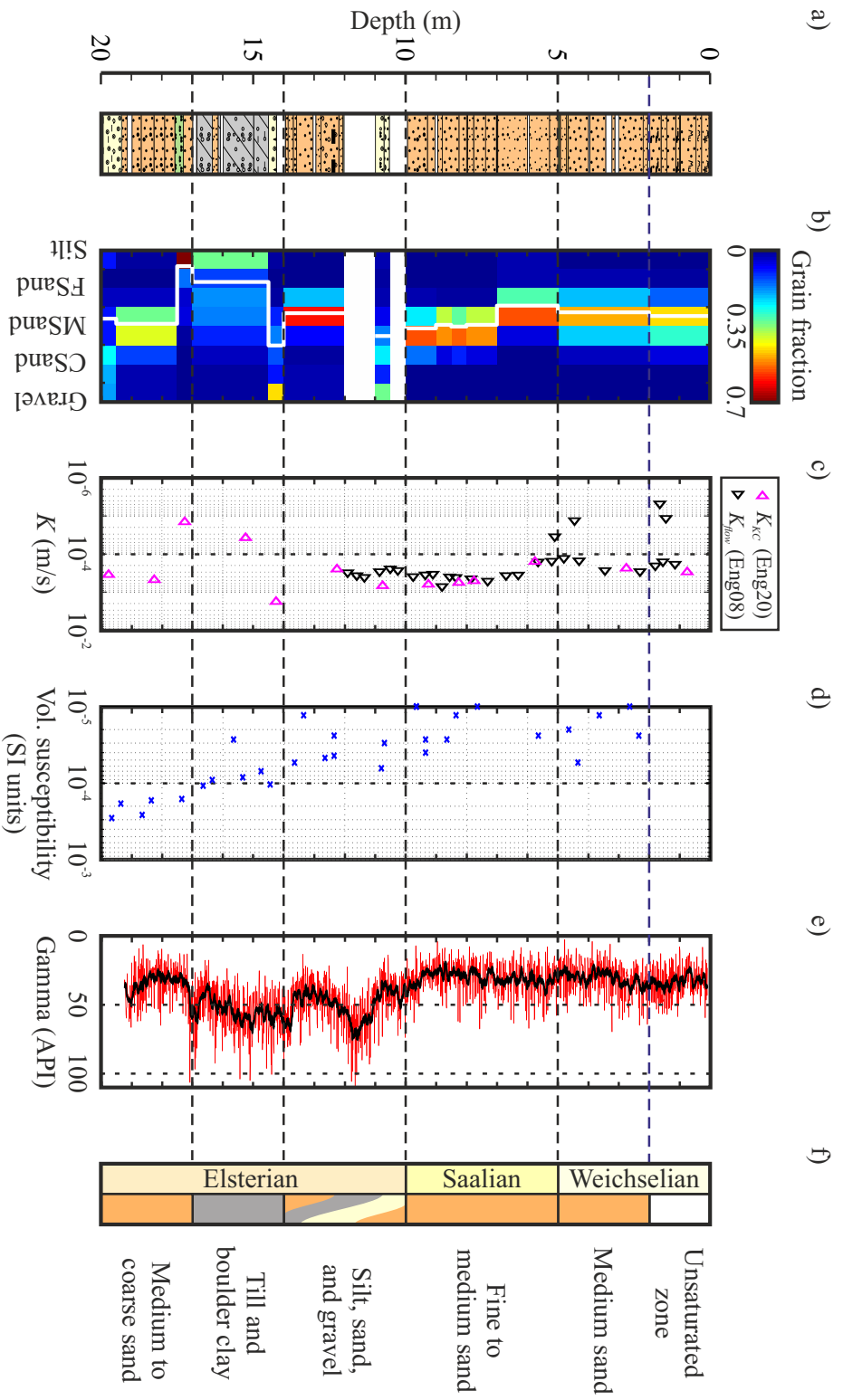


Figure 6.4.: Summary of the background information obtained at the Eng20 site. Lithology profile (a) (for key see Fig. 6.3) and conceptual model of Eng20 (f). Sieving analyses obtained from coring sleeves including  $d_{grain}$  (white line) (b) and  $K$  derived from grain-size analyses (Eq. 3.5) (c).  $K$  estimated by flow measurement on coring sleeves obtained at Eng08 plotted for comparison. Volume susceptibility (Rolf, pers. comm.) (d) from drill cores and gamma ray log (Grelle, pers. comm.) measured in the borehole (red) including moving average (black) (e).

sieving analyses in clay-rich material or on samples with a wide distribution of grain sizes (see Chap. 3.6.3) the actual  $K$  value of the layer might differ. Below, the sediments of the Elsterian glacial mainly consist of medium sand with an overall low clay content but thin interbeddings of coarse sands and limnic till. Apart from the till layer on top, the average  $K$  value is in the range of  $4 \times 10^{-4} \text{ m s}^{-1}$ .

#### 6.2.4. Summary of applied NMR methods

Several NMR methods were conducted on the Schillerslage site to obtain a comprehensive image of the shallow aquifers. All applied NMR methods have different specifications and therefore vary in  $\omega_0$ ,  $t_{\text{dteff}}$  and pulse sequences to measure different  $T$  as well as sizes and conditions of the probed volume as summarised in Table 6.1. The term  $t_{\text{dteff}}$ , defined by Dlugosch et al. (2011) for FIDs recorded by surface NMR, is used more generally in this chapter as the delay between the middle of the excitation pulse and the first data point of the final processed NMR signal.

Method	$\omega_0$ (kHz)	$t_{\text{dteff}}$ (ms)	$T$	Sample	
				Condition	Volume
Surface NMR	2.1	15 to 70	$T_2^*, T_1$	in situ	$>100 \text{ m}^3$
Earth's field NMR	2.1	25	$T_1$	drill core	$0.5 \text{ dm}^3$
Borehole NMR	245	2	$T_2$	in situ	$1 \text{ dm}^3$
Laboratory NMR	2000	0.2 to 1	$T_2, T_1$	disturbed	$0.02 \text{ dm}^3$

Table 6.1.: List of NMR methods with respective specifications:  $\omega_0$ ,  $t_{\text{dteff}}$ , measured  $T$  and details of the probed volume.

#### Surface NMR

Using large wire loops placed on the surface of the Earth, surface NMR allows imaging the subsurface in a non-invasive way. The method utilises the homogeneous but comparable weak homogeneous Earth's magnetic field and therefore requires sample volumes of several hundreds of cubic metres. Because there is no simple linear relation between pulse moment ( $q$ ) and the location from which the NMR signal originates, an inversion algorithm is used to reconstruct the distribution of water in the subsurface (see Chap. 4). Two different surface NMR surveys were conducted at the Schillerslage site both utilising circular loops with one turn and a diameter of 50 m.

## 6. The hydrogeophysical test site Schillerslage

The static magnetic background field has a strength of 49 135 nT and an inclination of 68°.

The 2D survey consists of seven COI loop setups located at p1 to p7 and arranged on a profile with an azimuth of 100°E. The data were collected in May 2009 using the NUMIS Lite equipment (IRIS Instruments, Orleans, France) with  $t_{\text{pulse}} = 40$  ms resulting in  $t_{\text{dteff}} = 63$  ms. The survey utilises a simple single pulse FID experiment to estimate  $T_2^*$ . This data set has been inverted using the 2D QTI code presented in Chapter 5.

In May 2012, a 1D survey was conducted at p1 using a phase-cycled pseudosaturation recovery scheme after Walbrecker et al., 2011 to achieve information about  $T_1$  and  $T_2^*$  in the subsurface. The survey consists of four soundings with different pulse delays (50, 100, 300 and 700 ms) between the two excitation pulses. The data were collected using the GMR equipment (Vista Clara Inc., Mukilteo, USA) using  $t_{\text{pulse}} = 10$  ms which results in a  $t_{\text{dteff}}$  of 15 ms for  $T_2^*$ . Including the shortest pulse delay,  $t_{\text{dteff}}$  increases to approximately 70 ms for  $T_1$ . The received data set has been inverted using an adapted QTI scheme after Müller-Petke et al., 2013.

### Earth's field NMR

Similar to surface NMR, Earth's field NMR relies on the comparably weak Earth's magnetic field as the background field for the NMR experiment. To increase  $\mathbf{M}_0$  (see Eq. 2.1) a magnetic pre-polarisation pulse is applied immediately before the start of the actual NMR pulse sequence which allows to probe significantly smaller samples. The pre-polarisation pulse of the used Terranova-MRI (Magritek, Wellington, New Zealand) equipment has a strength of up to 18.8 mT and a duration of several seconds, which is significant longer than  $T_1$ .

Varying the length of the delay between the pre-polarisation pulse and the 90° pulse allows estimating the  $T_1$ -relaxation of a sample (Callaghan and Le Gros, 1982). This was done using 19 logarithmically spaced delays ranging from 0 to 2 s and  $T_1$  was estimated by a subsequent monoexponential fit. Because a tuned circuit is used as a hardware filter to amplify the NMR signal, this leads to a comparable long  $t_{\text{dteff}}$  of 25 ms. In addition to  $T_1$ ,  $T_2^*$  can be estimated from the recorded FIDs. However, because the measured  $T_2^*$  were significantly shorter than expected, the presented data are limited to  $T_1$ . The short  $T_2^*$  times are most likely the result of instrumental effects of the Terranova-MRI or inhomogeneities in the magnetic background field.

The used Terranova-MRI has a sensitive volume of approximately 0.5 dm<sup>3</sup> and can be used to investigate segments of drill cores with a diameter of

up to 7 cm. Because it can be powered by a 24 V DC power source, the instrument can be easily set up in the field. The presented data were therefore collected on fresh drill cores immediately after they were pulled from the borehole.

Additionally to the drill cores, several fluid samples were taken from the aquifer between 5 and 10 m by pumping water from a screened observation well located close to Eng08. Immediately after extracting the fluid,  $T_B$  was estimated using a  $T_1$  measurement showing values of approximately 2.1 s.

### Borehole NMR

Borehole NMR utilises the strong artificial magnetic field of a permanent magnet inside the probe. This leads to a magnetic gradient field in the surrounding of the probe which allows sampling different sensitive volumes depending on the matching Larmor frequency ( $\omega_0$ ).

The presented survey was conducted using the Javelin system (Vista Clara Inc., Mukilteo, USA) working at 245 kHz. The gradient of the magnetic field  $\Delta\mathbf{B}_0$  sampled at 245 kHz is approximately  $0.08 \text{ T m}^{-1}$  (Grunewald, pers. comm., 2013). A CPMG pulse sequence with an inter-pulse spacing of 2 ms was used to estimate  $T_2$ . According to the more general definition of effective dead time used in this chapter, this leads to  $t_{\text{deff}}$  of about 2 ms. To obtain a  $T_2$  distribution from the recorded data an inversion was performed to estimate the  $w_j$  for 150 logarithmically spaced time bins between 5 ms to 3 s (see Chap. 3.5.3).

Two downhole probes with different diameters are available at the LIAG. The applied JP175(C) is only 45 mm thick and can therefore be deployed in slim groundwater observation wells. As a first approximation, the sensitive volume has the shape of an upright hollow cylinder with a height of 1 m and a slim layer of few millimetre located 120 mm from the centre of the probe. Because the auger to drill the observation well has a radius of 88 mm, the sensitive volume is expected to lie in the mainly undisturbed zone of the sediments. To increase the vertical resolution of the survey, overlapping measurements with an increment of 0.5 m were conducted.

### Laboratory NMR

Similar to the borehole application, NMR measurements in the laboratory utilise a strong artificial magnetic field. However, because the sample can be placed inside an arrangement of magnets, the magnetic background field shows less gradients inside the sensitive volume.

## 6. The hydrogeophysical test site Schillerslage

The presented measurements were conducted using a Rock Core Analyzer (Magritek, Wellington, New Zealand), working at 2 MHz. A CPMG pulse sequence with an echo spacing of 0.2 ms was used to estimate  $T_2$ . According to the definition of effective dead time used in this chapter, this leads to  $t_{\text{deff}}$  of about 0.2 ms. The  $T_1$ -relaxation was measured using an inversion recovery experiment with 20 logarithmically spaced pulse delays ranging from 1 ms to 4 s. Because of the contribution of the shortest pulse delay,  $t_{\text{deff}}$  is about 1 ms for the  $T_1$  experiment. To obtain a  $T_1(T_2)$  distribution from the data, an inversion was conducted to estimate the  $w_j$  for 150 (300) logarithmically spaced time bins ranging from 1 ms to 3 s (see Chap. 3.5.3).

A sample holder with a volume of 20 cm<sup>3</sup> was used to place the unconsolidated material into the sensitive volume of the laboratory NMR. To prepare a sample, the sample holder was first filled with degassed and deionised water to which sodium chloride was added to reach an electrical conductivity of 330  $\mu\text{S cm}^{-1}$ . Then, the dried and disturbed sub-sample from the drill core was slowly added to the water column to prevent air pockets. The material was gradually filled and compacted with a pestle to approximate undisturbed conductions as best as possible.

The built-in cooling system of the Rock Core Analyzer was used to ensure a constant sample temperature between 21 and 22 °C during the measurements. Because  $T_B$  is not only a function of temperature but can be altered by dissolved ions (see Chap. 3.2),  $T_B$  was estimated separately for every sample. Therefore, the pore fluid was extracted after the NMR experiments on each sample and  $T_2$  of the fluid was measured using a CPMG experiment.

## 6.3. Structural investigation

### 6.3.1. Electrical resistivity tomography

An ERT profile was conducted at the main profile to verify the structural information gained from the boreholes and to obtain a electrical resistivity model necessary to calculate  $\mathbf{G}$  for the inversion of the surface NMR measurements. The ERT survey was carried out in January 2012 using a Lippmann 4-point light 10W equipment (LGM, Schauffing, Germany). The data of a Wenner- $\alpha$  and Wenner- $\beta$  configuration and two electrode spacings of 2 and 5 m were merged into one data set. This data set was inverted using the Boundless Electrical Resistivity Tomography code described in Günther et al., 2006. The obtained electrical resistivity distribution is presented in

Figure 6.5a. Apart from artifacts at the start and end of the ERT profile due to a lack of model resolution, the electrical resistivity model does not indicate any 2D structures and agrees well with the conceptual 1D model of the lithology obtained from drilling (Fig. 6.5b).

A 1D block inversion was conducted on an averaged data set obtained from the ERT survey to obtain a more adapted electrical resistivity model. A model of five layers (Fig. 6.5c) with their respective layer boundaries matching well with drilling information (Fig. 6.5d) sufficiently explains this averaged data set. The first layer reaches down to 4.5 m and shows a high electrical resistivity of about  $500 \Omega \text{ m}$  which agrees well with the distribution of the medium sands of the Weichselian glacial. The water table at 2 m is not resolved by the 1D block inversion. Below 4.5 m, the medium sand of the Saalian complex shows still comparably high electrical resistivities of about  $300 \Omega \text{ m}$  with a lower boundary at 10 m. The top two layers of the Elsterian glacial are only resolved as one layer reaching down to 16 m. The medium electrical resistivities of  $85 \Omega \text{ m}$  are probably the result of the significant amount of silty material in the medium sand and gravel layers. Below 16 m, the lower sand layer of the Elsterian glacial leads to a rise in electrical resistivity of approximately  $200 \Omega \text{ m}$  which drops again to about  $20 \Omega \text{ m}$  for the marl bedrock.

#### 6.3.2. 2D surface NMR

A 2D surface NMR survey consisting of seven COI experiments, each separated by half the loop diameter (25 m), was conducted on the main profile of the Schillerslage site. Because the survey was carried out in 2009 using a NUMIS Lite equipment, the survey (i) does not include separated tx and rx loop configurations, (ii) only has a small pulse moment range of  $0.15 < q < 3 \text{ A s}$  and (iii) leads to a data set with  $t_{\text{dteff}} = 63 \text{ ms}$  (Fig. 6.6a) which is long compared to modern equipment.

To estimate the 2D sensitivity kernel ( $\mathbf{G}$ ) necessary for the inversion, the propagation of the magnetic excitation fields in the subsurface was calculated using the mean 1D electrical resistivity model (Fig. 6.5c) obtained from the ERT survey. In analogy to the other QTI examples presented in this work, the parameter  $r_z$  was set to 0.2 to prefer a horizontal layering and the data error was estimated from the stacking error of the FIDs. The achieved data misfit is presented in Figure 6.6b. The plot shows no structures, which implies that the obtained QTI result fully explains the measured data. However, similar to the Nauen field example, the large  $\chi^2$  value of 2.8 indicates that the used stacking error of the FIDs, which are

6. The hydrogeophysical test site Schillerslage

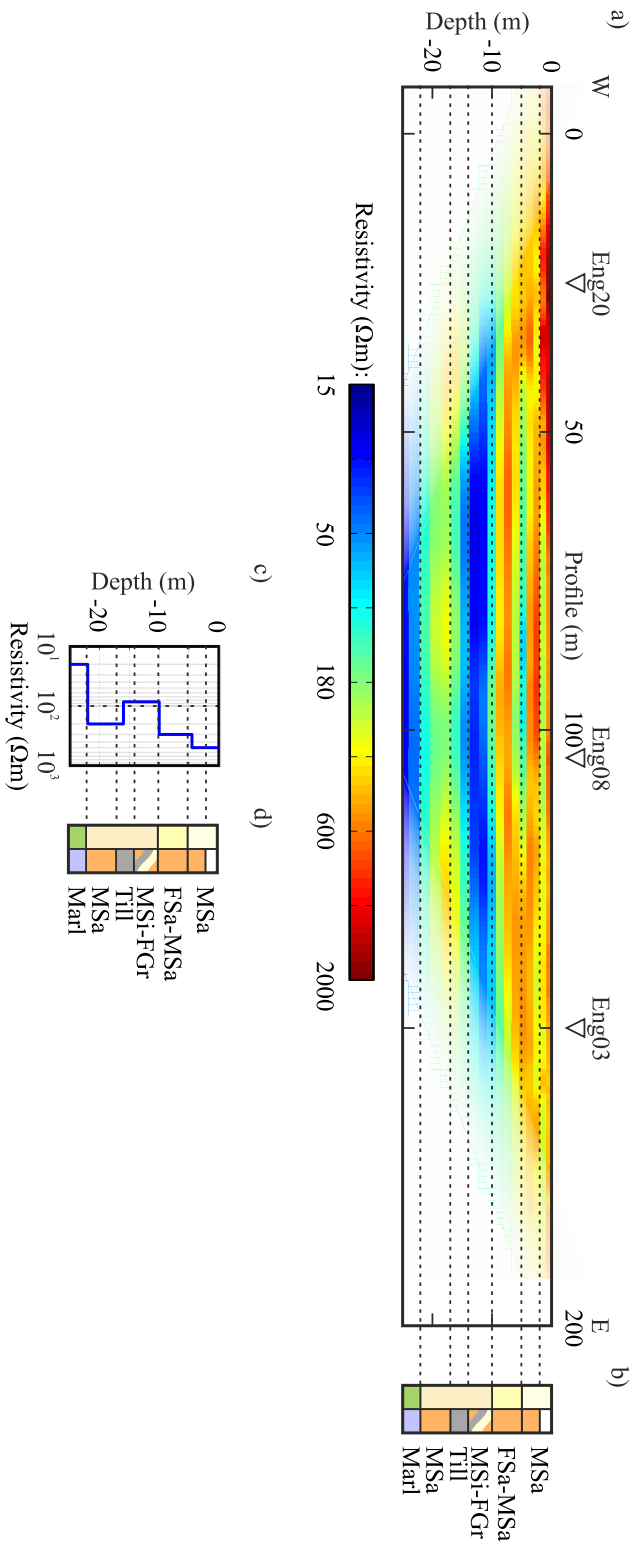


Figure 6.5.: ERT result of the electrical resistivity distribution at the Schillerslage site (a) and derived mean 1D electrical resistivity model (c). Conceptual 1D model of the lithology obtained from drilling (b and d) (see Fig. 6.3).

### 6.3. Structural investigation

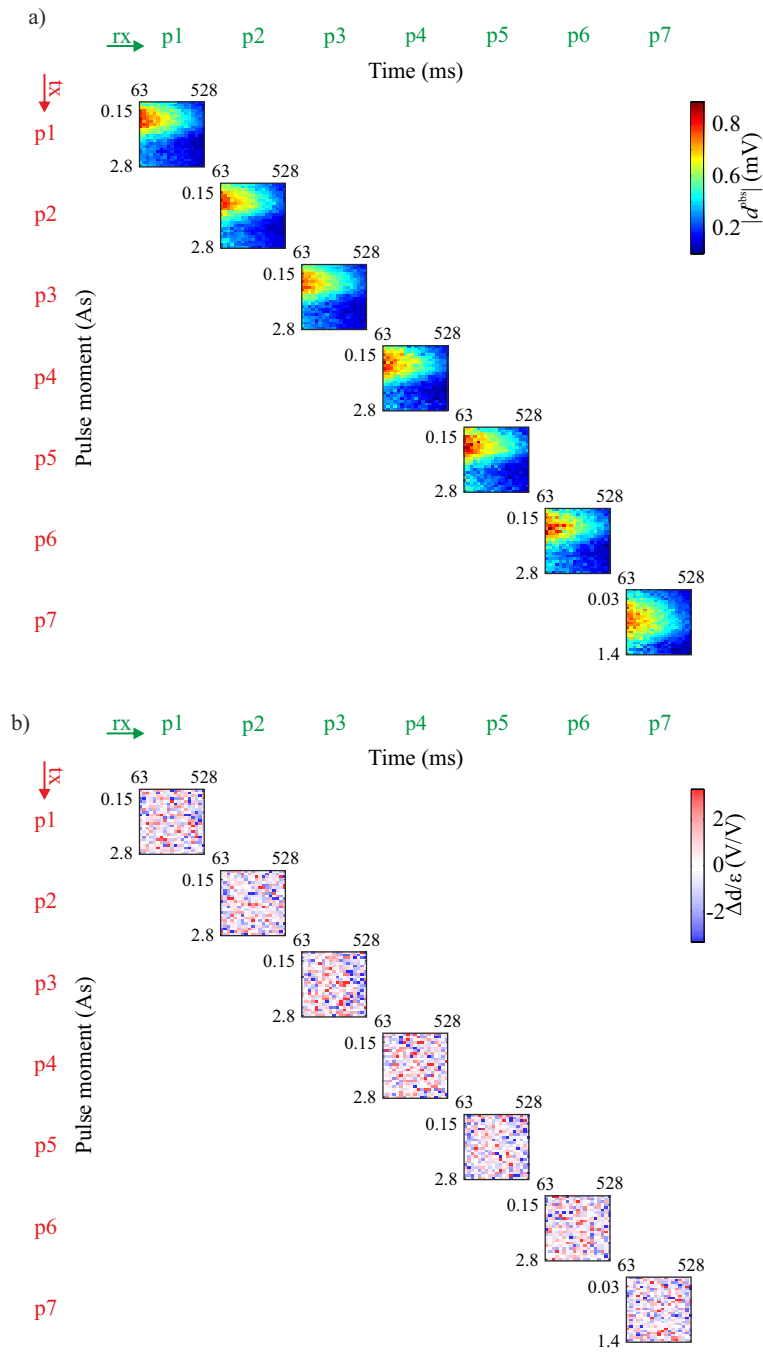


Figure 6.6.: (a) Data of the surface NMR survey conducted at the Schillerslage site. The matrix layout is consistent to Figure 5.1. (b) Error weighted data misfit ( $\chi^2 = 2.8$ ) of the QTI result presented in Figure 6.7.

6. The hydrogeophysical test site Schillerslage

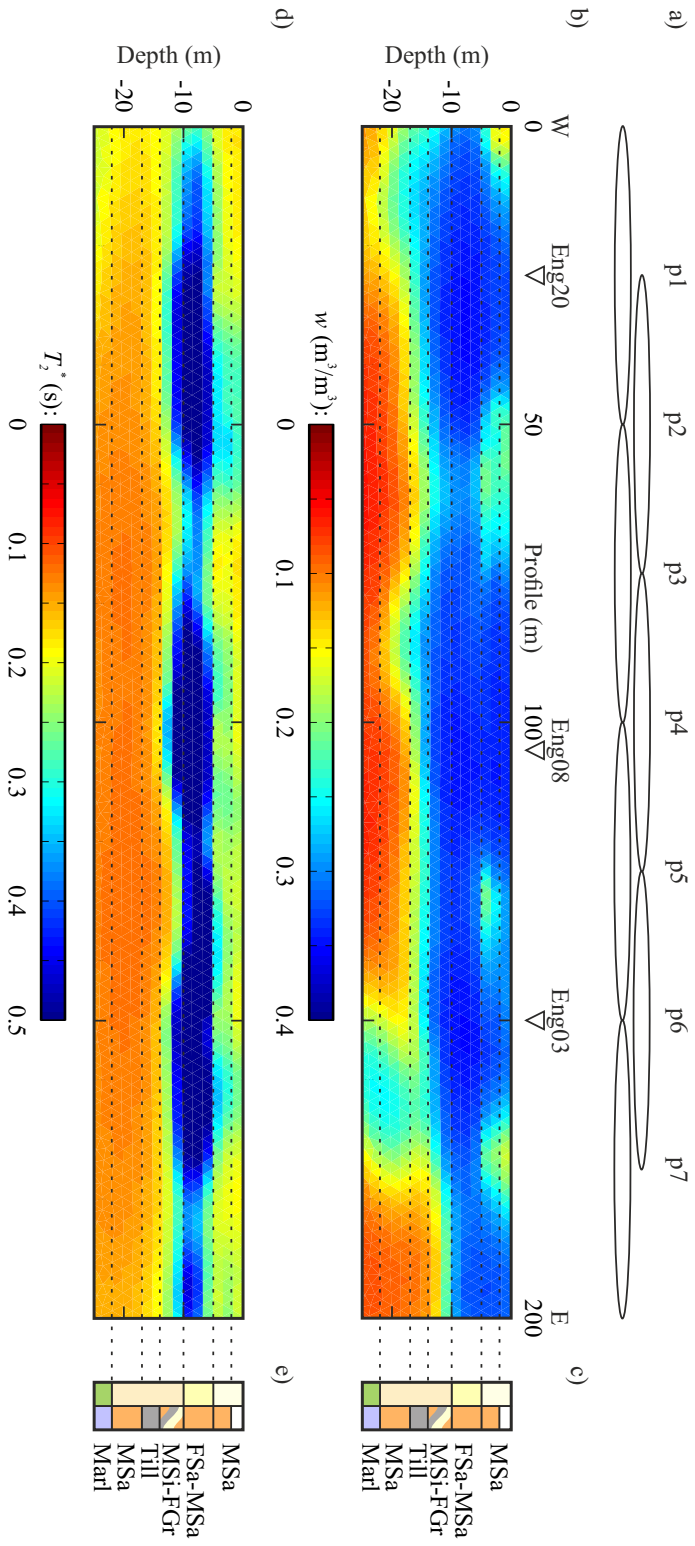


Figure 6.7.: Loop layout (a) and QTI result of the spatial  $w$  (b) and  $T_2^*$  (d) distribution obtained from the 2D surface NMR survey. For data and data misfit see Figure 6.6. (c, e) Conceptual 1D model of the lithology obtained from drilling (see Fig. 6.3).

already internally processed by NUMIS Lite equipment, underestimates the real data error for the Schillerslage data set.

As a first approximation, the QTI result presented in Figure 6.7 can be interpreted as a simple three layer model. The first layer, with  $w$  values of about 0.32 and  $T_2^*$  of approximately 0.2 s, matches the distribution of medium sand from the Weichselian glacial in the top 5 m of the subsurface. The lower  $w$  values in parts of this layer might be the consequence of the unsaturated zone not resolved by the QTI result. The second layer, with consistent  $w$  of about 0.32 but significantly higher  $T_2^*$  values  $> 0.4$  s, coincide in depth with the well sorted fine to medium sands of the Saalian complex. The boundary to the sediments of the Elsterian glacial below 10 m is not well resolved. The medium sand and gravel on top still show  $w$  of 0.3 but slightly faster  $T_2^*$  between 0.15 and 0.4 s. Below 14 m, the QTI result shows consistent  $T_2^*$  of about 0.15 s but a decrease in the NMR visible water content below 0.2. The QTI result of the 2D surface NMR survey does not resolve the lower aquifer consisting of medium to coarse sands. Instead, the  $w$  values show some lateral variations in the Elsterian glacial sediments. In general, this agrees well with the observations obtained from drill cores indicating an increased variability in lithology in this layer. However, because the pattern in  $w$  does not correlate with electrical resistivity anomalies from the ERT survey it is hard to evaluate if this pattern represents real 2D structures in the subsurface or are the result of the described limitations of the survey. Most limitations might have been overcome by a modern multi-channel equipment with a higher pulse moment range and a shorter effective dead time, as indicated by the increased resolution of the 1D surface NMR measurement presented in the following chapter.

## 6.4. Parameter investigation

Additionally to the 2D structural information gained from surface NMR surveys, the quality of the NMR parameters  $w$  and  $T$  and their potential to derive  $K$  using the Kozeny-Godefroy model (KGM) are evaluated at the Schillerslage site. A comprehensive survey was conducted at the drilling location Eng20 using all NMR methods available at the LIAG to characterise shallow aquifers.

## 6. The hydrogeophysical test site Schillerslage

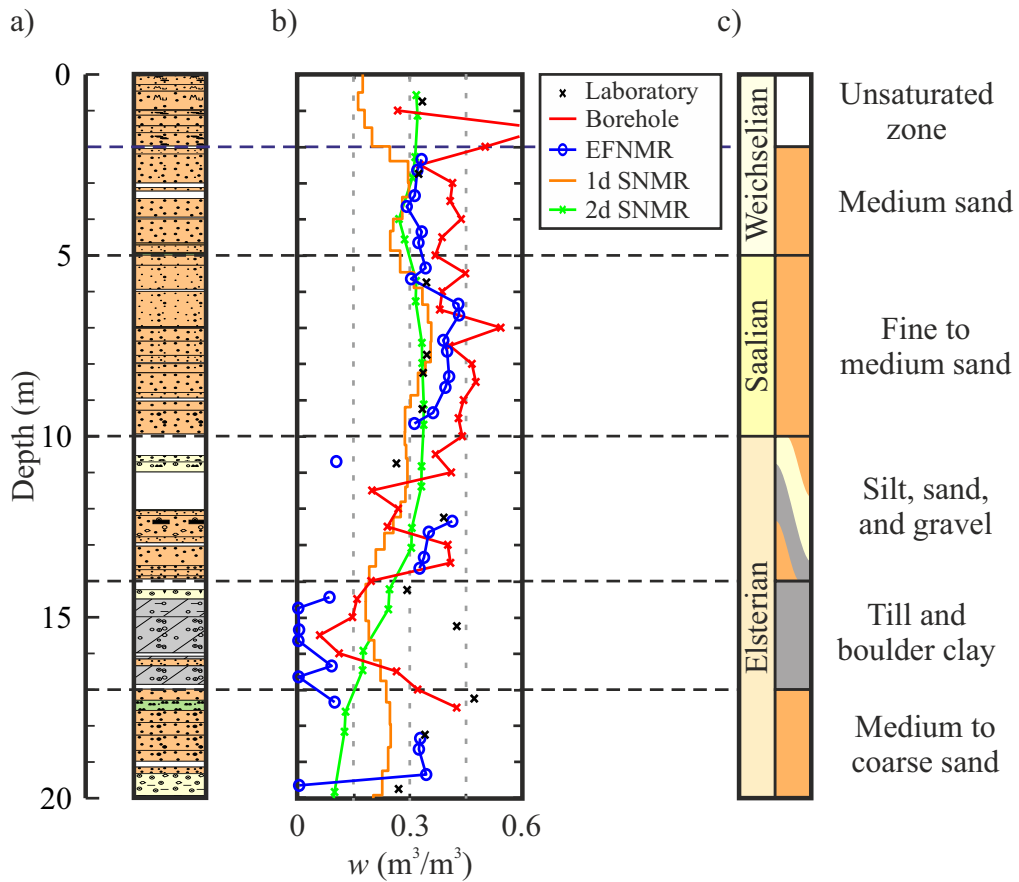


Figure 6.8.: Lithology profile (a) and conceptual model (c) of the Eng20 drilling (see Fig. 6.3). Comparison of  $w$  obtained by different NMR methods (b).

### 6.4.1. NMR water content

A comparison of  $w$  obtained from laboratory, borehole, Earth's field and surface NMR measurements is presented in Figure 6.8. Laboratory NMR measurements show water contents of about 0.35 in most parts of the Eng20 profile. A deviation to higher  $w$  values up to 0.48 in fine material and lower  $w$  values down to 0.27 in coarse material can be observed respectively. Because the dry samples were re-saturated, laboratory NMR measurements cannot resolve the unsaturated zone above 2 m. The comparably high  $w > 0.4$  in silty material originates from water with short  $T_2 < 10$  ms which includes bound water.

Borehole NMR measurements at Eng20 show a mean  $w$  in the top 10 m of approximately 0.44. This is significantly higher than the water content obtained by other NMR methods. Part of these high  $w$  values originate from water with  $T_2 < 10$  ms. Because of the instrumental  $t_{\text{dteff}}$  of 2 ms, this fast relaxing water is hardly resolved. Between 1.5 and 2 m, even higher  $w$  values of up to 0.67 were measured. These high  $w$  values most likely originate from a 0.2 m peat layer verified by a soil sampler at a depth of 1.8 m. The till and boulder clay layer between 14 and 17 m and the clay rich layers between 11.5 and 12.5 m are traced by low  $w$  of  $< 0.15$  and  $< 0.3$ , respectively.

The water content estimated by Earth's field NMR on drill cores obtained from the first 5 m shows values of about 0.32. This agrees well with laboratory NMR measurements on re-saturated material from respective depths. Below, the water content in the medium sands of the Saalian complex raises slightly to about 0.4. The other sandy parts of the profile below 10 m show a similar range of  $w$  values. Layers with very coarse material (10.75 and 19.75 m) as well as very fine material (between 14 and 17 m) are equally characterised by low  $w$  values.

The water content obtained from both, 1D and 2D surface NMR surveys shows values of about 0.32 for the aquifers above 10 m. The change in lithology at about 4 to 5 m is indicated with reduced  $w$  values below 0.3. The upper sediments of the Elsterian glacial between 10 and 14 m are also characterised by decreasing  $w$  values. This agrees well with the increasing clay content and the comparable long  $t_{\text{dteff}} > 15$  ms for surface NMR leading to an underestimation of the water content. The results of both surveys differ in the unsaturated zone above 2 m and the aquifer below 17 m which can only be resolved by the 1D survey. This is probably due to the smaller  $q$  range and longer  $t_{\text{dteff}}$  of the 2D data set.

### 6.4.2. Transverse NMR relaxation time ( $T_2$ )

#### Distribution of relaxation times

Laboratory and borehole NMR measurements were used to estimate the distribution of transverse NMR relaxation times, i.e.  $w_j$  versus  $T_2$  bins, on a depth profile at Eng20. The results are presented in Figure 6.9b and c respectively. The maximum and mean of the logarithms (Eq. 3.9) of each  $T_2$  distribution and the result of a monoexponential data fit are presented to visually evaluate how these values comprise the information of the  $T_2$  distribution into a representative number. Additionally, the  $T_B$

6. The hydrogeophysical test site Schillerslage

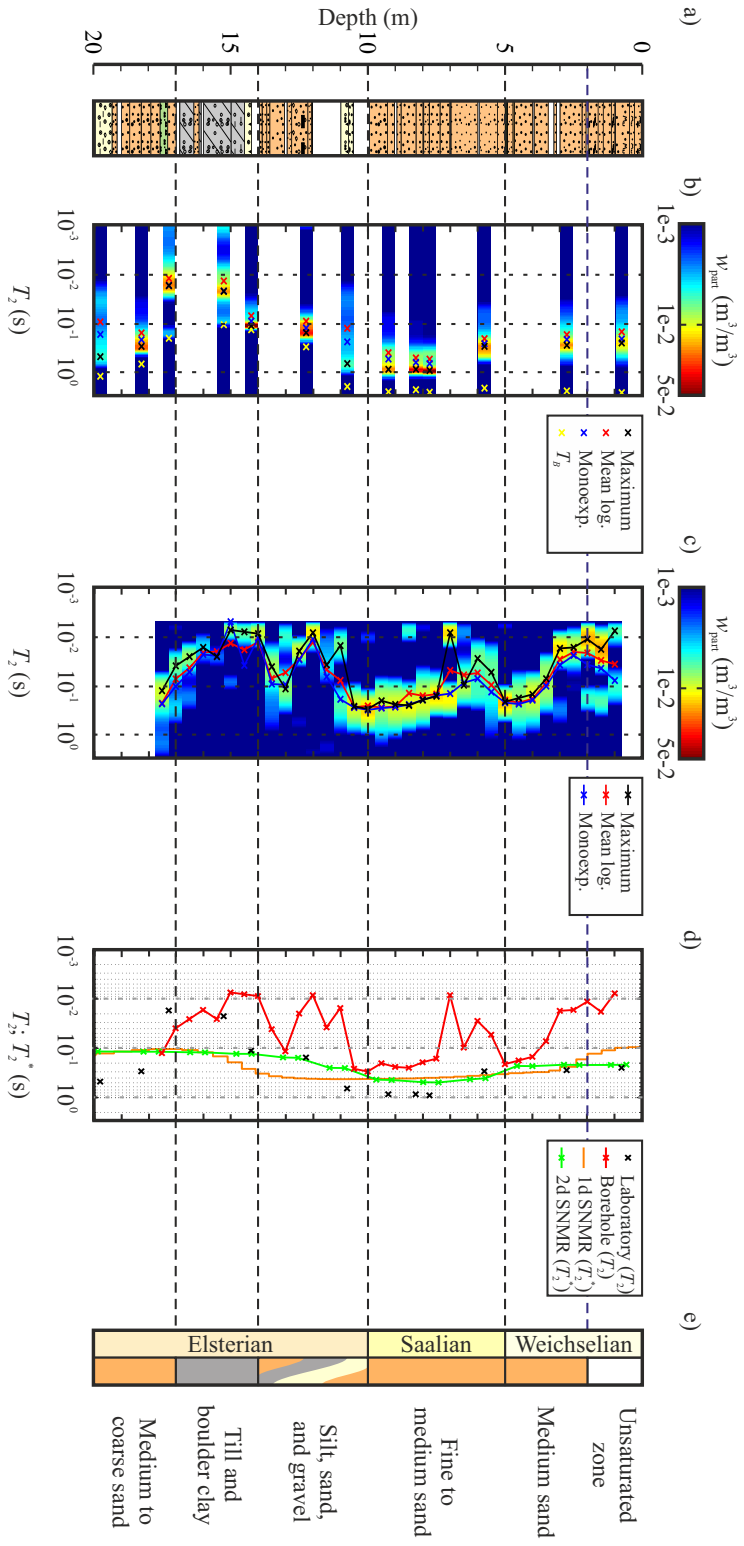


Figure 6.9: Lithology profile (a) and conceptual model (e) of the Eng20 drilling (see Fig. 6.3).  $T_2$  distribution with respective maximum and mean of the logarithms and monoexponential data fit estimated on samples (b) using laboratory NMR and (c) borehole NMR measurements.  $T_B$  of the pore fluid from separate  $T_2$  measurements for comparison (b). Summary of  $T_2$  and  $T_2^*$  values obtained by different NMR methods (d).

values measured on the extracted pore fluid of the re-saturated laboratory samples were plotted for comparison (Fig. 6.9b).

Most  $T_2$  distributions obtained from laboratory NMR are quite narrow indicating a narrow distribution of pore sizes. Note that the visible width of the distributions presented in Figures 6.9b and c are highly amplified by the logarithmic colour scale used for  $w_j$ . Because of the mainly narrow  $T_2$  distributions and in analogy to the reasons discussed in Chapter 3.6.4, the maximum of each distribution was chosen to represent each  $T_2$  measurement. The obtained  $T_{ML}$  and the monoexponential data fit are systematically shorter than the maximum of the  $T_2$  distribution ( $T_{ML} < \text{monoexponential} < \text{maximum}$ ). Samples with a wide or multiexponential distribution of  $T_2$  times can be found in the sediments of the Elsterian glacial below 10 m. Two of these samples were taken from the gravel layers at 10.75 and 19.75 m respectively which both contain a high silt content. The boulder clay probed at 14.75 m and the limnic till layer located at the top of the lower aquifer at 17.25 m not only shows a wide  $T_2$  distribution including short  $T_2$  times but also a quite distinct peak at several deciseconds. By comparing the relaxation times of these peaks to the value of  $T_B$ , their origin can be identified as excessive water which was not removed properly from the top of the sample after re-saturation.

Compared to laboratory NMR, the  $T_2$  distributions obtained from borehole NMR are commonly wider. Additionally, clearly multiexponential NMR signals can be observed in the unsaturated zone  $< 2$  m, in a thin layer at 7 m and in several parts of the sandy aquifer of the Elsterian glacial below 10 m. In contrast to the laboratory NMR measurement, the boulder clay shows a narrower  $T_2$  distribution. Another difference between the  $T_2$  distributions obtained by both NMR methods is, that at several depths the maximum of the borehole NMR distribution leads to faster  $T_2$  times than the respective  $T_{ML}$ . To focus on the strongest NMR signal of the sampled volume and to be consistent with the laboratory NMR measurement, the maximum of a distribution is chosen to be representative for the depth.

### Single representative relaxation time

To be able to compare the transverse relaxation times obtained from different NMR methods, the maxima of the  $T_2$  distributions estimated using laboratory and borehole NMR as well as the monoexponential  $T_2^*$  results from the two surface NMR surveys are summarised in Figure 6.9d. The  $T_2$  values obtained from laboratory NMR measurements characterise the first 5 m of the depth profile, which includes the sediments of the

## 6. The hydrogeophysical test site Schillerslage

Weichselian glacial and the upper fine sands of the Saalian complex, with  $T_2$  of about 0.25 s. Below, the medium sands show higher  $T_2$  values of about 0.8 s which gradually drop down to 0.15 s for the sandy parts of the upper Elsterian glacial. The boulder clay and limnic till with very short  $T_2$  times of several deciseconds show a good contrast to the underlain medium to coarse sands of the Saalian complex with long  $T_2$  times of 0.3 to 0.5 s.

In most parts of the profile, the  $T_2$  from borehole NMR are significantly shorter than  $T_2$  obtained by laboratory NMR or even  $T_2^*$  obtained by surface NMR. This order does not change if the means of the logarithms of both distributions are chosen instead of their maxima. The longest estimated  $T_2$  times are 0.2 s in the sediments of the Weichselian glacial (4 to 5 m), 0.3 s for the Saalian complex (7.5 to 10.5 m) and 0.2 s in the Elsterian glacial sands (13 and 17.5 m). Three depth intervals with very short  $T_2$  times of only several hundredths of a second can be identified at about 1 to 3 m, 6 to 7 m and 11 to 12.5 m which are not visible in the laboratory NMR result.

The result of the 1D surface NMR survey resolves four layers with different  $T_2^*$  times. The first layer with  $T_2^*$  of 0.1 s reaches down to 2 m and matches the unsaturated zone. The second layer with  $T_2^*$  of 0.3 s reaches down to a depth of about 5 m which agrees with the distribution of medium sand of the Weichselian glacial. Below,  $T_2^*$  smoothly rises reaching 0.4 s in the upper sediments of the Elsterian glacial at about 13 m. In the boulder clay and lower sediments of the Elsterian glacial below 14 m,  $T_2^*$  drops gradually to about 0.1 s. Because of the low  $w$  values in the unsaturated zone and the boulder clay, the obtained  $T_2^*$  values might be hardly resolved.

Compared to the 1D survey, the  $T_2^*$  result extracted from the 2D surface NMR survey (Fig. 6.7) at the location of Eng20 does not resolve the unsaturated zone. A three layer model therefore sufficiently characterises the subsurface. It consists of the sediments of the Weichselian glacial down to 5 m with  $T_2^*$  times of about 0.23 s, the sediments of the Saalian complex between 5 and 10 m with  $T_2^*$  times of about 0.45 s and the sediments of the Elsterian glacial below 10 m with a gradual change in  $T_2^*$  from 0.15 to 0.1 s. Therefore, both surface NMR surveys show quite consistent  $T_2^*$  values but, similar to the  $w$  result presented in Figure 6.8, resolve the unsaturated zone and the upper sediments of the Elsterian glacial between 11 and 14 m differently.

### 6.4.3. Longitudinal NMR relaxation time ( $T_1$ )

#### Distribution of relaxation times

A distribution of  $T_1$  times was only obtained from laboratory NMR measurements. The results, plotted on a depth profile, are presented in Figure 6.10b. The characteristics of the obtained  $T_1$  distributions, i.e. relative width and multiexponential behaviour, agree well with the  $T_2$  distributions obtained from the same samples at respective depths (see Fig. 6.9b). Probably because of the lower signal-to-noise ratio, the absolute width of each  $T_1$  distribution is slightly broader compared to the respective  $T_2$  distribution. Additionally, the peaks visible at  $T_B$  in two  $T_2$  distributions, which most likely origin from excessive pore fluid on top of the samples, can only be detected in the  $T_1$  distribution measured at the sample obtained from 17.25 m. In analogy to  $T_2$ , the maximum of each  $T_1$  distribution was chosen to represent the sample.

#### Single representative relaxation time

The  $T_1$  values obtained at Eng20 using laboratory, Earth's field and surface NMR are presented in Figure 6.10c. The  $T_1$  time obtained by laboratory NMR therefore starts in the first 6 m at about 0.33 s, rises to a value of about 0.8 s between 6 and 10 m and drops down to 0.16 s for the sandy parts of the upper Elsterian glacial. The boulder clay and limnic till between 15 and 17.5 m show very short  $T_1$  times of several hundredths of a second. In the medium to coarse sands below 17.5 m,  $T_1$  rises again to about 0.4 s. Overall, the  $T_1$  values obtained by laboratory NMR are very similar to the respective  $T_2$  values (Fig. 6.9c) showing only a slight shift ( $T_1 \approx 1.1 T_2$ ) to longer relaxation times.

The  $T_1$  values estimated by Earth's field NMR start at about 0.3 s for the saturated zone between 2 and 6 m and show an anomaly of high  $T_1$  values of up to 0.6 s at 4.5 m. Below, in the sands of the Saalian complex between 6 and 10 m, the  $T_1$  times rise to about 0.5 s. In the sandy part of the upper Elsterian glacial sediments, the  $T_1$  times rise further reaching 0.5 to 0.7 s. The lower sandy parts of the Elsterian glacial sediments below 17 m again show high  $T_1$  values of about 0.7 s which drop to 0.5 s at 20 m. Because of the long  $t_{\text{dteff}}$  and the low signal-to-noise ratio of Earth's field NMR measurements, the  $T_1$  times estimated on samples with a NMR visible  $w < 0.1$  were classified as unreliable and therefore are not presented in this work.

6. The hydrogeophysical test site Schillerslage

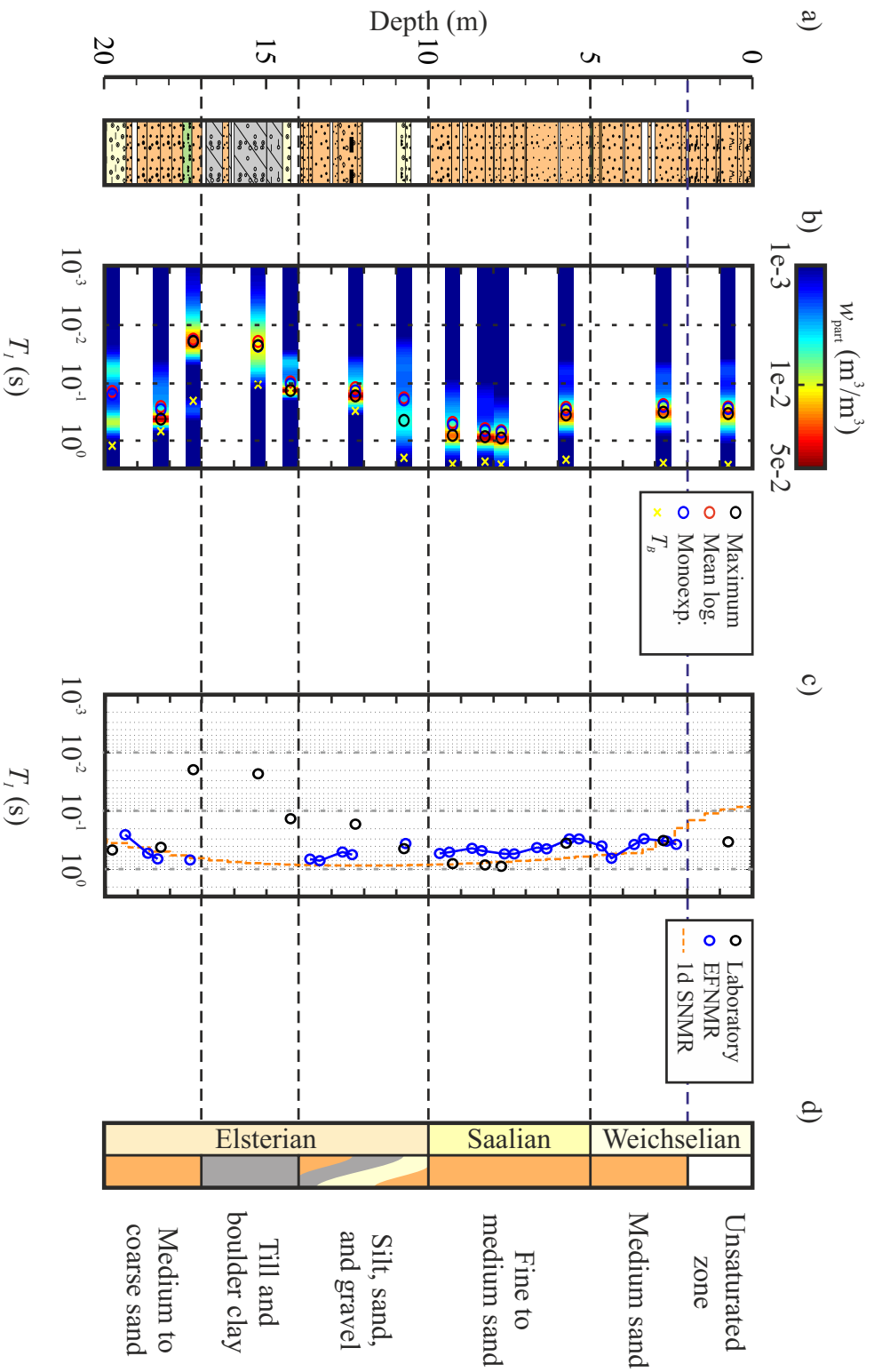


Figure 6.10.: Lithology profile (a) and conceptual model (d) of the Eng20 drilling (see Fig. 6.3).  $T_1$  distributions with respective maxima and mean of the logarithms and monoexponential data fits estimated on samples using laboratory NMR measurements (b).  $T_B$  of the pore fluid from separate  $T_2$  measurements for comparison. Summary of  $T_1$  values obtained by different NMR methods (c).

The  $T_1$  times obtained from the 1D surface NMR start at 0.1 s for the unsaturated zone, increase to about 0.5 s for the medium sands of the Weichselian glacial and smoothly rise to a maximum of 0.84 s at about 12 m. Below, the lower part of the Elsterian glacial sediments show  $T_1$  times of about 0.3 s. As indicated by the low  $w$ , the boulder clay is not resolved by the surface NMR survey due to the long  $t_{\text{deff}}$ .

#### 6.4.4. Impact of method specific properties on the obtained NMR parameters

The applied methods to obtain the NMR parameters at Eng20 differ in many aspects. The most obvious are:

- used pulse sequence (CPMG or FID),
- condition of the sampled volume (in situ, drill core, disturbed),
- impact of the pore water ( $T_B$ ),
- length of the effective dead time ( $t_{\text{deff}}$ ),
- resolution at different depth (local or surface measurement),
- model used to estimate a representative  $T$  (multi- or monoexponential),
- Larmor frequency ( $\omega_0$ ) of the NMR experiment,
- calibration of the NMR water content.

All these properties have an impact on the estimated  $w$ ,  $T_2$ ,  $T_2^*$  and  $T_1$  values and need to be considered when interpreting the results. Because of the ambiguous impact of several properties and the lack of systematic measurements, this section holds a discussion rather than a study.

#### Pulse sequence

The expected impact of the used pulse sequences, CPMG or FID, to estimate the transverse relaxation time, and thus the difference between  $T_2$  and  $T_2^*$ , depends on the strength of the magnetic field gradients in a sample. A volume susceptibility of a sample  $> 1.3 \times 10^{-4}$ , given in the International System of Units (SI), can provide an indication for high internal magnetic gradients leading to  $T_2^* < T_2$  (Grunewald and Knight, 2011a). To evaluate

## 6. The hydrogeophysical test site Schillerslage

the impact of internal magnetic gradients on the NMR measurements at Eng20, the volume magnetic susceptibility was measured on the drill cores (Fig. 6.4). The susceptibility values are  $< 1.3 \times 10^{-4}$  SI down to a depth of 17 m and below rise slightly to  $3 \times 10^{-4}$  SI. Therefore, the impact of internal magnetic gradients on  $T_2^*$  is expected to be very small for the Schillerslage site. This is especially true because the limit of  $1.3 \times 10^{-4}$  SI was approximated for a fluid temperature of  $15^\circ\text{C}$  and thus a higher  $D$  than the cooler in-situ conditions ( $10^\circ\text{C}$ ) probed by surface NMR.

Another source for magnetic gradients can be an artificial background field with a well defined field-strength gradient ( $\Delta\mathbf{B}_0$ ), as for example used by borehole NMR. Independent of their origin, the impact of magnetic gradients on the measured  $T_2$  time can be reduced when using a CPMG pulse sequence. After Equation 2.7, the effectiveness of a CPMG pulse sequence primarily depends on the length of the inter-echo spacing  $t_{es}$ . Because laboratory NMR can utilise a very short inter-echo spacing, e.g. 0.2 ms for the presented data, the impact of  $T_D$  on  $T_2$  is commonly ignored for material with a low susceptibility. Based on information provided by the manufacturer, the used NMR borehole tool has a  $\Delta\mathbf{B}_0$  of  $0.08 \text{ T m}^{-1}$  and uses an inter-echo spacing of 2 ms. After Equation 2.7, this leads to an additional relaxation process with  $T_D = 4.7 \text{ s}$ . The impact on the presented  $T_2$  data due to  $T_D$  is therefore  $< 0.02 \text{ s}$  which does not explain the overall significant shorter  $T_2$  times obtained by borehole NMR compared to laboratory NMR. To improve the interpretation of future measurements, the information provided by the manufacturer about  $\Delta\mathbf{B}_0$  and thus amplitude of  $T_D$  should be verified. This can be done using several NMR experiments with variable  $t_{es}$  conducted in a water tank with known  $T_B$  and  $D$ .

### Sample condition

The impact of the different conditions of the probed material, in-situ, drill core, or disturbed sample, on the NMR measurements are complex and therefore difficult to evaluate. Only borehole and surface NMR measurements sample the material under in-situ conditions. However, because both methods show large differences in the achieved  $w$  and  $T$  values, this makes a clear identification of artifacts which originate from the condition of the sample difficult.

Assuming that disturbed material has a lower compaction than under in-situ conditions, e.g. due to the lower burden, the expected effects on the NMR parameters are a higher  $w$  and longer  $T$ . Indications for this are the high  $w$  values in the boulder clay between 14 and 17 m and the exceptional

long  $T_2$  and  $T_1$  times between 7 and 11 m which can only be observed in the disturbed samples used by laboratory NMR.

Changes in the saturation of a sample, e.g. because of spilled water or an imperfect re-saturation of a dry sample, can lead to altered  $w$  values. A spilling of water and thus a reduced saturation was observed when drill cores filled with coarse material, and thus high  $K$ , were pulled out of the ground. A re-saturation of these cores was attempted, but the possibilities in the field were limited to simply adding water on top of the drill cores. This might explain the low  $w$  value estimated by Earth's field NMR, e.g. on the drill core filled with gravel obtained from a depth of 10.75 m. On the other hand, the samples obtained from the unsaturated zone were intentionally saturated in the laboratory to achieve porosity and pore-size information.

### Bulk water relaxation

The bulk water relaxation ( $T_B$ ) is an upper limit for each measured  $T$  time and can obscure pore-size information when ignored. Its impact on the measured  $T$  is only negligible for  $T_B \gg T$  (see Eq. 3.6 and 3.10). The value of  $T_B$  is hard to access because it needs to be estimated by a separate NMR measurement on the extracted pore fluid.

To estimate  $T_B$  of the in-situ pore fluid in the field, water was pumped out of an observation well located at Eng08 which was screened between 5 and 10 m. Immediately after the extraction,  $T_B$  was estimated by Earth's field NMR measurement showing values of about 2.1 s. A more depth specific sampling of the pore fluids was not possible and no sample could be obtained from depths below 10 m. Additionally, it is likely that the fluid was preferentially extracted from parts of the aquifer which have the highest  $K$  values.

During the preparation of the laboratory NMR samples  $T_B$  of the fluid was monitored. All samples were re-saturated using the same fluid with  $T_B$  of 2.48 s. After the NMR measurements on the saturated samples, the pore fluid was extracted and  $T_B$  was estimated individually for each sample. For the first 10 m of the depth profile,  $T_B$  seems to be unaffected by the saturation process. Below 10 m, the  $T_B$  times measured on the extracted fluid are significantly shorter (see Fig. 6.9).  $T_B$  changes smoothly with depth, reaching a minimum of  $T_B = 0.1$  s at about 15 m and rises back to  $T_B > 1$  s at 20 m. The assumption  $T_B \gg T$  is clearly violated for several measurements below 10 m.

This large change of  $T_B$  was not expected for natural material and indicates a high concentration of dissolved paramagnetic substances in

## 6. The hydrogeophysical test site Schillerslage

the pore fluid (Coates et al., 1999). Although suspiciously low  $T_2$  values were already reported for the re-saturated samples gained from deeper drill cores at the Nauen site (Müller-Petke (2009) and see Chap. 5.4), a large impact of  $T_B$  has not been considered yet. A further study needs to evaluate if the observed variations of  $T_B$  are also representative for in-situ conditions or are the consequence of the re-saturation of dried up samples. A first indication can be the increased amount of organic material, found in samples from Eng20 with short  $T_B$  times, which can lead to chemical processes when exposed to aerobic conditions. The unknown variation of  $T_B$  under in-situ conditions bears a large uncertainty when comparing the results of laboratory NMR with other NMR methods at depths below 10 m. On the other hand, indications that the short  $T_B$  times observed in the laboratory are not representative for in-situ conditions are the long  $T$  times measured by Earth's field and 2D surface NMR on samples below 10 m.

### Effective dead time

The impact of the effective dead time ( $t_{\text{dteff}}$ ) on the estimated NMR parameters depends on the  $T$  time of the sample and the signal-to-noise ratio of the measurement (Dlugosch et al., 2011). If  $t_{\text{dteff}}$  is long enough that a part of a multiexponential NMR signal has already been decayed, this leads to an underestimation of  $w$ , a narrower  $T$  distribution and an overestimation of  $T$  when calculating  $T_{ML}$ .

The strongest effect of  $t_{\text{dteff}}$  on the measurements at Eng20 can be observed in the boulder clay layer between 14 and 17 m. Compared to laboratory NMR ( $t_{\text{dteff}} = 1$  to 0.2 ms),  $w$  estimated by borehole NMR ( $t_{\text{dteff}} = 2$  ms) and Earth's field NMR ( $t_{\text{dteff}} = 25$  ms) is lower dependent on the respective length of  $t_{\text{dteff}}$  (see Fig. 6.8). Additionally, the width of the  $T_2$  distributions estimated from borehole NMR is smaller compared to laboratory NMR (see Fig. 6.9). The impact of  $t_{\text{dteff}}$  on the surface NMR measurements ( $t_{\text{dteff}} > 15$  ms) is similar. However, the parameters estimated by surface NMR are additionally affected by the smoothness constraints used during the inversion and the reduced resolution with depth as discussed in the following.

### Depth resolution

All applied NMR methods have different abilities to resolve the NMR parameters with depth. By sampling drill cores, laboratory and Earth's field NMR have the advantage to receive the NMR signals from a comparable

small and depth specific volume (see Tab. 6.1). It is therefore easy to ensure that the obtained information about  $w$  and  $T$  are from a single lithological unit. A comparison of  $T_1$  and  $T_2$  values obtained by laboratory and Earth's field NMR are presented in Figure 6.11b. The  $T_1$  times obtained from laboratory and Earth's field NMR agree well at the depth interval above 7 m. Between 7 and 14 m the results are inconsistent with longer  $T$  times estimated by laboratory NMR in the upper part and significant shorter  $T$  times in the part below 10 m. The lower  $T_1$  values obtained by laboratory NMR agree better with the increased clay content indicated by the natural gamma ray log at the respective depth (see Fig. 6.4e). However, the samples used for laboratory measurements are disturbed from in-situ conditions and the measurements at this depth are significantly affected by  $T_B$ . Below 18 m, the  $T$  times obtained from both methods differ but do not show a consistent trend. This might be the result of vertical lithological variations which are not consistently resolved by both methods.

Although the volume sampled by borehole NMR is small, the vertical length of the sensitive volume is approximately 1 m and thus rather large. Therefore, a single borehole NMR experiment can integrate signals from different lithologies or saturation conditions. This might explain the increased number of wide or even clearly multiexponential distributions observed by borehole NMR especially in the unsaturated zone between 1 and 2 m (see Fig. 6.9). The  $T_2$  times obtained from borehole NMR are systematically shorter than  $T$  from other methods (Fig. 6.11b). The amplitude of this shift exceeds the expected difference between  $T_1$  and  $T_2$ , e.g. as observed by laboratory NMR, or the expected impact of  $T_D$ . Nevertheless, because of the continuous and comparable high sampling rate of Earth's field and borehole NMR, the obtained  $T$  profiles consistently resolve structures in the first 10 m. These are anomalies of long  $T$  times at about 4 to 5 m, shorter  $T$  times in the upper part of the fine sands of the Saalian complex and a rise to longer  $T$  times in the coarser sediments below 7 m.

The signals recorded by surface NMR integrate over the largest volume of all presented methods. The ability to resolve the NMR parameters  $w$  and  $T$  on a depth profile is obtained by conducting and inverting several surface NMR experiments with different  $q$  values. In general, this leads to a low resolution of  $T$  in layers with low  $w$  and an overall reduced resolution in  $w$  and  $T$  with depth. For a detailed study on the sensitivity of surface NMR and the applied QTI see Müller-Petke (2009), Mueller-Petke and Yaramanci (2010) and Müller-Petke et al. (2013). The different results for  $T$  obtained by surface NMR at Eng20 are presented in Figure 6.11c. Dependent on the range of  $q$  and the signal-to-noise ratio of the data set,

6. The hydrogeophysical test site Schillerslage

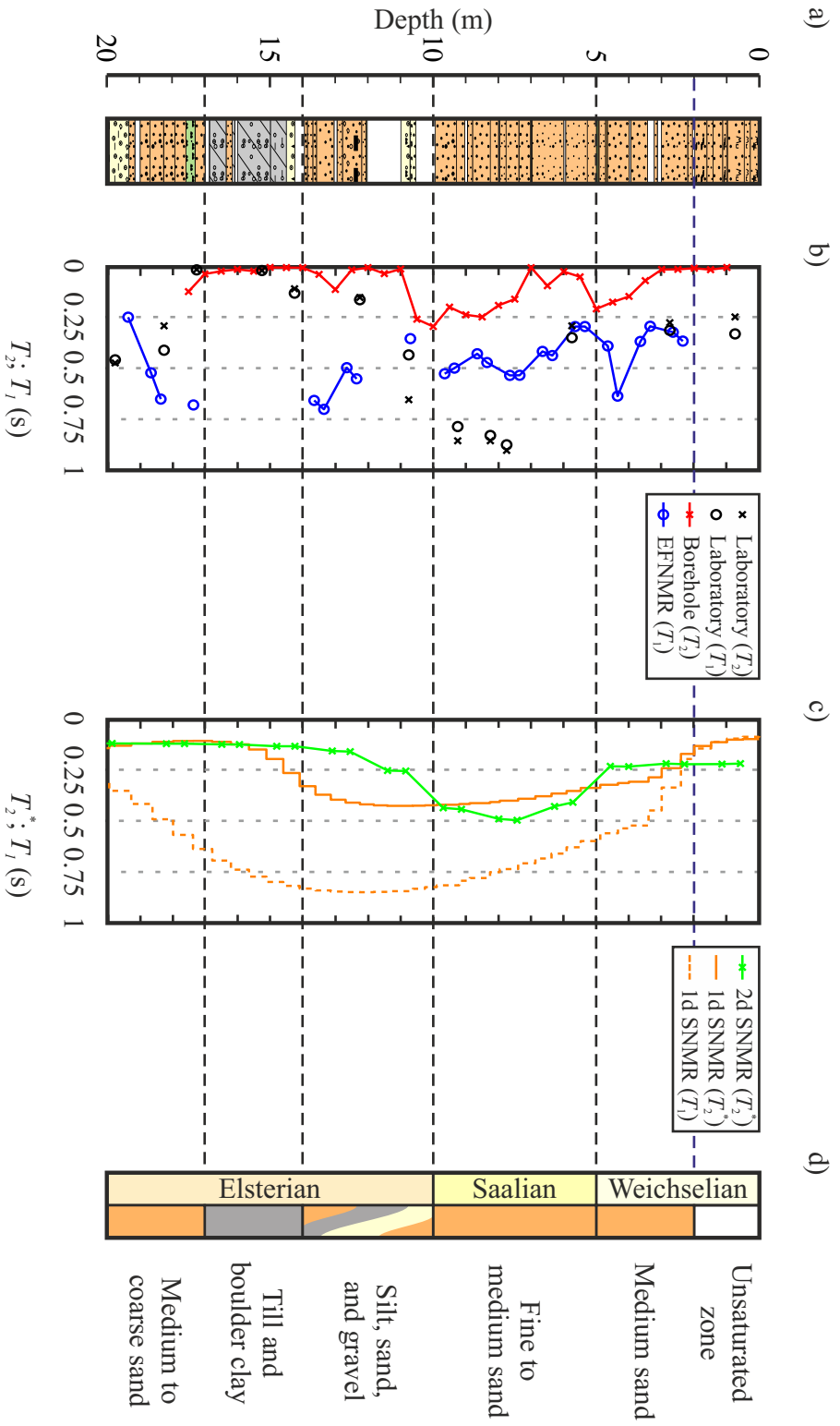


Figure 6.11.: Lithology profile (a) and conceptual model (d) of the Eng20 drilling (see Fig. 6.3). Comparison of  $T_1$  from methods with similar depth resolution.  $T_1$  and  $T_2$  times obtained using laboratory, borehole and Earth's field NMR measurements.  $T_1$  and  $T_2^*$  times obtained from surface NMR surveys.

surface NMR can resolve the overall trend in  $T$  but struggles to resolve variations of  $T$  originating from fine layers or occurring at larger depth. The most noticeable deviation between the  $T_2$  results obtained from the 1D and 2D surface NMR survey can be observed at a depth between 10 to 14 m. But it is difficult to evaluate which result should be preferred over the other because there are arguments for both. The decreasing  $T_2$  times of the 2D survey is supported by laboratory and borehole NMR measurements and is consistent with the expectation of shorter  $T$  times due to an increased clay content. On the other hand, the data set of the 1D survey has a better signal quality and larger  $q$  range and the increasing  $T$  values are supported by Earth's field NMR measurements.

### Estimation of $T$

There are different ways to merge the information of a measured NMR signal into one specific  $T$  value. Dependent on the signal-to-noise ratio and  $t_{\text{dteff}}$  of the method, the maximum of the fitted relaxation-time distribution was used for laboratory and borehole NMR and a monoexponential data fit was used for Earth's field and surface NMR measurements. The objective was to explain the measured data within the noise level using the simplest model. A detailed discussion about why the maximum of the  $T$  distribution was preferred in this work to represent the pore-size information of samples can be found in Chapter 3.5.3 and 3.6.4.

### Larmor frequency

The Larmor frequency ( $\omega_0$ ) of the NMR methods used in this work span a range of three magnitudes, from laboratory NMR (2 MHz) over borehole NMR (245 kHz) to Earth's field and surface NMR (2 kHz). Because  $\omega_0$  is linear related to  $\mathbf{B}_0$  (Eq. 2.3) and thus  $\mathbf{M}_0$  (Eq. 2.2),  $\omega_0$  can be used as an indication for the maximum strength of the NMR signal obtained from a volume unit of water. Laboratory NMR features the highest  $\omega_0$  leading to the highest signal-to-noise ratio of the presented measurements  $> 600$  followed by borehole NMR which leads to a signal-to-noise ratio of up to  $\approx 10$ . To compensate for the low  $\mathbf{M}_0$ , Earth's field NMR utilises a trick to increase  $\mathbf{M}_0$  using a pre-polarisation pulse resulting in a signal-to-noise ratio of up to  $\approx 3$ . Surface NMR compensates for the low  $\mathbf{M}_0$  by integrating the NMR signal over a large volume which significantly increases the signal-to-noise ratio of a single experiment up to  $\approx 100$ . However, the ability to

## 6. The hydrogeophysical test site Schillerslage

resolve a water layer depends on an inversion of a set of NMR experiments which commonly leads to a decrease of resolution with depth.

The relaxation of a proton is affected by its mobility in the fluid and the electron spin relaxation (Godefroy et al., 2001b). This leads to a temperature and frequency dependency of the  $\rho$  and hence shorter measured  $T$  times for lower Larmor frequencies. After Godefroy et al. (2001b), the range of  $\omega_0$  used by the different NMR methods in this work theoretically affects  $T$  in sandy material by a factor of up to about 1.6 with longer  $T$  times for higher  $\omega_0$  values. For the presented data, a systematic shift of  $T$  dependent on  $\omega_0$  was not observed which indicates that other effects are more dominant.

### Calibration of the NMR water content

The amplitude of the NMR signal is linear correlated to the amount of water in a sample (Eq. 2.1). To estimate the NMR water content ( $w$ ), information about the sampled volume is necessary. For surface NMR, the volume sensitivity of each NMR experiment is calculated dependent on the propagation of the magnetic excitation fields and the spatial  $w$  distribution is estimated from the NMR signal amplitude using an inversion. For laboratory and Earth's field NMR measurements, the sampled volume is commonly known. Therefore, the linear correlation between NMR signal amplitude and  $w$  can be calibrated using a water sample of equal temperature. For the presented data, this calibration was repeated at least once per day. The calibration of the borehole tool requires more effort and can be achieved using a large water tank. Because a calibration tank was not available at the LIAG at the time of the survey, the calibration factor provided by the manufacturer was used. The noticeable and systematic deviation to higher  $w$  values estimated by borehole NMR in most parts of the Eng20 profile indicates that this calibration should be reviewed. However, because of modifications to the hardware of the probe a few days after the survey, a new calibration cannot be applied retrospectively to the presented data. Additionally, it should be noted that the calibration of the probe does not affect the estimate  $T_2$  times.

## 6.5. Prediction of $K$ from NMR measurements

### 6.5.1. 1D application using different NMR methods

To predict  $K$  from NMR measurements using KGM, information about the model parameters  $\rho_a$ ,  $\tau$  and  $T_B$  are necessary. A  $\tau$  of 1.5 was consistently assumed throughout this chapter. This is in agreement to the value of  $\tau$  discussed in Chapter 3 and used for the calculation of  $K_{KC}$  from sieving analyses (Chap. 6.2.3). For the laboratory samples,  $T_B$  was estimated from the extracted pore fluid of each sample. For all other NMR measurements which sample the pore water under in-situ conditions, water was extracted from a close by well and a mean  $T_B$  value of 2.1 s was estimated using Earth's field NMR.

The calibration of KGM is therefore reduced to the estimation of a representative  $\rho_a$  value. This is done exemplarily using the laboratory NMR measurements. Laboratory NMR was chosen because (i)  $T_B$  was estimated reliably on the laboratory samples, (ii) of the high quality of  $T_2$  and  $T_1$  and (iii) the material sampled by NMR and used to estimate  $K$  was identical. To estimate the best  $\rho_a$  which explains the  $K_{KC}$  values obtained from sieving analyses,  $\rho_a$  was varied between 30 and 300  $\mu\text{m s}^{-1}$ . The achieved RMS between the logarithmic of both  $K_{KC}$  and  $K_{KGM}$  are presented in Figure 6.12a. The till rich samples between 14 and 17 m are excluded from this analyses because of the limitations of Kozeny-Carman type equations to predict  $K$  in this material (Chap. 3.6.3). A  $\rho_a$  of approximately 100  $\mu\text{m s}^{-1}$  for  $T_1$  (Fig. 6.12b) and 130  $\mu\text{m s}^{-1}$  for  $T_2$  (Fig. 6.12c) leads to the lowest RMS and explains most observed variations of  $K$  in the sandy aquifers of the Schillerslage site within a quarter of a magnitude.

The values of  $\rho_a$  estimated for laboratory NMR measurements were transferred to predict  $K$  using all other NMR methods. The achieved  $K$  values obtained from  $T_2$  and  $T_2^*$  are summarised in Figure 6.13b. The figure shows that for the Schillerslage site, the calibration obtained from the laboratory NMR ( $T_2$ ) can be transferred to surface NMR ( $T_2^*$ ) leading to a sufficient prediction of  $K$  within half a magnitude. Larger deviations can be observed in the unsaturated zone above 2 m and below 14 m where the used surface NMR setups cannot resolve the thin layers of short  $T_2^*$  times.

The significantly shorter  $T_2$  times observed by borehole NMR compared to all other NMR methods, as discussed in Chapter 6.4.2, consequently lead to lower  $K$  values than expected. Reasonable variations of the KGM parameters can help to evaluate if the borehole NMR measurements are

6. The hydrogeophysical test site Schillerslage

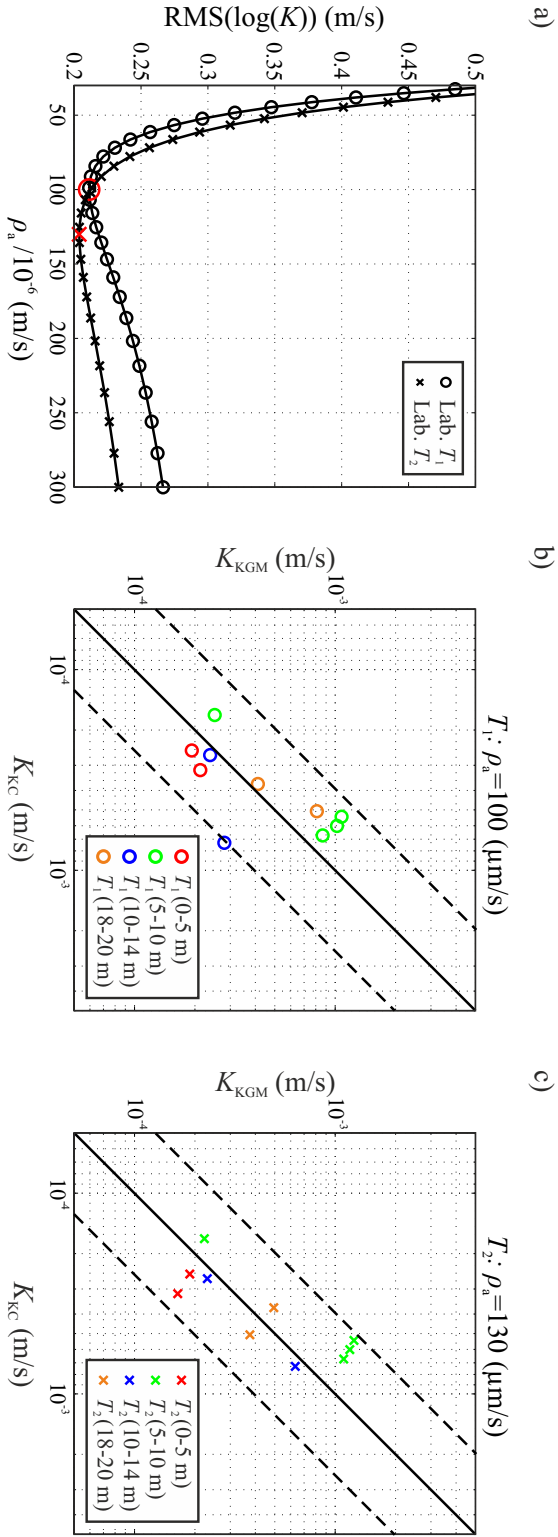


Figure 6.12.: Estimation of  $\rho_a$  for the Eng20 location by comparing  $K$  from sieving analyses on drill cores ( $K_{KC}$ ) and  $K$  from NMR using KGM ( $K_{KGM}$ ). (a) Obtained RMS of the logarithm of  $K_{KC}$  and  $K_{KGM}$  for a range of  $\rho_a$  from 30 to 300  $\mu\text{m s}^{-1}$  and  $T_1$  (circle) and  $T_2$  (cross) respectively. The models which achieve the lowest RMS for  $T_1$  and  $T_2$  are marked in red and presented in (b) ( $\rho_a = 100 \mu\text{m s}^{-1}$ ) and (c) ( $\rho_a = 130 \mu\text{m s}^{-1}$ ) respectively. The colours used in (b) and (c) mark samples from depth intervals with similar lithology. The continuous line marks identity and the dashed lines a deviation by a quarter of a magnitude.

### 6.5. Prediction of $K$ from NMR measurements

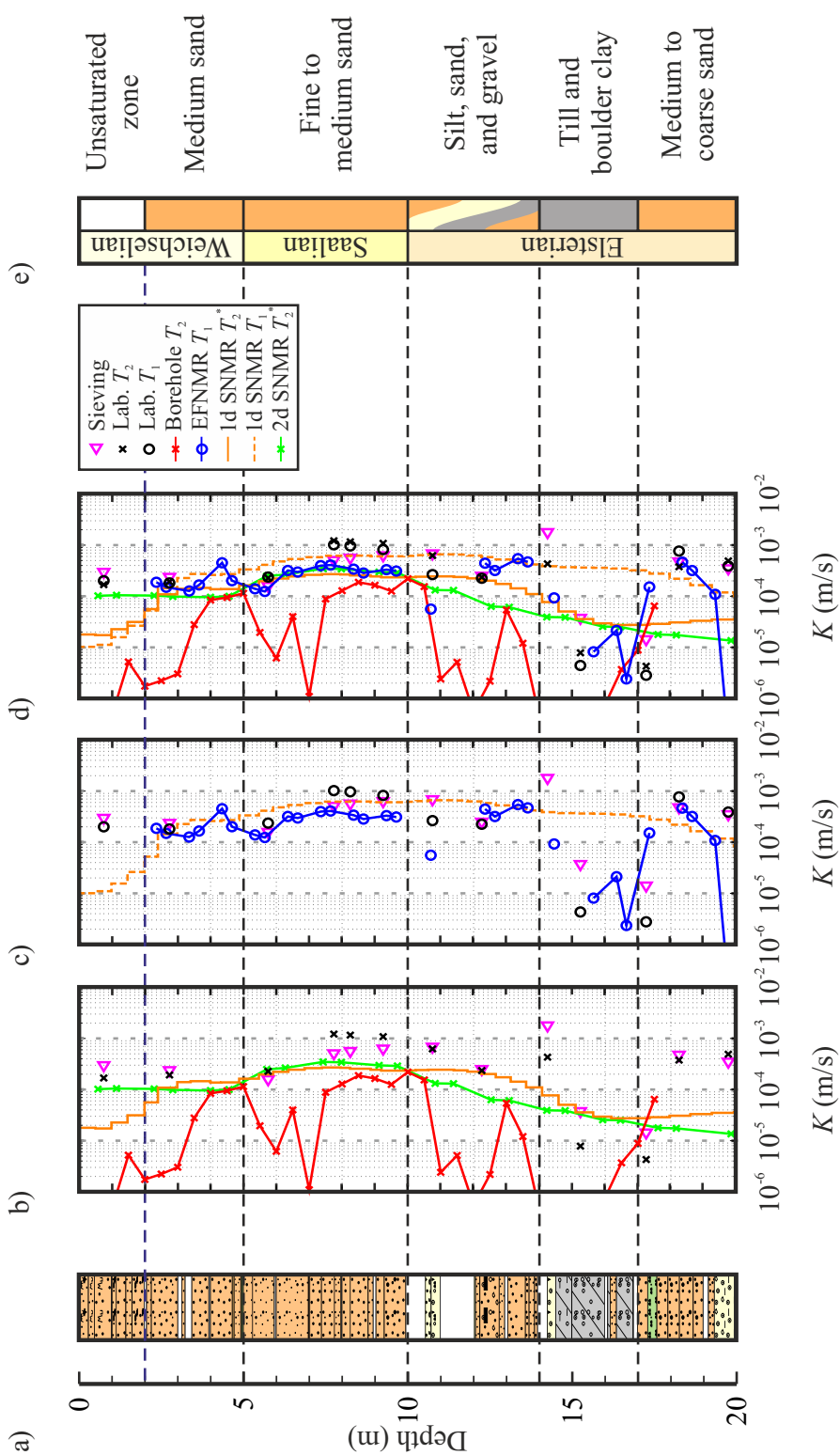


Figure 6.13.: Lithology profile (a) and conceptual model (e) of the Eng20 drilling (see Fig. 6.3).  $K$  derived from NMR measurements of  $\phi$  and the relaxation time  $T_2$  and  $T_1$  (b) and  $T_2^*$  and  $T_1^*$  (c) obtained using different methods. Summary of  $K$  obtained from all NMR methods (d).

## 6. The hydrogeophysical test site Schillerslage

affected by additional processes. The variability of  $\tau$  is limited and its impact on  $K$  is rather small. Additionally, assuming an equal  $\tau$  value for KGM and the Kozeny-Carman equation to predict  $K$  from sieving, a variation of  $\tau$  does not change the ratio of both  $K$  values at all. Increasing  $\rho_a$  leads to slightly higher  $K$  values predicted by KGM. But even for  $\rho_a = \infty$ , these  $K$  values do not reach the prediction achieved from sieving analyses. This ability of KGM to obtain a maximum  $K$  from a NMR measurement is described in Chapter 3.4.2. It is based on the slow-diffusion condition which limits the maximum  $T$  value which can be obtained from a given pore size and therefore  $K$ . This indicates that one of the relaxation processes,  $T_B$  of the in-situ water or the effect of  $T_D$ , are currently underestimated when interpreting the presented borehole NMR results. Recent diffusion measurements on free water indicates that  $\Delta\mathbf{B}_0$  and thus the impact of  $T_D$  is higher than provided by the manufacturer. More sophisticated studies are necessary to obtain the properties of the used borehole probe.

The  $K$  values obtained from KGM using  $T_1$  are summarised in Figure 6.13c. Similar to  $K$  predicted using  $T_2$ , most deviations from  $K$  obtained from sieving analyses are within half a magnitude. Larger deviations, e.g. in the till and boulder clay layer between 14 and 17 m, can be explained by the limitations of the surface NMR surveys or of Kozeny-Carman like equations which are not suited to predict  $K$  on till rich material.

A summary of all  $K$  values obtained from KGM using the same  $\rho_a$  values for all NMR methods are summarised in Figure 6.13d. While most visible effects were discussed earlier, the figure summarises that, for the Schillerslage site and considering the discussed limitations,  $T_2$ ,  $T_2^*$  and  $T_1$  can equally lead to a reliable prediction of  $K$  within half a magnitude.

### 6.5.2. 2D application using surface NMR

After the calibration of KGM based on the 1D variations of  $K$  at Eng20, the estimated value of  $\rho_a = 130 \mu\text{m s}^{-1}$  and the result of the 2D surface NMR survey (Fig. 6.7) presented in Chapter 6.3.2 can be merged to a 2D image of  $K$  in the subsurface (Fig. 6.14). Similar to results for  $w$  and  $T_2^*$ , the spatial variations of  $K$  can be explained by a simple three layer model. The first layer, with  $K$  values of about  $1 \times 10^{-4} \text{ m s}^{-1}$  matches the distribution of medium sand from the Weichselian glacial in the top 5 m of the subsurface. The pattern of lower  $K$  values in parts of this layer might be the consequence of the unsaturated zone not resolved by the QTI result. The spatial distribution of the second layer with consistent  $K$  of about  $1 \times 10^{-3} \text{ m s}^{-1}$  is in good agreement with the well sorted fine to

6.5. Prediction of  $K$  from NMR measurements

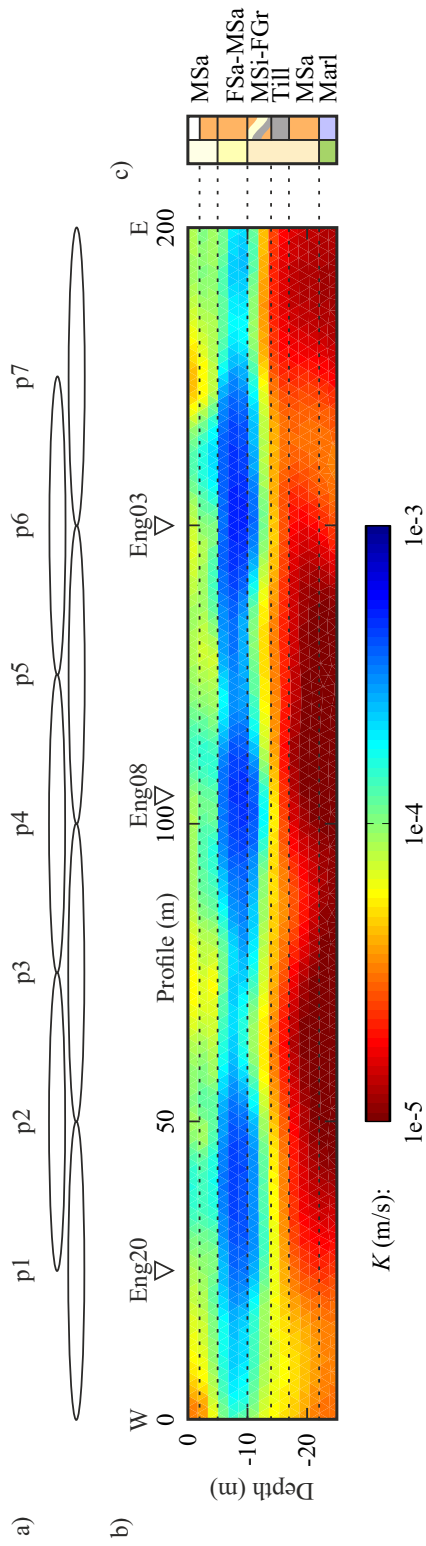


Figure 6.14.: Loop layout (a) and 2D result of  $K$  based on the KGM and 2D QTI result of the surface NMR survey presented in 6.7. (c) conceptual 1D model of the lithology obtained from drilling (see Fig. 6.3).

## 6. The hydrogeophysical test site Schillerslage

medium sands of the Saalian complex. The boundary to the sediments of the Elsterian glacial below 11 m is not well resolved. The medium sands and gravel on top still show  $K$  values of about  $5 \times 10^{-5} \text{ m s}^{-1}$  which can reach up to  $1 \times 10^{-5} \text{ m s}^{-1}$  in parts of the profile below 14 m. The lower aquifer consisting of medium to coarse sands is not resolved by the QTI result. Because the lateral pattern in  $K$  does not correlate with electrical resistivity anomalies from the ERT survey it is difficult to evaluate if they represent real 2D structures in the subsurface or are the result of the limitations of the survey as described in Chapter 6.3.2.

### 6.6. Summary of the Schillerslage study

The studies conducted at the Schillerslage site can be summarised as follows. The results obtained from drilling (Chap. 6.2.2), ERT and 2D surface NMR (Chap. 6.3) indicate that the site shows no larger 2D structures.

All applied NMR methods (Chap. 6.2.4) have their specific advantages and disadvantages which need to be considered to obtain a consistent image of the subsurface (Chap. 6.4.4). Therefore, a long  $t_{\text{deff}}$  time can lead to lower  $w$  values and longer  $T$  times, e.g. observed in the boulder clay. If the depth resolution of the method is high enough to resolve a single lithological unit, most observed NMR signals can be sufficiently explained by a monoexponential decay or the maximum of the  $T$  distribution. The observed variations of  $T_B$  on the re-saturated laboratory samples range from 0.1 to 2.48 s and thus can significantly affect the interpretation of  $T$ . The  $T_2$  times estimated by borehole NMR are significantly shorter than  $T$  obtained from other methods. The hence estimated  $K$  values from KGM are too low even for reasonable variations of the KGM parameters. This indicates that the impact of  $T_D$  on the measurements of the used borehole probe, i.e. the value of  $\Delta \mathbf{B}_0$ , needs to be reviewed. The exceptional high  $w$  values estimated by borehole NMR indicate that the equipment needs to be recalibrated. The dephasing of the NMR signals observed by surface NMR is not significant at the Schillerslage site and thus  $T_2^*$  yields valuable pore-size information.

To predict  $K$  using KGM, the obtained  $\rho_a$  from laboratory NMR and sieving analyses is approximately  $100 \mu\text{m s}^{-1}$  for  $T_1$  and  $130 \mu\text{m s}^{-1}$  for  $T_2$  respectively (Chap. 6.5.1). The thus calibrated KGM can be transferred to predict  $K$  using  $w$  and  $T$  obtained from other NMR methods. In combination with the 2D QTI result, this can lead to a 2D image of  $K$  in the subsurface (Chap. 6.5.2).

## 7. Summary and Outlook

A new model, called Kozeny-Godefroy model (KGM), has been presented and evaluated for predicting hydraulic conductivity ( $K$ ) from nuclear magnetic resonance (NMR) measurements on unconsolidated material (Chap. 3). Compared to the Schlumberger-Doll Research and SeEVERS equation, KGM allows for improved prediction of  $K$  for coarse-grained material by including the diffusion-limited case and bulk water relaxation. Replacing the empirical calibration factors with structural, physical and NMR intrinsic parameters focus the calibration of KGM using flow measurements on the matrix-specific parameters of the sample and therefore increase the range of validity. The application of KGM is limited to (i) materials with a small range of pore sizes and (ii) simple pore geometries like tube-shaped, planar or spherical pores.

The 2D  $qt$  inversion (QTI) approach (Chap. 5) is a valuable tool to image water content ( $w$ ) and the NMR relaxation time ( $T_2^*$ ) in the subsurface using surface NMR. The native implementation of data error and model regularisation into QTI leads to a simplified and stable inversion and improved results compared to the time-step inversion. The most significant improvements are the reduced amount of artifacts in the obtained spatial  $w$  and  $T_2^*$  distributions and the ability to implement additional structural information using spatial regularisation. Because  $T_2^*$  can yield valuable lithological, pore-size and  $K$  information, imaging both NMR parameters,  $w$  and  $T_2^*$ , allows for enhanced subsurface characterisation. An appropriate implementation of the electrical subsurface resistivity avoids the dislocation of structures and artifacts of low  $w$  values tracing regions of low electrical resistivity.

An extensive study to characterise the shallow aquifers was conducted at the hydrological test site Schillerslage (Chap. 6). This study consists of several geoscientific and geophysical surveys including different NMR methods. The obtained NMR parameters show method specific properties which need to be considered to obtain a consistent image of the subsurface. Most remarkable are the impact of effective dead time, bulk water relaxation, and the size and condition of the sampled volume. After the calibration of KGM using laboratory NMR measurements and sieving analyses, the obtained parameters were transferred to predict  $K$  using other NMR methods. In combination with the 2D QTI result, this leads to a 2D image of the spatial

## 7. Summary and Outlook

$K$  distribution in the subsurface.

This thesis tackles some of the demanding questions when characterising shallow aquifers using NMR. But it is the nature of research to raise new questions. The main factor which limits the range of application for KGM are the constraints applied to pore geometry and pore-size distribution. Therefore, the performance of KGM to predict  $K$  on material which violates basic assumptions, e.g. shows a range of pore sizes, should be reviewed. The prediction of  $K$  on samples which were not calibrated by flow measurements on similar material might be improved by (i) extensive laboratory measurements on different geological materials to estimate the natural range of apparent surface relaxivity variations and (ii) exploiting the information about pore-radius and apparent surface relaxivity contained in the relaxation-time distribution of diffusion controlled samples. Additionally, the natural variations of  $T_B$  under different lithologies and fluid chemistries should be studied to improve the prediction of  $K$  from NMR measurements which lack a separate fluid sampling, e.g. borehole and surface NMR.

The range of application for the presented 2D QTI approach can be increased by (i) a sensitivity kernel calculation which fully supports a 2D electrical resistivity distribution, (ii) including capability for transverse or longitudinal relaxation times and (iii) an target specific adaptation of the model space. For non-resistive targets, e.g. clay or salt water, accounting for the real 2D distribution of electrical resistivities in the subsurface during the calculation of  $\mathbf{G}$  is crucial to avoid artifacts in the inversion results. Targets which show significant magnetic susceptibilities benefit from  $T_1$  or  $T_2$  experiments because  $T_2^*$  can lose pore size and thus  $K$  information due to internal magnetic gradients on the pore scale. Dependent on the target, the selection of another model space, e.g. stretched-exponential  $T_2^*$  for regions with an interbedding of fine and coarse layers, might lead to better results. Using the complete and naturally complex NMR signal for the inversion instead of reducing the signal to its amplitude will simplify the processing of NMR data and improve the resolution of the 2D QTI approach. The consequent increment of QTI from 2D to 3D applications is currently limited by the size of the inverse problem. This can be solved by further size optimisations or, in the near future, will be solved automatically by the rapid progress in the performance of personal computers.

## 8. Acknowledgements

Many people supported me on my long way to finish this thesis. I can only thank a few of them here and I apologise to those I am not mentioning.

Prof. Dr. Ugur Yaramanci for pushing the hydrogeophysical application of NMR since decades. His support not only allowed me to finish this thesis but, over the years, developed a small and supportive working group at the Technical University of Berlin and the LIAG.

Prof. Dr. Esben Auken who agreed to review this thesis despite his full schedule.

Dr. Mike Müller-Petke for his support and countless discussions which were a beacon through the deep waters of NMR. It was a lot of fun! Today I know that I have hardly scratched the surface of this ocean am I am looking forward to explore more.

Dr. Thomas Günther for supporting me with his next to boundless knowledge of inverting geoscientific data. His input, point of view and several last minute feedbacks improved a lot of my publications.

Mathias Ronczka and Dr. Jan Igel for all the scientific discussions beyond the scope of NMR and their help in solving everyday problems. Good luck for your thesis Matze!

Robert Meyer, Wolfgang Südekum, Thomas Grelle, Jan-Thorsten Blanke, Dr. Christian Rolf and the drilling crew of the State Authority for Mining, Energy and Geology for their support during field and laboratory measurements.

Dr. Marion Miensopust, Martin Lyssenko and Dr. Tobias Stacke for their persistent proof reading.

Last but not least, I want to thank my family and friends for their unlimited support.



# Bibliography

- Akbar, M., M. Petricola, and M. Watfa (1995). Classic Interpretation Problems: Evaluating Carbonates. *Oilfield Review* 7(1), pp. 38–57 (cit. on p. 2).
- Bartell, F. E. and H. J. Osterhof (1928). The Pore Size of Compressed Carbon and Silica Membranes. *The Journal of Physical Chemistry* 32(10), pp. 1553–1571. DOI: 10.1021/j150292a012 (cit. on p. 18).
- Behroozmand, A. A., E. Auken, G. Fiandaca, A. V. Christiansen, and N. B. Christensen (2012). Efficient full decay inversion of MRS data with a stretched-exponential approximation of the distribution. *Geophysical Journal International* 190(2), pp. 900–912. ISSN: 1365-246X. DOI: 10.1111/j.1365-246X.2012.05558.x (cit. on pp. 41, 44).
- Binot, F. (2008). Vier neue Bohrungen im Mess- und Testgebiet des GGA-Instituts nördlich von Schillerslage bei Burgdorf, Niedersachsen. GGA-Bericht. Archiv Nr.: 0 128 085. GGA-Institut, Stilleweg 2, D-30655 Hannover (cit. on pp. 68–70).
- Bloch, F. (1946). Nuclear Induction. *Physical Review* 70(7–8), pp. 460–474. DOI: 10.1103/PhysRev.70.460 (cit. on p. 8).
- Bloch, F., W. W. Hansen, and M. Packard (1946). The Nuclear Induction Experiment. *Physical Review* 70(7-8), pp. 474–485. DOI: 10.1103/PhysRev.70.474 (cit. on p. 1).
- Braun, M. (2007). Influence of the resistivity on Magnetic Resonance Sounding: 1D inversion and 2D modelling. PhD thesis. TU Berlin: Technical University of Berlin (cit. on p. 58).
- Braun, M., M. Hertrich, and U. Yaramanci (2005). Study on complex inversion of magnetic resonance sounding signals. *Near Surface Geophysics* 3(3), pp. 155–163. DOI: 10.3997/1873-0604.2005011 (cit. on pp. 36, 65).
- Braun, M. and U. Yaramanci (2008). Inversion of resistivity in Magnetic Resonance Sounding. *Journal of Applied Geophysics* 66(3–4), pp. 151–164. ISSN: 0926-9851. DOI: 10.1016/j.jappgeo.2007.12.004 (cit. on pp. 34, 53, 54).
- Brown, R. J. S. and B. W. Gamson (1960). Nuclear magnetism logging. *Journal of Petroleum Technology* 219 pp. 199–201 (cit. on p. 1).
- Brown, R. J. S. and P. Fantazzini (1993). Conditions for initial quasilinear  $T_2^{-1}$  versus  $\tau$  for the Carr-Purcell-Meiboom-Gill NMR with diffusion and

## Bibliography

- susceptibility differences in porous media and tissues. *Physical Review B* 47 (22), pp. 14823–14834. DOI: 10.1103/PhysRevB.47.14823 (cit. on p. 13).
- Brownstein, K. R. and C. E. Tarr (1979). Importance of classical diffusion in NMR studies of water in biological cells. *Physical Review A* 19(6), pp. 2446–2453. DOI: 10.1103/PhysRevA.19.2446 (cit. on pp. 1, 2, 12–14, 22, 29).
- Callaghan, P. T. and M. Le Gros (1982). Nuclear spins in the Earth’s magnetic field. *American Journal of Physics* 50(8), pp. 709–713. DOI: 10.1119/1.12735 (cit. on p. 74).
- Carman, P. C. (1938). The determination of the specific surface of powders. *Journal of the Society of Chemical Industrialists* 57 pp. 225–234 (cit. on pp. 1, 11).
- (1956). Flow of gases through porous media. Ed. by P. C. Carman. London: Academic Press (cit. on p. 18).
- Carr, H. Y. and E. M. Purcell (1954). Effects of Diffusion on Free Precession in Nuclear Magnetic Resonance Experiments. *Physical Review* 94(3), pp. 630–638. DOI: 10.1103/PhysRev.94.630 (cit. on p. 10).
- Carrier, W. D. (2003). Goodbye, Hazen; Hello, Kozeny-Carman. *Journal of Geotechnical and Geoenvironmental Engineering* 129(11), pp. 1054–1056. DOI: 10.1061/(ASCE)1090-0241(2003)129:11(1054) (cit. on pp. 1, 11, 21, 27).
- Coates, G. R., L. Xiao, and M. G. Prammer (1999). NMR Logging Principles and Application. Huston: Halliburton Energy Services (cit. on p. 92).
- Coates, G. R. and J. L. Dumanoir (1973). A new approach to improved log-derived permeability. In: *SPWLA 14th Annual Logging Symposium*, p. 28 (cit. on p. 15).
- Coscia, I., S. Greenhalg, N. Linde, J. Doetsch, L. Marescot, T. Günther, and A. Green (2011). 3D crosshole apparent resistivity static inversion and monitoring of a coupled river-aquifer system. *Geophysics* 76(2), G49–G59. DOI: 10.1190/1.3553003 (cit. on pp. 38, 47, 53).
- Dlugosch, R., M. Mueller-Petke, T. Guenther, S. Costabel, and U. Yaramanci (2011). Assessment of the potential of a new generation of surface NMR instruments. *Near Surface Geophysics* 9(2), pp. 89–102. DOI: 10.3997/1873-0604.2010063 (cit. on pp. 3, 36, 48, 58, 64, 73, 92).
- Dlugosch, R., T. Günther, M. Müller-Petke, and U. Yaramanci (2013). Improved prediction of hydraulic conductivity for coarse-grained, unconsolidated material from nuclear magnetic resonance. *Geophysics* 78(4), EN55–EN64. DOI: 10.1190/geo2012-0187.1 (cit. on pp. 3, 11).

- (2014). Two-dimensional distribution of relaxation time and water content from surface nuclear magnetic resonance. *Near Surface Geophysics* 12 pp. 231–241. DOI: 10.3997/1873-0604.2013062 (cit. on pp. 4, 43).
- Dunn, K. J., D. J. Bergman, and G. A. Latorraca (2002). Nuclear magnetic resonance, Petrophysical and Logging Applications. Ed. by K. Helbig and S. Treitel. 1. Pergamon (cit. on pp. 13, 18).
- Foley, I., S. A. Farooqui, and R. L. Kleinberg (1996). Effect of Paramagnetic Ions on NMR Relaxation of Fluids at Solid Surfaces. *Journal of Magnetic Resonance Series A* 123(1), pp. 95–104. ISSN: 1064-1858. DOI: 10.1006/jmra.1996.0218 (cit. on p. 29).
- Fukushima, E. and S. B. W. Roeder (1981). Experimental Pulse NMR - A Nuts and Bolts Approach. Westview Press (cit. on p. 38).
- Girard, J. F., M. Boucher, A. Legchenko, and J. M. Baltassat (2007). 2D magnetic resonance tomography applied to karstic conduit imaging. *Journal of Applied Geophysics* 63(3-4), pp. 103–116. ISSN: 0926-9851. DOI: 10.1016/j.jappgeo.2007.08.001 (cit. on pp. 3, 38).
- Godefroy, S., M. Fleury, F. Deflandre, and J. P. Korb (2001a). Temperature effect on NMR surface relaxation. In: *SPE Annual Technical Conference and Exhibition, 30 September-3 October 2001, New Orleans, Louisiana*, p. 13. DOI: 10.2118/71700-MS (cit. on p. 22).
- Godefroy, S., J. P. Korb, M. Fleury, and R. G. Bryant (2001b). Surface nuclear magnetic relaxation and dynamics of water and oil in macroporous media. *Physical Review E* 64(2), p. 13. ISSN: 1063-651X. DOI: 10.1103/PhysRevE.64.021605 (cit. on pp. 13, 24, 29, 96, 115).
- Grunewald, E. and R. Knight (2011a). The effect of pore size and magnetic susceptibility on the surface NMR relaxation parameter  $T_2^*$ . *Near Surface Geophysics* 9(2), pp. 169–178. DOI: 10.3997/1873-0604.2010062 (cit. on p. 89).
- Grunewald, E. and R. Knight (2011b). A laboratory study of NMR relaxation times in unconsolidated heterogeneous sediments. *Geophysics* 76(4), G73–G83. DOI: 10.1190/1.3581094 (cit. on p. 29).
- Günther, T. and M. Müller-Petke (2012). Hydraulic properties at the North Sea island of Borkum derived from joint inversion of magnetic resonance and electrical resistivity soundings. *Hydrology and Earth System Sciences* 16 pp. 3279–3291. DOI: doi : 10.5194/hess-16-3279-2012 (cit. on pp. 41, 43, 44, 55).
- Günther, T., C. Rücker, and K. Spitzer (2006). Three-dimensional modeling and inversion of dc resistivity data incorporating topography – Part II: Inversion. *Geophysical Journal International* 166(2), pp. 506–517. DOI: 10.1111/j.1365-246X.2006.03011.x (cit. on pp. 37, 38, 76).

## Bibliography

- Hertrich, M., M. Braun, T. Günther, A. G. Green, and U. Yaramanci (2007). Surface Nuclear Magnetic Resonance Tomography. *IEEE Transactions On Geoscience And Remote Sensing* 45(11), pp. 3752–3759. DOI: 10.1109/TGRS.2007.903829 (cit. on pp. 3, 37, 38, 44).
- Hertrich, M., M. Braun, and U. Yaramanci (2005). Magnetic resonance soundings with separated transmitter and receiver loops. *Near Surface Geophysics* 3(3), pp. 141–154. DOI: 10.3997/1873-0604.2005010 (cit. on p. 3).
- Hertrich, M., A. G. Green, M. Braun, and U. Yaramanci (2009). High-resolution surface-NMR tomography of shallow aquifers based on multi-offset measurements. *Geophysics* 74(6), G47–G59. DOI: 10.1190/1.3258342 (cit. on pp. 3, 38, 55–61).
- Hertrich, M. (2008). Imaging of groundwater with nuclear magnetic resonance. *Progress in Nuclear Magnetic Resonance Spectroscopy* 53(4), pp. 227–248. ISSN: 0079-6565. DOI: 10.1016/j.pnmrs.2008.01.002 (cit. on p. 31).
- Holland, R., R. Dlugosch, T. Günther, S. Sass, J. Holzhauer, J. Sauer, F. Binot, and U. Yaramanci (2011). Das hydrogeophysikalische Testfeld Schillerslage. *Deutsche Geophysikalische Gesellschaft e.V. Mitteilungen* 2011(1), pp. 51–54. ISSN: 1064-1858 (cit. on p. 67).
- Howard, J. J., W. E. Kenyon, and C. Straley (1993). Proton Magnetic Resonance and Pore Size Variations in Reservoir Sandstones. *SPE Formation Evaluation* 8(3), pp. 194–200. DOI: 10.2118/20600-PA (cit. on p. 26).
- Hürlimann, M. D., K. G. Helmer, L. L. Latour, and C. H. Sotak (1994). Restricted Diffusion in Sedimentary Rocks. Determination of Surface-Area-to-Volume Ratio and Surface Relaxivity. *Journal of Magnetic Resonance, Series A* 111(2), pp. 169–178. ISSN: 1064-1858. DOI: 10.1006/jmra.1994.1243 (cit. on pp. 14, 26).
- James, R. A. and R. Ehrlich (1999). Core-Based Investigation of NMR Logging as a Tool for Characterization of Shallow Unconsolidated Aquifers. *Ground Water* 37(1), pp. 48–57. ISSN: 1745-6584. DOI: 10.1111/j.1745-6584.1999.tb00957.x (cit. on p. 65).
- Josh, M., L. Esteban, C. D. Piane, J. Sarout, D. N. Dewhurst, and M. B. Clennell (2012). Laboratory characterisation of shale properties. *Journal of Petroleum Science and Engineering* 88–89 pp. 107–124. ISSN: 0920-4105. DOI: 10.1016/j.petro.2012.01.023 (cit. on p. 1).
- Keating, K. and R. Knight (2007). A laboratory study to determine the effect of iron oxides on proton NMR measurements. *Geophysics* 72(1), E27–E32. DOI: 10.1190/1.2399445 (cit. on p. 57).

- Kenyon, W. E. (1997). Petrophysical Principles of Applications of NMR Logging. *The Log Analyst* 38(2), pp. 21–43 (cit. on pp. 1, 14, 57).
- Kenyon, W. E., P. I. Day, C. Straley, and J. F. Willemsen (1988). A Three-Part Study of NMR Longitudinal Relaxation Properties of Water-Saturated Sandstones. *SPE Formation Evaluation* 3(3), pp. 622–636. DOI: 10.2118/15643-PA (cit. on pp. 1, 2, 14, 15, 29).
- Kenyon, W. E., J. J. Howard, A. Sezginer, C. Straley, A. Matteson, K. Horkowitz, and R. Ehrlich (1989). Pore-size Distribution and NMR in Microporous Cherty Sandstones. In: *Proceedings of the 40th Annual Logging Symposium*, p. 24 (cit. on pp. 14, 26).
- Kestin, J., M. Sokolov, and W. A. Wakeham (1978). Viscosity of liquid water in the range -8 °C to 150 °C. *Journal of Physical and Chemical Reference Data* 7(3), pp. 941–948. DOI: 10.1063/1.555581 (cit. on p. 18).
- Kleinberg, R. L., S. A. Farooqui, and M. A. Horsfield (1993). T1/T2 Ratio and Frequency Dependence of NMR Relaxation in Porous Sedimentary Rocks. *Journal of Colloid and Interface Science* 158(1), pp. 195–198. ISSN: 0021-9797. DOI: 10.1006/jcis.1993.1247 (cit. on pp. 9, 14).
- Kleinberg, R. L., C. Flaum, C. Straley, P. G. Brewer, G. E. Malby, E. T. Peltzer III, G. Friederich, and J. P. Yesinowski (2003). Seafloor nuclear magnetic resonance assay of methane hydrate in sediment and rock. *Journal of Geophysical Research* 108(B3), p. 13. DOI: doi:10.1029/2001JB000919 (cit. on p. 2).
- Kleinberg, R. L. and M. A. Horsfield (1990). Transverse relaxation processes in porous sedimentary rock. *Journal of Magnetic Resonance (1969)* 88(1), pp. 9–19. ISSN: 0022-2364. DOI: 10.1016/0022-2364(90)90104-H (cit. on pp. 10, 13).
- Kozeny, J. (1927). Über kapillare Leitung des Wassers im Boden. *Sitzungsberichte / Akademie der Wissenschaften in Wien, Mathematisch-Naturwissenschaftliche Klasse Abteilung IIa* 136 pp. 271–306 (cit. on pp. 1, 11).
- Lanfrey, P. Y., Z. V. Kuzeljevic, and M. P. Dudukovic (2010). Tortuosity model for fixed beds randomly packed with identical particles. *Chemical Engineering Science* 65(5), pp. 1891–1896. ISSN: 0009-2509. DOI: 10.1016/j.ces.2009.11.011 (cit. on p. 23).
- LaTorraca, G. A., K. J. Dunn, and R. J. S. Brown (1993). Predicting permeability from nuclear magnetic resonance and electrical properties measurements. In: *1993 Society of Core Analysts Conference*, pp. paper. 9312 pp. 1–12 (cit. on p. 13).
- Legchenko, A. and O. A. Shushakov (1998). Inversion of surface NMR data. *Geophysics* 63(1), pp. 75–84. DOI: 10.1190/1.1444329 (cit. on pp. 2, 38).

## Bibliography

- Legchenko, A. and P. Valla (2002). A review of the basic principles for proton magnetic resonance sounding measurements. *Journal of Applied Geophysics* 50(1-2), pp. 3–19. ISSN: 0926-9851. DOI: 10.1016/S0926-9851(02)00127-1 (cit. on pp. 2, 40).
- Lehmann-Horn, J. A., M. Hertrich, S. A. Greenhalgh, and A. G. Green (2011). Three-Dimensional Magnetic Field and NMR Sensitivity Computations Incorporating Conductivity Anomalies and Variable-Surface Topography. *IEEE Transactions on Geoscience and Remote Sensing* 49(10), pp. 3878–3891. DOI: 10.1109/TGRS.2011.2135861 (cit. on p. 32).
- Levitt, M. H. (2002). Spin Dynamics - Basics of Nuclear Magnetic Resonance. John Wiley & Sons, LTD (cit. on pp. 5, 6).
- Mavko, G. and A. Nur (1997). The effect of a percolation threshold in the Kozeny-Carman relation. *Geophysics* 62(5), pp. 1480–1482. DOI: 10.1190/1.1444251 (cit. on p. 15).
- McCutcheon, S. C., J. L. Martin, and T. O. J. Barnwell (1993). Handbook of Hydrology. In: ed. by D. R. Maidment. McGraw-Hill, New York. Chap. 11, pp. 11.1–11.69 (cit. on p. 18).
- Meiboom, S. and D. Gill (1958). Modified Spin-Echo Method for Measuring Nuclear Relaxation Times. *Review of Scientific Instruments* 29(8), p. 688. DOI: 10.1063/1.1716296 (cit. on p. 10).
- Mohnke, O. and U. Yaramanci (2008). Pore size distributions and hydraulic conductivities of rocks derived from Magnetic Resonance Sounding relaxation data using multi-exponential decay time inversion. *Journal of Applied Geophysics* 66(3-4), pp. 73–81. ISSN: 0926-9851. DOI: 10.1016/j.jappgeo.2008.05.002 (cit. on pp. 15, 36).
- Mueller-Petke, M. and U. Yaramanci (2010). QT inversion — Comprehensive use of the complete surface NMR data set. *Geophysics* 75(4), WA199–WA209. DOI: 10.1190/1.3471523 (cit. on pp. 2, 36, 38, 41, 43, 47, 64, 65, 93, 117, 118).
- Müller-Petke, M. (2009). Extended use of Magnetic Resonance Sounding datasets - QT inversion and resolution studies. PhD thesis. Berlin University of Technology (cit. on pp. 56, 57, 62, 63, 92, 93).
- Müller-Petke, M., J. O. Walbrecker, and R. J. Knight (2013). The inversion of surface-NMR T1 data for improved aquifer characterization. *Geophysics* 78 EN83–EN94. DOI: 10.1190/GE02013-0035.1 (cit. on pp. 74, 93).
- Nocedal, J. and S. Wright (2006). Numerical Optimization. Ed. by T. Mikosch, S. Robinson, and S. Resnick. 2nd. XXII Springer Series in Operations Research and Financial Engineering. Springer Verlag, p. 664 (cit. on p. 38).

- Pape, H., J. E. Tillich, and M. Holz (2006). Pore geometry of sandstone derived from pulsed field gradient NMR. *Journal of Applied Geophysics* 58(3), pp. 232–252. ISSN: 0926-9851. DOI: 10.1016/j.jappgeo.2005.07.002 (cit. on pp. 11, 18).
- Persson, P. O. and G. Strang (2004). A Simple Mesh Generator in MATLAB. *SIAM Review* 46(2), pp. 329–345. DOI: 10.1137/S0036144503429121 (cit. on p. 45).
- Purcell, E. M., H. C. Torrey, and R. V. Pound (1946). Resonance Absorption by Nuclear Magnetic Moments in a Solid. *Physical Review* 69(1–2), pp. 37–38. DOI: 10.1103/PhysRev.69.37 (cit. on p. 1).
- Ramakrishnan, T. S., L. M. Schwartz, E. J. Fordham, W. E. Kenyon, and D. J. Wilkinson (1999). Forward Models for Nuclear Magnetic Resonance in Carbonate Rocks. *The Log Analyst* 40(4), pp. 260–270 (cit. on pp. 29, 65).
- Roncza, M., Müller-Petke, R. M. Dlugosch, and T. Günther (2012). A physics-driven approach using Single-Pore-Modes (SPM) for estimating an average pore radius and surface relaxivity from NMR data. In: *Proceedings of 25th international SAGEEP conference*. Tucson, Arizona, p. 5 (cit. on p. 22).
- Sass, S. (2010). Applicability of geophysical measuring methods for determination of K values in comparison to conventional methods. Diploma thesis. Leibniz University Hannover (cit. on p. 71).
- Seevers, D. O. (1966). A nuclear magnetic method for determining the permeability of sandstones. In: *SPWLA 7th Annual Logging Symposium*. Paper L Tulsa, Oklahoma, p. 14 (cit. on pp. 1, 2, 12, 14, 29).
- Semenov, A. G. (1987). NMR hydroscope for water prospecting. In: *Proceedings of the Seminar on Geotomography*, pp. 66–67 (cit. on p. 1).
- Straley, C., A. Matteson, S. Feng, L. M. Schwartz, W. E. Kenyon, and J. R. Banavar (1987). Magnetic resonance, digital image analysis, and permeability of porous media. *Applied Physics Letters* 51(15), pp. 1146–1148. DOI: 10.1063/1.98766 (cit. on pp. 14, 26).
- Timur, A. (1968). An Investigation Of Permeability, Porosity, and Residual Water Saturation Relationships For Sandstone Reservoirs. *The Log Analyst* IX(4), pp. 8–17 (cit. on p. 15).
- Walbrecker, J. O., M. Hertrich, and A. G. Green (2009). Accounting for relaxation processes during the pulse in surface NMR data. *Geophysics* 74(6), G27–G34. DOI: 10.1190/1.3238366 (cit. on p. 36).
- (2011). Off-resonance effects in surface nuclear magnetic resonance. *Geophysics* 76(2), G1–G12. DOI: 10.1190/1.3535414 (cit. on pp. 36, 74).

## Bibliography

- Walsh, D. O., E. Grunewald, P. Turner, A. Hinnell, and P. Ferre (2011). Practical limitations and applications of short dead time surface NMR. *Near Surface Geophysics* 9(2), pp. 103–111. DOI: 10.3997/1873-0604.2010073 (cit. on p. 50).
- Walsh, D. O. (2008). Multi-channel surface NMR instrumentation and software for 1D/2D groundwater investigations. *Journal of Applied Geophysics* 66(3-4), pp. 140–150. ISSN: 0926-9851. DOI: 10.1016/j.jappgeo.2008.03.006 (cit. on pp. 3, 40).
- Ward, S. H. and G. W. Hohmann (1988). Electromagnetic Theory for Geophysical Applications. In: *Electromagnetic Methods in Applied Geophysics*. Ed. by M. N. Nabighian. Society of Exploration Geophysicists. Chap. 4, pp. 130–311. DOI: 10.1190/1.9781560802631.ch4 (cit. on pp. 32, 50).
- Weichman, P. B., E. M. Lively, and M. H. Ritzwoller (1999). Surface Nuclear Magnetic Resonance Imaging of Large Systems. *Physical Review Letters* 82(20), pp. 4102–4105. DOI: 10.1103/PhysRevLett.82.4102 (cit. on p. 1).
- (2000). Theory of surface nuclear magnetic resonance with applications to geophysical imaging problems. *Physical Review E* 62(1), pp. 1290–1312. DOI: 10.1103/PhysRevE.62.1290 (cit. on pp. 32, 36).
- Weichman, P. B., D. R. Lun, M. H. Ritzwoller, and E. M. Lively (2002). Study of surface nuclear magnetic resonance inverse problems. *Journal of Applied Geophysics* 50(1–2), pp. 129–147. ISSN: 0926-9851. DOI: 10.1016/S0926-9851(02)00135-0 (cit. on p. 65).
- Weidelt, P. (2005). Geoelektrik Grundlagen. In: *Handbuch zur Erkundung des Untergrundes von Deponien*. Ed. by K. Knödel, H. Krummel, and G. Lange. 3 Springer-Verlag, pp. 71–100 (cit. on p. 34).
- Whittall, K. P., M. J. Bronskill, and R. M. Henkelman (1991). Investigation of analysis techniques for complicated NMR relaxation data. *Journal of Magnetic Resonance (1969)* 95(2), pp. 221–234. ISSN: 0022-2364. DOI: 10.1016/0022-2364(91)90213-D (cit. on p. 22).
- Woessner, D. E. (1963). NMR spin-echo self-diffusion measurements on fluids undergoing restricted diffusion. *The Journal of Physical Chemistry* 67(6), pp. 1365–1367. DOI: 10.1021/j100800a509 (cit. on pp. 29, 65).
- Yaramanci, U., G. Lange, and M. Hertrich (2002). Aquifer characterisation using Surface NMR jointly with other geophysical techniques at the Nauen/Berlin test site. *Journal of Applied Geophysics* 50(1-2), pp. 47–65. ISSN: 0926-9851. DOI: 10.1016/S0926-9851(02)00129-5 (cit. on p. 55).

# A. Appendix

## A.1. KGM for planar and spherical pore geometries

The governing equations of KGM can be adapted to other basic pore geometries. This can be done using an explicit solution for  $T$  (Eq. 3.10) given by (Godefroy et al., 2001b) for basic pore geometries and adapting the fluid flow model (Eq. 3.1) to the new pore geometry which is usually done using an equivalent  $S/V$  of the pore. Following the derivation of KGM described in Chapter 3.4 this leads to

$$K = \frac{\rho g}{2\tau^2 \alpha^2 \eta} \phi \left( \frac{-D}{\rho} + \sqrt{\left(\frac{D}{\rho}\right)^2 + \frac{2\alpha D T_B T}{T_B - T}} \right)^2, \quad (\text{A.1})$$

where pore shape index  $\alpha = 1, 2, 3$  for planar, cylindrical, and spherical pores respectively. The impact on KGM is shown in Figure A.1 Changes in pore shape index ( $\alpha$ ) do not only lead to a small shift in the predicted  $K$ , which can be compensated to some degree by adapting tortuosity ( $\tau$ ), but predominantly affect the range of the slow-diffusion case, which increases with increasing  $\alpha$ .

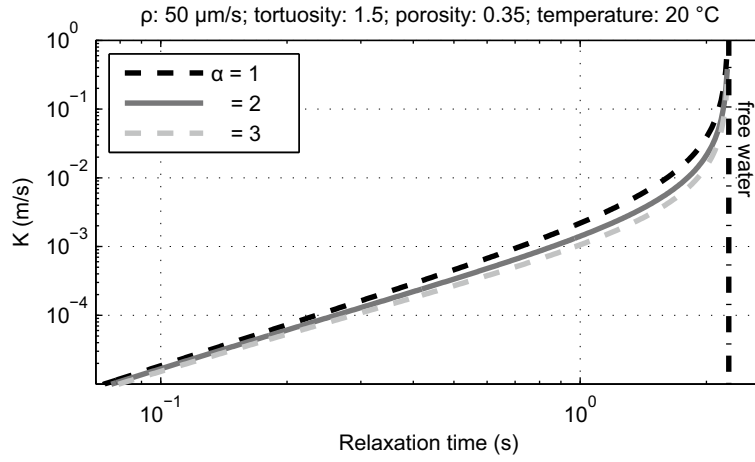


Figure A.1.: Comparison of the impact of different pore geometries on KGM, where  $\alpha = 1, 2, 3$  for planar, cylindrical and spherical pores respectively.

## A. Appendix

For the presented data sets of glass beads and quartz sand, tube-shaped pores ( $\alpha = 2$ ) are most suitable for finding a constant material specific  $\rho_a$  for all samples. For glass beads, a spherical pore geometry ( $\alpha = 3$ ) might also explain the measurements within the error level. But the ranges of  $\rho_a$  for the different grain sizes overlap to a lesser degree. Planar pore geometry fails to predict  $K$  estimated by flow measurements probably due to the reduced impact of the diffusion on planar pores. Further research might show if Equation A.1 can be successfully applied on samples with other pore geometries.

## A.2. Structure of the Jacobian matrix

The derivation of the Jacobian matrix ( $\mathbf{J}$ ) is described in the following for a discrete data space  $d_n$  and QTI using a model space consisting of cells ( $c$ ) with respective  $w_c$  and a monoexponential  $T_{2c}^*$ . Therefore, the partial derivative for every synthetic data point  $d_{ln}$  with respect to the intrinsic model parameters is given by:

$$\frac{\partial d_{ln}}{\partial w_c} = \mathbf{G}_{cl}^A e^{-t_n/T_c} \quad \text{and} \quad (\text{A.2})$$

$$\frac{\partial d_{ln}}{\partial T_c} = (t_n/T_c^2) \mathbf{G}_{cl}^A w_c e^{-t_n/T_c} . \quad (\text{A.3})$$

In case of using the real-valued amplitudes of  $\mathbf{d}$ ,  $\mathbf{G}_{cl}^A$  is the transformed kernel which yields  $|d_l| = \mathbf{G}_{cl}^A m_c$  according to Mueller-Petke and Yaramanci (2010). The matrices  $\mathbf{H}_n$  and  $\mathbf{I}_n$ , given for a fixed time gate  $n$  and referring to the derivatives of  $w$  and  $T_2^*$  respectively, can be written as:

$$\mathbf{H}_n = \begin{bmatrix} \frac{\partial d_{1n}}{\partial w_1} & \frac{\partial d_{1n}}{\partial w_2} & \dots & \frac{\partial d_{1n}}{\partial w_C} \\ \frac{\partial d_{2n}}{\partial w_1} & \ddots & & \vdots \\ \vdots & & \ddots & \vdots \\ \frac{\partial d_{Ln}}{\partial w_1} & \dots & \dots & \frac{\partial d_{Ln}}{\partial w_C} \end{bmatrix}; \quad \mathbf{I}_n = \begin{bmatrix} \frac{\partial d_{1n}}{\partial T_1} & \frac{\partial d_{1n}}{\partial T_2} & \dots & \frac{\partial d_{1n}}{\partial T_C} \\ \frac{\partial d_{2n}}{\partial T_1} & \ddots & & \vdots \\ \vdots & & \ddots & \vdots \\ \frac{\partial d_{Ln}}{\partial T_1} & \dots & \dots & \frac{\partial d_{Ln}}{\partial T_C} \end{bmatrix}. \quad (\text{A.4})$$

Combining  $\mathbf{H}_n$  and  $\mathbf{I}_n$  of all time gates and merging them leads to:

$$\mathbf{J} = \begin{bmatrix} \mathbf{H}_1 & \mathbf{I}_1 \\ \mathbf{H}_2 & \mathbf{I}_2 \\ \vdots & \vdots \\ \mathbf{H}_N & \mathbf{I}_N \end{bmatrix}. \quad (\text{A.5})$$

### A.3. Transformation of the model domain

In order to restrict  $w$  and  $T_2^*$ , both summarized in  $\mathbf{m}$ , within a lower bound  $\mathbf{m}_l$  and an upper bound  $\mathbf{m}_u$ , a cotangent transform is used similar to Mueller-Petke and Yaramanci (2010).

$$\mathbf{m}^{cot} = -\cot\left(\frac{\mathbf{m} - \mathbf{m}_l}{\mathbf{m}_u - \mathbf{m}_l}\pi\right). \quad (\text{A.6})$$

A separate value of  $\mathbf{m}_l$  and  $\mathbf{m}_u$  were chosen for  $w$  and  $T_2^*$ . Additionally to the benefit of restricting  $w$  and  $T_2^*$ , this has the advantage of combining two physical quantities into a unit-less measure. The transformed Jacobian  $\mathbf{J}^{cot}$  is then computed by means of total differentiation

$$\mathbf{J}^{cot} = \mathbf{J} / \frac{\partial \mathbf{m}^{cot}}{\partial \mathbf{m}} = \mathbf{J} \frac{\mathbf{m}_u - \mathbf{m}_l}{\pi} \sin^2\left(\frac{\mathbf{m} - \mathbf{m}_l}{\mathbf{m}_u - \mathbf{m}_l}\pi\right). \quad (\text{A.7})$$

## A.4. Coordinates of the field examples

Eddelstorf:

Point	Easting (m)	Northing (m)	Elevation (m)	Note
p1	3609551.9	5892638.2	66.9	
p2	3609579.2	5892667.1	66.8	
p3	3609606.5	5892696.1	66.7	
p4	3609634.1	5892725.2	66.4	
Drilling	3609545	5892386	72	2829HY0003

Nauen:

Point	Easting (m)	Northing (m)	Elevation (m)	Note
p1	3744517.2	5829681.1	-	formerly: P5
p2	3744535.1	5829697.1	-	formerly: P6
p3	3744570.8	5829729.2	-	formerly: P7
p4	3744588.7	5829745.2	-	formerly: P8
Drilling	3744354.1	5829535.9	-	drill location

Schillerslage:

Point	Easting (m)	Northing (m)	Elevation (m)	Note
p1	3565957.0	5818525.2	-	formerly: S7
p2	3565834.6	5818548.2	-	formerly: S6
p3	3565859.2	5818543.7	-	formerly: S5
p4	3565883.7	5818539.2	-	formerly: S4
p5	3565908.4	5818534.6	-	formerly: S3
p6	3565932.6	5818530.2	-	formerly: S2
p7	3565957.0	5818525.2	-	formerly: S1
Eng03	3565931.7	5818530.5	51.07	drill location
Eng08	3565892.4	5818536.0	51.29	drill location
Eng20	3565808	5818553	51.4	drill location
ERTstart	3565778.7	5818559.6	-	
ERTend	3565972.3	5818519.5	-	

Table A.1.: Coordinates of important locations for the presented field examples given in the Gauss-Krüger coordinate system using a Bessel ellipsoid (Potsdam Datum).